Developing Interaction Potentials From First Principles

Lindsay Foy

PhD
The University of Edinburgh
2008

The work in this thesis is entirely my own, except where I have *either* acknowledged help from a named person or given a reference to a published source or a thesis. Text taken from another source will be enclosed in quotation marks and a reference given.

Date **Signature**

Abstract

Interaction potentials for the double-perovskite cryolite, Na_3AlF_6, have been developed for use in classical Molecular Dynamics (MD) simulations using a method whereby ionic configurations are generated with empirical pair potentials, the multipoles and forces on the ions and the stress tensor of the cell are extracted from *ab initio* single-point DFT calculations, and then the multipoles, forces and stresses from the MD simulations are 'fit' to the *ab initio* quantities in a series of steps in which the potential parameters are optimized, for models of varying complexity. Previously, interaction potentials have been developed empirically by tuning the parameters to reproduce experimentally-derived properties such as structure factors and densities, and so the testing and development of the newer method is necessary in order to standardize a way of obtaining potentials from first principle considerations. A fitted potential was then used to characterize the ion dynamics in crystalline cryolite: a monoclinic to orthorhombic phase transition and the low-temperature-phase tilt-domain structure of the AlF_6^{3-}, the dominant structural features, are reproduced. The motional processes, which have been studied indirectly in NMR, conductivity and diffraction experiments, include oscillation of the AlF_6^{3-} and sodium ion diffusion - it has been suggested that these occur at a remarkably fast rate. The nature of the AlF_6^{3-} oscillatory motion is studied in more depth than accessible to experiment, and its connection with diffusion is investigated. Given the intrinsically defective nature of cryolite and the absence of diffusion in the initial simulations, defects are introduced to observe their effect on the dynamics: they are shown to be necessary for diffusion. This work has been written up in an article accepted for publication in the Journal of Physical Chemistry.

The *ab initio* potentials developed as above involve representing a system with formally charged monatomic ions. We extended the scope of the method significantly with technical developments to allow for the inclusion of molecular ions, such as the hydroxide ion, the sulphate ion or the uranyl ion, where the intraionic bonding has significant covalent character. The appropriate modifications of the MD code were made and a modified force-fitting procedure was developed. The new method was applied to $Mg(OH)_2$ which is an important mineral (brucite) and to the melts of uranyl chloride which are of interest in nuclear waste reprocessing. Although we found good potentials were harder to obtain for these compounds, we found this arose from their layered structure rather than the molecular nature of the ions, and that our method could achieve a level of success approaching that used in the cryolite work on further iterations of the fitting process.

Acknowledgements

Firstly I would like to thank my supervisor Professor Paul A. Madden for his guidance and help throughout my PhD. I would also like to thank the other members of the Madden group who have made the experience of research over the last few years more enjoyable: Michael Pounds, Robert Heaton, Stewart Reed and Dario Marrocchelli. Thanks are also due to Martin Plummer and Phil Hasnip for their work on the extensions to the CASTEP code which made this project possible.

Contents

List of Figures

List of Tables

Chapter 1

Introduction

The ability to accurately model materials by computer simulation is a great challenge in science, with several key points of motivation. To be able to observe the dynamic processes occurring at a microscopic level under a variety of conditions and link them to observable, macroscopic properties gives us a more complete understanding of how materials work. For example, in the area of ionic solids upon which our work is focused, there are many interesting structural and dynamic phenomena which occur such as ionic conduction, molecular-ion reorientation and transitions between different solid phases, a more complete picture of which can be derived by complimenting experimental studies with simulation. Many technologies utilise phenomena such as these, which underpin the material properties relied on, for example, in the processing of nuclear waste, solid oxide and hydrogen fuel cells and the electro-extraction of metals. Simulation allows us to study the behaviour of materials under a wide range of physical conditions, which are not always easily accessible, safe, or affordable experimentally - or indeed possible. Extreme temperatures and pressures such as those in the earth's mantle, and hazardous substances such as those in nuclear waste would be examples whereby study by simulation has a large advantage. Where simulation can be taken to the *predictive* level, it is a very powerful tool in such cases.

While *ab initio* simulation methods provide a more rigorous description of the interatomic interactions in a material, they are often not computationally tractable

for anyone trying to simulate the phenomena mentioned above which require large simulation cells and long simulation times. Therefore we use classical methods which are based upon Newton's laws and require some form of interaction potential. To model the behaviour of any material accurately using non-*ab initio* methods requires a good interaction potential. In the past these have been derived empirically by tuning the parameters in the potential to reproduce experimental properties such as density and vibrational frequencies. A recent development in this area in the condensed phase is to 'fit' potentials: to match quantities such as forces and multipoles predicted by a potential model to the same quantities from *ab initio* calculations, by adjusting the parameters in the model.

This thesis describes how we developed classical interaction potentials for cryolite using *ab initio* methods, and how we went on to use them to study the ionic motion in the solid phase by simulation. In previous work, ionic interaction potentials for AlF_3 [1] and its mixtures with NaF [2] have been proposed on the basis of empirical considerations. It has been shown how anion dipole polarization is the key physical ingredient in an ionic interaction model for stabilizing the tilting of the Al-centred octahedra in cryolite [2] and in pure AlF_3 [1], thereby giving a good account of the crystal structure and phase behaviour. These interaction potentials, which comprise formally charged Born-Mayer pair potentials supplemented by an account of anion polarization [3], were also used in the first phase of the present work [4]. Motivated by a general need to extend the modeling of fluoride materials onto a *predictive* level [5] and also by a desire to improve quantitative aspects of the cryolite dynamical behaviour obtained with the empirical potentials, revealed in the early stages of this work, we also derived a potential of the same type from purely *ab initio* considerations which was used for the simulations yielding the results described herein.

Several considerations motivate our interest in performing computer simulation studies of the ionic motion in solid cryolite. Understanding the physical properties of

compounds that exhibit the perovskite structure is important in geological science, where magnesium silicate ($MgSiO_3$) perovskite is the dominant material constituting the Earth's lower mantle [6]. Perovskites are also of technological interest: several electroceramics [7, 8] and high-temperature superconductors [9] adopt the perovskite structure. The resistivity of cryolite itself drops by over three orders of magnitude between 450° and 550°C [10]. The NMR studies carried out on cryolite indicate the existence of a considerable degree of ionic motion but, as yet, they have not been able to present a consistent picture of the ion dynamics. Owing to the range of ionic motion that exists in the solid phase (outlined in section 3.5), Na_3AlF_6 should be an ideal material for refining NMR techniques to examine the motion of quadrupolar nuclei [11]: however, a notable feature of the NMR results is that there are inconsistencies at a quantitative level between results obtained by different groups and even between the results obtained by the same group on different samples (for example, natural and synthetic cryolite [12]). Furthermore, there are qualitative inconsistencies between the NMR picture of the solid as one sustaining a high degree of ionic motion well below the phase transition, and that which emerges from the diffraction data, which indicates the contrary. Simulations should, in principle, give insight into the character of possible motions and may indicate the source of these inconsistencies.

Apart from the interest in studying the solid state, molten cryolite is the electrolyte in the production of aluminium from alumina, and thus of enormous importance in its own right [13], so the development of good, transferable models of the ionic interactions is a significant goal. We have developed empirically parameterized simulation models on several occasions [2, 1] and have shown how these potentials can reproduce the crystal structures although we have not successfully connected their dynamical properties to observation. In this work, we will use a potential derived from *ab initio* considerations, using techniques previously used to model oxides [14]. We begin with an account of the development of this potential and we will

contrast its predictions with those of the empirical potentials used in simulations of cryolite in the run-up to this work [4].

The AlF_6^{3-} units in cryolite are molecular in their behaviour, although the Al-F bonding is of an ionic nature. In other 'ionic' materials however, not all of the bonding falls into this regime: truly molecular ions such as the hydroxide, carbonate, and sulphate species are held together by covalent interactions. For these we need to reconsider our potential model, and hence make extensive changes to our potential fitting process, with the aim of developing interaction potentials for such compounds from *ab initio* considerations. As a further extension of our extended ionic model, we developed models for incorporating molecular ions into our atomic MD program - namely the hydroxide and uranyl ions. In both models we rigorously maintained our principle of describing the system at an *atomic* level: in one we described the intramolecular interactions using harmonic springs, in the other we applied bond length constraints which enforced the rigid retention of molecular geometry throughout a simulation. Modeling the molecular ions as rigid entities (though still on an atomic level) and focusing on the intermolecular interactions seemed to be a good foundation, where it is these interactions we are chiefly interested in as they govern the structure and dynamics at a microscopic level, which can in turn be associated with macroscopic phenomena of technological interest.

In terms of wider motivation, there is considerable interest in both uranyl and hydroxyl compounds. Layered double hydroxides in particular are important in mineralogy, forming many intercalation compounds [15]. A layered structure is typical of many hydroxyl compounds, including $Mg(OH)_2$, $Ca(OH)_2$ and $Al(OH)_3$, in which the metals are octahedrally coordinated and the octahedra share edges, in an approximate hexagonally close-packed system of oxygen atoms conforming to slight variants of the the CdI_2 structure. The hydrogen atoms are oriented into the the interstices in between the layers. These compounds are characterized by strong bonding between the atoms in the sheets and relatively weak forces between the

sheets, allowing a wide range of charged and neutral molecules/atoms to be accomodated [16, 17]. For example, it is possible for other metals to be intercalated to occupy these sites to form layered double hydroxides, or 'anionic clays'. Such materials are of use as catalysts and catalyst supports [18], in separation and membrane technology, in filtration and in the scavenging and controlled release of anions through their absorption and anion exchange properties [19]. They can also be used for storing reactants for use in fine chemical synthesis [20], for storing nutrients or pesticides for use in agriculture [21], and for containing the products of degradation reactions in the surrounding enviroment [22]. The uranyl anion is a crucial species in the extraction of uranium ore and the processing of nuclear fuel [23]. It is an extremely thermodynamically stable species and the U=O double bond undergoes few chemical reactions, for which reason it is particularly difficult to get into elemental form, but also makes uranyl compounds a safe way of transporting the element.

In summary, the work in this thesis is largely focused on the development of interaction potential fitting techniques from *ab initio* considerations, where we have chosen materials of scientific and technological interest to work with, which also advance our methods. In the case of cryolite, we go on to make an in-depth study of the ion dynamics to gain insight into the wide array of microscopic phenomena that are thought to occur.

Chapter 2

Computational Methods

2.1 Molecular Dynamics Simulation

In this work we optimise interaction potentials for use in classical Molecular Dynamics ('MD') simulations. This involves using MD simulation to perform the force and multipole calculations on ionic configurations for comparison with the *ab initio*-derived quantities. We go on to perform basic tests on the potentials, and for the case of cryolite we carried out an extensive study of the structure and dynamics in the solid phase by MD simulation. It is a useful tool in gaining a better picture of the properties and behaviour of a material at a microscopic level, where we can make direct observations without the uncertainty as to which microscopic phenomena may be the cause of a particular observable in an experimental study.

We choose from several possible ensembles in MD simulation, depending on which three of the thermodynamic variables N,V,T and P we wish to hold constant. In studies where we aim to replicate the behaviour of a 'real' system under experimental conditions we would keep the temperature constant by implementing a thermostatting procedure; for example, if the kinetic energies grow too high then the particle velocities are scaled down accordingly. The number of particles is also kept constant, via the periodic boundary conditions mentioned below. We would typically treat the remaining two variables V and P thus; by equilibrating a system at constant *pressure* until a steady structure (volume, cell dimensions) could be observed to be maintained, then studying the dynamics over longer simulations at

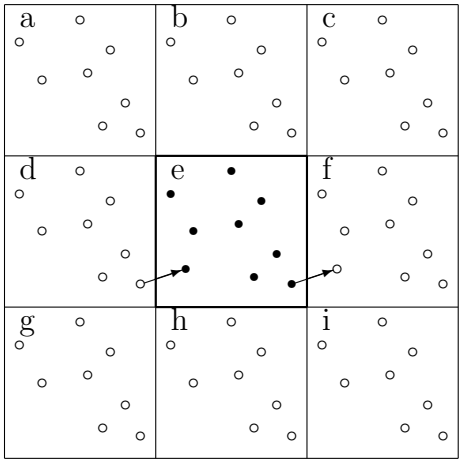

Figure 2.1: [24] The application of Periodic Boundary Conditions. When an ion leaves the simulation cell, for example the ion at the bottom right of cell *e* moving from cell *e* to the image cell *f*, it is replaced by the equivalent ion from the image cell, which for this ion is cell *d*, which moves in through the opposite face.

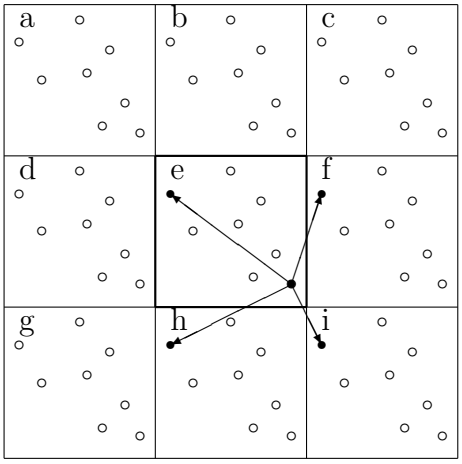

Figure 2.2: [24] The calculation of the identity of *Nearest Neighbours*. The ion at the bottom right of cell *e* is closer to the image of the ion at the top left of cell *e*, in cell *i*, than to the ion in cell *e* itself.

constant *volume*. Use of a barostat to keep the pressure constant is typically several times more computationally expensive; use of constant volume simulations, where appropriate, maximizes the length of time that can be devoted to studying processes such as diffusion and molecular reorientation which occur relatively slowly on the MD timescale of 10^{-10}-10^{-9}s.

To conserve the composition of our simulation cell, which typically consists of a several hundred to one thousand ions, we apply *periodic boundary conditions* whereby the cell is replicated throughout space infinitely in all directions: as a particle leaves through one face, it re-enters through the opposite face (Figure 2.1). The crystal cell axes always coincide with the axes of the periodically repeating cell. This setup prevents surface effects influencing the behaviour of the system, and allows bulk properties to be studied. The long range Coulombic interactions between ions are calculated using an Ewald summation [24], which finds the forces due to pairs of ions within one cell in 'real space', then finds the forces due to ions in successive shells of surrounding cells in 'reciprocal space' up to a point where

the converging values can be predicted accurately, relying on the infinite periodicity of the system. Short range interactions need only be calculated for pairs of ions i and j within a radius of up to half of one cell length; here the *minimum image convention* [25] is invoked, where the forces found on i are those due to the nearest of all periodic images of every j, as shown in Figure 2.2.

2.2 The Interaction Model

2.2.1 The Baseline Model

In order to simulate a given material, we need a description of the interactions between all the species in the system, which at our level equates to all *atoms*, though approximations can be made to treat groups of atoms - molecules or parts of molecules - as single entities. This set of interactions comes in the form of an energy potential V, from which we can obtain the forces on the atoms:

$$\mathbf{F}(\mathbf{r}) = -\frac{d\mathbf{V}(\mathbf{r})}{dr} \tag{2.1}$$

and from the forces we can use Newton's laws of motion to calculate the positions, velocities, accelerations... of the atoms from step to step, which in our methodology is carried out using the Velocity Verlet algorithm [24].

Our baseline interaction potential, the Rigid Ion Model ('RIM'), consists of a pair potential of Born-Mayer form [26]. This pair potential is written:

$$V(r_{ij}) = \frac{Q_i Q_j}{r_{ij}} + B^{ij} e^{-\alpha^{ij} r_{ij}} - f_{ij}^6(r_{ij}) \frac{C_{ij}^6}{r_{ij}^6} - f_{ij}^8(r_{ij}) \frac{C_{ij}^8}{r_{ij}^8}. \tag{2.2}$$

The first term in Equation 2.2 describes the Coulombic (charge-charge) interactions between the atomic ions, where Q represents the ionic charges on the atoms. The second is a Fumi-Tosi short-range-repulsion term [27, 28] which accounts for the overlap of electron density under the Pauli Exclusion Principle. The third and fourth terms are attractive and represent the dispersion interaction between atoms, where $C_{ij}^{(6)}$ and $C_{ij}^{(8)}$ are the dispersion coefficients. $f_{ij}^{(n)}$ are dispersion damping

functions which are present to prevent the terms tending to infinity as $r \to 0$, and are given by the Tang-Toennies formula [29]:

$$f_{ij}^{(n)}(r_{ij}) = 1 - e^{-(b_{ij}^n r_{ij})} \sum_{k=0}^{n} \frac{(b_{ij}^n r_{ij})^k}{k!}. \tag{2.3}$$

The parameters open to negotiation in this model we consider to be the short-range B and α, which approximately signify the relative atomic radii and steepness of the repulsive potential wall, respectively. The values for these have, in the past, been reached by attempting to match properties such as the density and vibrational frequencies to those reported from experiment. The more recently developed method is described in the next section, whereby we 'fit' information predicted by the potential model to the same information calculated from *ab initio* considerations, by varying these parameters, stepwise, until we find the best match. The dispersion coefficients C^n and parameters f^n may also be derived this way, or fine-tuned post-fitting.

2.2.2 The Polarizable Ion Model

For the majority of systems the inclusion of polarization in the model significantly increases the accuracy of the simulations, and this model has been described previously [3]. Exceptions include the crystalline alkali halides in which the ions occupy highly symmetric sites. However even compounds considered to be well within the limit where we would describe the bonding to be 'ionic' appear to require something more than a rigid-sphere model with uniform spherical charge distribution. This is not surprising considering the thermally distorted and distorting environments of the crystallographic sites, where polarization will be induced to some extent, and even a change of size or shape deformation.

In the Polarizable Ion Model ('PIM'), we assign a dipole-polarizability α to the relevant species: if an ion of polarisability α is placed in an electric field $\boldsymbol{\varepsilon}$, the dipole moment induced on the ion is given by:

$$\boldsymbol{\mu} = \alpha \boldsymbol{\varepsilon}. \tag{2.4}$$

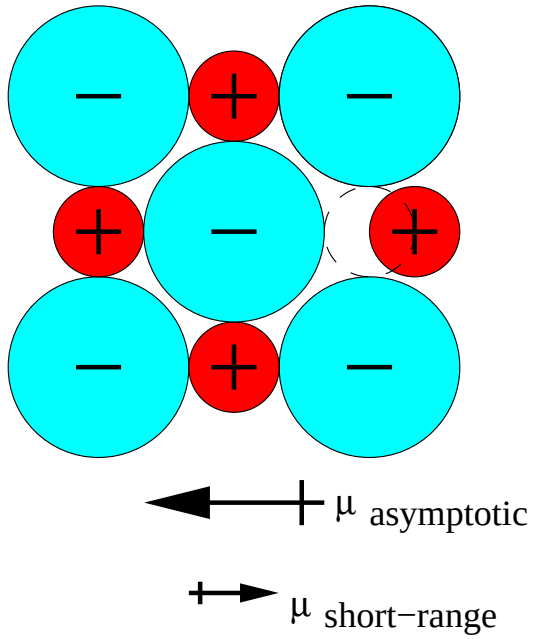

Figure 2.3: Origin of the 'asymptotic' and 'short-range' contributions to the dipole induced by cation motion in a condensed phase.

The field will have a Coulombic contribution and a short-range contribution in opposition created by electron cloud overlap. This is illustrated in Figure 2.3: if one cation begins to move away, then a dipole is created on the anion with the negative end pointing in the opposite direction. This effect is modified however by the movement of the anion's electrons into the vacancy left by the displaced cation.

The induced multipoles interact both with each other and the ionic charges. Given that the distance R_{ij} separating ions i and j is much greater than the length characterising the charge separation in dipole μ^i, the Coulombic part is given by (minus) the first derivative of the potential at i as defined by the multipole expansion up to dipole level:

$$\varepsilon^i_\alpha = - \bigtriangledown_\alpha \left(TQ_j - T_\beta \mu^j_\beta + \ldots\right) = -T_\alpha Q_j + T_{\alpha\beta}\mu^j_\beta - \ldots, \tag{2.5}$$

$$\mu^i_{\alpha,Coulombic} = \alpha_i \left(\sum_{j\neq i} \frac{Q_j R_{\alpha,ij}}{R^3_{ij}} - \sum_{j\neq i} \mu^j_\beta \frac{R^2_{ij}\delta_{\alpha\beta} - 3R_{\alpha,ij}R_{\beta,ij}}{R^5_{ij}} + \ldots\right). \tag{2.6}$$

Here ε^i_α and μ^i_α are the α^{th} Cartesian components (x, y, z) of the electric field at ion i and electric dipole of i. $\mathbf{T}$ are tensors representing the separation between atoms,

and can be generalized as:

$$\mathbf{T}_{\alpha\beta\ldots\nu} = \frac{1}{4\pi\epsilon_0} \bigtriangledown_\alpha \bigtriangledown_\beta \ldots \bigtriangledown_\nu \frac{1}{\mathbf{R}}. \tag{2.7}$$

Also:

$$\delta = 1 \;\; where \;\; \alpha = \beta \quad ; \quad \delta = 0 \;\; where \;\; \alpha \neq \beta. \tag{2.8}$$

The short range contributions are given by:

$$\varepsilon^i_\alpha = -T_\alpha Q_j \tag{2.9}$$

$$\mu^i_{\alpha,short-range} = \alpha_i \sum_{j \neq i} g(R_{ij}) \frac{Q_j R_{\alpha,ij}}{R^3_{ij}}. \tag{2.10}$$

where g_{ij} is a short range damping function which is applied to the interaction between the anion dipoles and the cation charges, and takes the form:

$$g_{ij}(r_{ij}) = 1 - c_{ij} e^{-(b_{ij} r_{ij})} \sum_{k=0}^{4} \frac{(b_{ij} r_{ij})^k}{k!} \tag{2.11}$$

where b_{ij} and c_{ij} indicate the range and the strength of the damping respectively. The dipole (and quadrupole) interactions are not simply pairwise additive like the short-range terms. The dipole on an ion interacts with the dipoles on the surrounding ions, which in turn are effected by that dipole: these dipole induced dipole interactions are determined by a conjugate gradient algorithm.

We can increase the level of the potential by increasing the order of the multipoles to quadrupole level, in which we similarly assign a quadrupole-polarizability c_{pol} to the atoms. For reasons of cost, and because it is usually unnecessary to allow multipoles to form on the less diffuse and less polarizable cations, we would tend only to apply the PIM to the anions [3, 30]. In the cryolite work, the potential includes fluoride ion polarization only.

2.2.3 Compressible and Aspherical Ion Models

A further extension of the ionic model can be helpful for materials where the crystallographic sites have very asymmetrical environments, inducing a significant change in the shape of the charge cloud. A discussion of which level of potential is suitable

to use for a particular system is given in the following section. Polarization accounts for a part of this, but there will also be a change in the overlap and hence short-range repulsion with neighbouring atoms. In such cases we can extend the short-range part of the potential model for the same species we would model as being polarizable, by allowing the ions to change size (or 'breathe'), and to form distortions of dipolar and quadrupolar symmetry [3]. This is done by adding an extra term for each effect to the sum of Born-Mayer type exponentials. For a binary system '+/-' where the anion is deformable, this can be written:

$$\begin{aligned} V(r^{ij})^{SR} &= \sum_{i=-,j=+} B^{+-}e^{-\alpha^{+-}\rho^{ij}} + \sum_{i,j=-} B^{--}e^{-\alpha^{--}r^{ij}} + \sum_{i,j=+} B^{++\alpha^{++}r^{ij}} \\ &+ \sum_{i=-}\Big[D^i(e^{\beta^-\delta^i} + e^{-\beta^-\delta^i}) + (e^{(\eta^-)^2|\epsilon^i|^2} - 1) + (e^{(\zeta^-)^2|\kappa^i|^2} - 1)\Big] \end{aligned} \tag{2.12}$$

where the first three terms, in order, represent cation-anion, anion-anion, cation-cation interactions. The last three represent the self-energy of changing shape, and forming dipolar and quadrupolar distortions respectively: the parameters β, η and ζ are the spring constants associated with the ease of forming these distortions, and D^i is a coefficient reflecting the self-energy of shape-change. The parameter ρ^{ij} is given by

$$\rho^{ij} = r^{ij} - \delta^i - S^{ij}_{\alpha}\epsilon^i_{\alpha} - S^{ij}_{\alpha\beta}\kappa^i_{\alpha\beta}. \tag{2.13}$$

Only the cation-anion term has been given many-body character , where the variable ρ^{ij} contains three parameters to be optimized, one for each deformation effect. δ^i represents the breathing parameter of anion species i, and for a simple compressible ion model ('CIM'), ρ^{ij} is given by $\rho^{ij} = r^{ij} - \delta^i$, and we use only the first self-energy term. For dipolar and quadrupolar distortions we add in terms 2 & 5, and 3 & 6 respectively from Equation 2.12. $\boldsymbol{\epsilon}^i$ and $\boldsymbol{\kappa}^i$ are the *vector* and *tensor* which describe the magnitude and orientation of the *dipolar* and *quadrupolar* distortions respectively in what will here-on be referred to as the 'DAIM' and 'QUAIM' models.

S_α^{ij} and $S_{\alpha\beta}^{ij}$ are the interaction tensors, given by

$$S_\alpha^{ij} = \frac{r_\alpha^{ij}}{r^{ij}} \quad ; \quad S_{\alpha\beta}^{ij} = \frac{3r_\alpha^{ij}r_\beta^{ij}}{(r^{ij})^2} - \delta_{\alpha\beta}. \tag{2.14}$$

Like the polarization, this aspherical short-range extension is a many-body effect and we use conjugate gradients to solve for the extent of the deformation on each individual ion (δ^i, $\boldsymbol{\epsilon}^{\mathbf{i}}$ and $\boldsymbol{\kappa}^{\mathbf{i}}$): an ion's deformation is dependent upon the positions of the surrounding ions, causing it to change the distribution of its charge density, which in turn will change the charge distribution of the surrounding ions.

2.3 Potential Fitting

Detailed descriptions of the generalized *ab initio* "force-fitting" procedure, used to obtain the parameters in a potential of a chosen form from condensed phase, planewave Density Functional, electronic structure calculations have been give recently, along with descriptions of how it has been applied to other ionic compounds [14, 31, 5]. It involves varying the parameters in the potential to minimize the difference between the *ab initio* forces, dipoles, and quadrupoles on each ion and those obtained from the potential for a set of condensed phase configurations. Here, our potential fitting method is outlined.

It is a big challenge for simulation to accurately model the behaviour of real materials. Ideally we would use *ab initio* simulations, as the most rigorous description of inter-atomic interactions available. However, these are too computationally intensive to investigate phenomena on the scale of diffusion, molecular reorientation and phase transitions, and we must use the classical simulation methods described in the previous section, which are driven by Newton's laws, are much cheaper, and allow us to study larger systems and for longer periods of time. Yet, we require accurate potentials to describe the interactions. Previously these have been put together empirically by fine-tuning the parameters to recreate properties like densities and vibrational frequencies. While there has been potential fitting work carried out in the past on gas phase atoms, ions and molecules from an *ab initio* standpoint,

the condensed phase is a little-explored area. This is largely due to the difficulty in extracting single-particle information from the available *ab initio* data, where it is in the nature of condensed-phase materials that many-body interactions such as polarization have a far greater weight in the total interaction. Most of the readily obtained information is a property of the whole system (energy, polarization etc. . .) rather than individual particles, and the properties of ions and molecules change significantly from when they are isolated to when they are placed in a crystalline environment. So it is much more difficult to fit potentials for condensed-phase systems which describe the interactions between individual atoms.

2.3.1 The Fitting Method

The fitting method is outlined in Figure 2.4. We start by generating configurations of an appropriate size using an empirical potential. These configurations tend to be of thermally distorted crystalline structures, so as to sample a wide range of environments which will hopefully be representative of those in the real system. This will result in a wide range of forces and multipoles, giving our fitting program statistically good data to work with. The configurations need not be restricted to one phase/structure: indeed there is an advantage to using configurations in many crystal structures (provided they are thermodynamically plausible) and even liquid configurations as this should increase the transferability of any pair potentials generated from the fits. It is our aim to produce pair potentials (Na-Na, F-Al etc. . .) that are transferable between different compounds. Here we are working on the basis that this has been successful for empirically generated potentials, and also from the consideration that there is negligible difference in the nature of a certain species of ion between sets of similar compounds, where experimental studies have estimated 'ionic radii' and ionic polarizabilities.

Next we perform *ab initio* electronic structure calculations using the DFT-based CASTEP program [32], from which we extract the forces on the ions. Further to this we perform Wannier localizations [33, 34, 35] on the electron density from

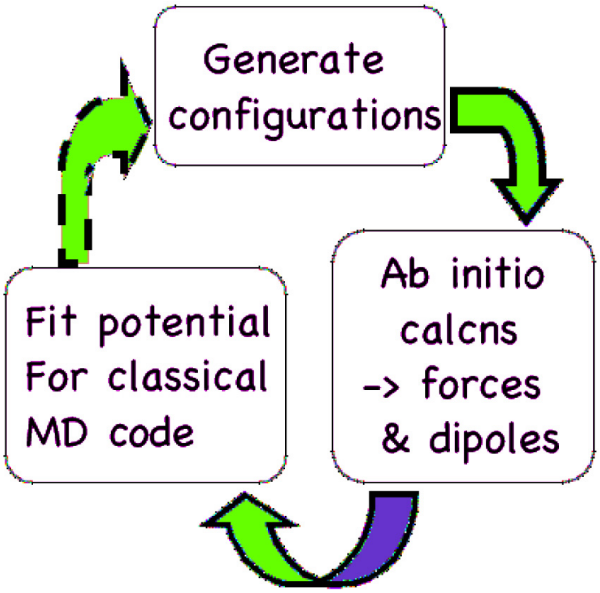

Figure 2.4: Illustrating the chain of events in the standard potential fitting process.

the first calculations, where the resulting Wannier functions represent the Kohn-Sham orbitals in the system. Once singly-assigned to the atoms, the distribution of their centres around each atom can be used to calculate the atomic dipoles and quadrupoles for use in the fitting. To calculate the dipole, we use:

$$\boldsymbol{\mu}^j = \sum_i Q^i \mathbf{R}^{ij} = -2 \sum_i \mathbf{R}^{ij} \tag{2.15}$$

where Q_i is the charge of Wannier function i (-2 a.u. for a filled orbital), $\mathbf{R}_i$ is the displacement between ion j and Wannier function i, and the sum is over all Wannier functions associated with the ion. To calculate the quadrupole we use:

$$\theta^j_{\alpha\beta} = -2 \sum_i \int d\mathbf{R} \; |\psi^i(\mathbf{R})|^2 \left(\frac{3R^{ij}_\alpha R^{ij}_\beta - R^{ij}\delta_{\alpha\beta}}{2} \right) \tag{2.16}$$

where we integrate over all space within a sphere of radius r_{cut}, and ψ_i are the wavefunctions of the orbitals associated with atom j, within this r_{cut}. Here, $\delta_{\alpha\beta}$ is defined as described in Equation 2.8, and R^{ij}_α and R^{ij}_β are the α^{th} and β^{th} Cartesian components (x, y, z) of the aforementioned displacement.

The size of the configurations we use is mainly restricted by the number of electrons required to be explicitly modeled in the CASTEP calculations, but as a rough

guide, up to 100 atoms is what we can usually expect to succeed with: to improve the statistics for the fitting process we run calculations on several configurations. The settings used in the CASTEP calculations are based upon those we have found to be successful in the past [36], for example we use a high plane wave energy cut-off of 1000eV, and perform tests at values around this region for any new system to ensure the total energy and more importantly the forces have converged by this point. All the work described here was carried out using a PBE-type exchange correlation functional[37]. A suitable distance cut-off by which we assign Wannier functions to individual atoms for multipole calculation is easily guessed at, taking into consideration the inter-atomic separations, and in ionic systems they can be assigned without deliberation as they lie very close to the nuclei. We can perform tests with more than one pseudopotential to ensure the consistency of the *ab initio*-derived forces with respect to the potential used.

Having obtained the forces and multipoles from *ab initio* calculations, we then go on to 'fit' the forces and dipoles predicted by the classical MD program to the *ab initio* values by varying the parameters in the potential model. It can be necessary to experiment with the step-values and ranges within which the parameters are permitted to vary in order to ensure the global minimum has been reached, though we find this is fairly insensitive to the starting values of the parameters. Using the newly-fit potential, it is then possible to generate more configurations which will hopefully be more representative of those in the real material than the configurations generated with an empirical potential. With these we can iterate the fitting process with the aim to improve the fit quality, further refining the potential.

In the fitting process, the best practice as developed to this point is to determine the polarization parameters alone first by fitting the dipoles and quadrupoles predicted by the potential model to the *ab initio* values. We then go on to optimize the short-range parameters by fitting the forces, while holding the polarization parameters fixed at the previously determined values. Here we are taking advantage of the

physical independence of the polarization and short range effects, which allows us to reduce the number of parameters the fitting procedure [38] is required to optimize at once. The fitting itself uses the MINUIT package [39] to minimize the function 'χ^2':

$$\chi^2 = \frac{1}{2}\sum_{i,C}\frac{\sum_\alpha |F^m_{i,\alpha,C} - F^{ai}_{i,\alpha,C}|^2}{|F^{ai}_{i,\alpha,C}|^2} \tag{2.17}$$

where here the example given is for the forces, but applies equally to multipoles. The sum is over all ions i in all configurations C, over all Cartesian components α of the force/multipole vector. The indices 'm' and 'ai' refer to the potential model and the *ab initio* methods.

The level of potential model required to achieve a 'good' fit varies from system to system, depending on the electronic structure, where we judge this to be a fit with a value of $\chi^2 < 0.1$. Ideally we would like to capture all of the physical effects such as ion polarization and ion deformation which can effect the crystal structure and dynamics to varying extents. At the same time we want to reduce the computational cost by not using an unnecessarily complex potential. As a baseline we use Coulomb charge-charge interactions as well as short range repulsion and dispersion interactions, the terms for which are given in Equation 2.2. This can be satisfactory for materials with simple regular structures and less polarizable ions such as Na and F in sodium fluoride. However it is not an adequate model for many compounds, including cryolite where the coordination polyhedra have complex tilt-patterns which we believe to be owing to polarization effects. Here we can allow the more polarizable ions to form dipoles and quadrupoles, and for very anisotropic systems let the ions change shape according to their environment (section 2.1).

As DFT calculations do not well-reproduce the effects of dispersion, we would tend to omit the corresponding parameters (C_n, f_n) from the initial force-fits, simply varying the short-range parameters. It is then possible to add dispersion into the potential after the fitting, by including the relevant terms in the interaction potential with 'best guess' starting values for each of the parameters. We would

then optimize these parameters by trial and error in the process of fine-tuning the structural dimensions predicted by the fitted potential. In the absence of dispersion effects in the *ab initio* simulation it is not unusual or surprising that the precise cell dimensions under the resulting potential to initially be at variance with those reported from experiment.

For each system studied, we attempt to fit potentials in steps of complexity to determine the best choice of potential to use for simulation studies, and by the way the fit-quality improves we can also gain insight into the relative weights each of these bonding effects have in the accurate reproduction of the real material.

2.4 Analytical Techniques

In the analysis of the structure and dynamics in our simulations, we use several functions, which are described in this section. The functions used to probe the structure and motion are all ensemble-averaged quantities. Where the functions are described by a Cartesian coordinate system, this will always be in the cell-frame: where the cell is orthorhombic the x axis coincides with the a, the y with the b and the z with the c.

2.4.1 Radial distribution functions

These are calculated from sets of ion positions generated during a simulation using the equation:

$$g_{ij}(r) = \frac{n_{ij}(r)}{4\pi r^2 (n_i n_j)^{\frac{1}{2}}} \tag{2.18}$$

where $n_{ij}(r)$ is the ensemble average of the number of species j in a radial shell at distance r, thickness dr, with species i at the centre, and n_x is the bulk density of species x. $n_{ij}(r)$ is given by:

$$n_{ij}(r) = \frac{1}{N_i}\frac{1}{N_t}\sum_{timestep=1}^{N_t}\sum_{i=1}^{N_i}\sum_{j=1}^{N_j}\delta(\mathbf{r} - (\mathbf{r_i}(t) - \mathbf{r_j}(t))) \tag{2.19}$$

where N_i and N_j are the total numbers of ions i and j, and N_t is the total number of time-frames of data that has been used in the calculation. The sharpness of the peaks

and relative heights of the maxima and minima indicate how rigid the structure is with respect to i and j: as one or both of the pair become more mobile the peaks broaden and begin to merge, though typically the first peak remains distinct for ions of opposite charge due to the high degree of ionic association between neighbours.

2.4.2 Mean squared displacements

The behaviour of the mean squared displacement functions can help reveal the nature of an ion's motion over a range of timescales. For species i they are calculated from the equation:

$$< \delta r_i^2(\Delta t) >= \frac{1}{N_i} \sum_{i=1}^{N_i} \sum_{t_0=1}^{N_t(\Delta t)} \frac{1}{N_t(\Delta t)} (\mathbf{r}_i(t_0 + \Delta t) - \mathbf{r}_i(t_0))^2, \tag{2.20}$$

where $N_t(\Delta t)$ is the number of time origins available for the time interval Δt. A function that plateaus shows that the species' motion is restricted, with an amplitude of $\sqrt{< \delta r_i^2(\Delta t_{plateau}) >}$ - this is the case for solids, and can include vibration and rotation. For liquids, or a sublattice of freely diffusing ions, the function increases approximately linearly as Δt increases and a diffusion coefficient can be calculated:

$$D_i = \lim_{\Delta t \to \infty} \frac{< \delta r_i^2(\Delta t) >}{6 \Delta t}. \tag{2.21}$$

2.4.3 Cage Correlation Functions

These describe the rate of exchange of ions in the first coordination sphere of a particular species, with ions in the rest of the cell. An r_{cutoff} for species i is located from the first minimum in the pair distribution function $g_{ij}(r)$, then a *neighbour list* $\vec{\ell_i}$ is created for each i by identifying which of the other N ions in the cell are within the distance r_{cutoff}. These will be a set of N_i vectors, of length N:

$$\vec{\ell_i} = \begin{pmatrix} f(r_{i1}) \\ \vdots \\ f(r_{iN}) \end{pmatrix} \tag{2.22}$$

where $f(r_{ij})$ is the Heaviside function,

$$f(r_{ij}) = \Theta(r_{\text{cutoff}} - r_{ij}) = \begin{cases} 1 & \text{if } |r_{ij}| \leq r_{\text{cutoff}} \\ 0 & \text{otherwise} \end{cases} . \tag{2.23}$$

To find out whether an exchange has occured between cage and bulk in the time interval Δt, the number of ions that have left i's neighbour list during that period is calculated:

$$n_i^{\text{out}}(\Delta t) = |\vec{\ell}_i(t_0)|^2 - \vec{\ell}_i(t_0) \cdot \vec{\ell}_i(t_0 + \delta t). \tag{2.24}$$

The cage correlation function is then given by:

$$C_i^{\text{cage}}(\Delta t) =< \Theta(c - n_i^{\text{out}}(\Delta t)) >, \tag{2.25}$$

where c is the number of atoms that must leave an atom's neighbour list before the coordination cage is considered to have decayed. In the program written for this work $c = 1$, and $\Theta = 1$ if $(c - n_i^{out}) > 0$, else $\Theta = 0$.

Cage lifetimes (τ_i^{cage}) can be extracted from the CF to give a measure of the stability of the different ionic complexes in the simulation. For example, an exponentially decaying function can be written:

$$C_i^{\text{cage}}(t) = C_i(0) e^{-\frac{t}{\tau_i^{\text{cage}}}}, \tag{2.26}$$

and the lifetime is found by integrating the function from $0 \rightarrow \infty$:

$$\tau_i^{\text{cage}} = \frac{1}{C(0)} \int_0^\infty C_i^{\text{cage}}(t) \mathrm{d}t, \tag{2.27}$$

or by finding the value of t at the point where $C_i^{\text{cage}}(t) = \frac{1}{e} C_i^{\text{cage}}(0)$, assuming exponential decay.

2.4.4 Orientational Correlation Functions

The functions in this work are expressed in terms of the angle θ swept about by the bonds (i) in the octahedral AlF_6^{3-} complex ions, during the time interval Δt:

$$C_{\theta 1}(\Delta t) =< \cos[\theta_i(\Delta t)] >=< \mathrm{P}_1[\cos(\theta_i(\Delta t))] >, \tag{2.28}$$

$$C_{\theta 2}(\Delta t) =< \frac{1}{2}(3\cos^2[\theta_i(\Delta t)] - 1) >=< \mathrm{P}_2[\cos(\theta_i(\Delta t))] >, \tag{2.29}$$

where the P_n are the Legendre polynomials. The values of $\cos\theta_i(\Delta t)$ are calculated for all Al-F bonds in the cell using the equation:

$$\cos\theta_i(\Delta t) = (dx_i(t_0)dx_i(t_0{+}\Delta t)){+}(dy_i(t_0)dy_i(t_0{+}\Delta t)){+}(dz_i(t_0)dz_i(t_0{+}\Delta t)) \tag{2.30}$$

where dx, dy and dz are the Cartesian components of the normalised Al-F bond vectors.

For an ensemble of non-interacting molecules rotating with the same angular frequency, the functions would oscillate indefinitely, the $C_{\theta 2}$ at twice the rate of the $C_{\theta 1}$. In condensed matter though, the mean time between collisions is very short compared to the reciprocal of the rotational frequency, so any bulk correlation is lost due to rapid modulation of angular velocities. As a result, the oscillations are completely damped and not observable, the functions going $\rightarrow 0$ as $t \rightarrow \infty$. It is possible to extract a mean *angle of libration* $\Theta^{\mathrm{lib}}(\Delta t)$ as a function of Δt:

$$\Theta^{\mathrm{lib}}(\Delta t) = \arccos(C_{\theta 1}(\Delta t)), \tag{2.31}$$

which can be compared to values derived from NMR linewidth studies.

2.4.5 Site exchange correlation functions

The program used to calculate these functions was written specifically for use in this work on the cryolite structure, in order to determine the rate of Na^+ exchange between the 6- and 12- coordinate sites. The type of site each Na^+ occupies is determined at every timestep by considering the RDFs $g_{Na,X}(r)$. An 'r_{cut}' value is determined corresponding to the position of the first minimum in the $g_{Na,Al}(r)$ function, and the number of Al^{3+} ions within this distance from each Na^+ is found in order to assign the site-type. Each Na^+ is then assigned a value of 'a' for every timestep, where:

$$a_i(t) = \begin{cases} +1 & \text{for the 6-crd. site} \\ -1 & \text{for the 12-crd. site} \end{cases} . \tag{2.32}$$

The value of $a_i(t)$ for each Na^+ (i) is correlated with the value after a time interval Δt, and the ensemble average is calculated:

$$C^{site}(\Delta t) = < a(t_0)a(t_0 + \Delta t) > . \tag{2.33}$$

In the limit of rapid exchange, the originally 6-crd. ions have a 1 in 3 chance of occupying a 6-crd. site and the originally 12-crd. ions (of which there are twice as

many) have a 2 in 3 chance of occupying a 12-crd. site, and the function is modified to go to zero as $t \rightarrow \infty$ by taking this into consideration. The site-occupancy lifetimes can then be obtained by the same method of integration as the cage- and rotation- lifetimes.

Chapter 3

Potential Fitting for Cryolite: Results

3.1 The Scheme for Cryolite

In order to fit a potential for cryolite we decided to use configurations of pure AlF_3 and NaF. We carried out some initial tests on cryolite itself, using configurations generated by the empirical potential given in Tables 3.1 and 3.2, which showed that fitting all of the short-range Fumi Tosi parameters for this compound comprised of three species was pushing the ability of the fitting program to find the global minimum owing to the number of parameters involved: twelve for a three-species systems versus six for a two-species system. By using NaF and AlF_3 we would be fitting the respective pair-potentials separately, reducing the number of parameters the fitting program was required to deal with at once. We generated configurations of AlF_3 in its 'ReO_3' structure [15, 40] by running short MD simulations using the empirical potential parameters. In this structure, the Al^{3+} ions are coordinated by six F^- ions, as they are in cryolite, and the F^- coordination number is two. For NaF the configurations were derived from MD simulations of the rocksalt, zinc-blende and CsCl structures, in which the F^- ions have coordination numbers of 6, 4 and 8, respectively, and liquid configurations were also generated. The configurations therefore sample as wide a range of thermally distorted coordination environments for the F^- ions as are likely to be found in cryolite.

The values for the parameters in the empirical potential [2, 1] used to generate

the configurations for electronic structure calculations are given in Table 3.1. (The significance of each parameter is shown in Equation 2.2. The short-range repulsion parameters B^{ij} and α^{ij} are linked to the pair cross-sectional radius and the steepness of the potential wall respectively, though the link is not independent as changing the value of α^{ij} also changes the effective radius, owing to the functional form of the potential.)

Pair	B^{ij}	α^{ij}	C^6	f^6	C^8	f^8
F^--F^-	120.93	2.79	44.37	1.9	538.8	1.9
Al^{3+}-F^-	80.00	1.80	1.05	1.9	2.04	1.9
Na^+-F^-	11.76	1.60	6.8	1.9	54.0	1.9
Al^{3+}-Al^{3+}	0.00	1.00	1.86	2.1	1.75	2.1
Na^+-Na^+	11.57	1.60	1.6	2.1	1.8	2.1
Al^{3+}-Na^+	2412.2	2.14	96.2	2.1	848.4	2.1

Table 3.1: Short-range parameters in the cryolite dipolar empirical pair potential used to generate NaF and AlF_3 configurations for electronic structure calculations. All values are given in atomic units.

α_F	$b_{F,Al}$	$c_{F,Al}$	$b_{F,Na}$	$c_{F,Na}$
6.78	1.89	1.00	1.86	1.00

Table 3.2: Polarization parameters in the dipolar empirical pair potential used to generate configurations for electronic structure calculations. All values are given in atomic units.

3.2 NaF

3.2.1 Step one: Generating Configurations of NaF

The crystal structure of sodium fluoride under atmospheric pressure is the rock-salt structure shown in Figure 3.1, in which all the sites have octahedral symmetry. Being a typical highly ionic structure, and containing ions at the least covalent ends of the spectrum in terms of electronegativity, we would anticipate no major issues in achieving good fitting results under our ionic interaction model, even at the more basic levels of potential. With the wish to produce *transferable* pair-potentials in mind, we did not restrict our fits for this compound to using configurations from

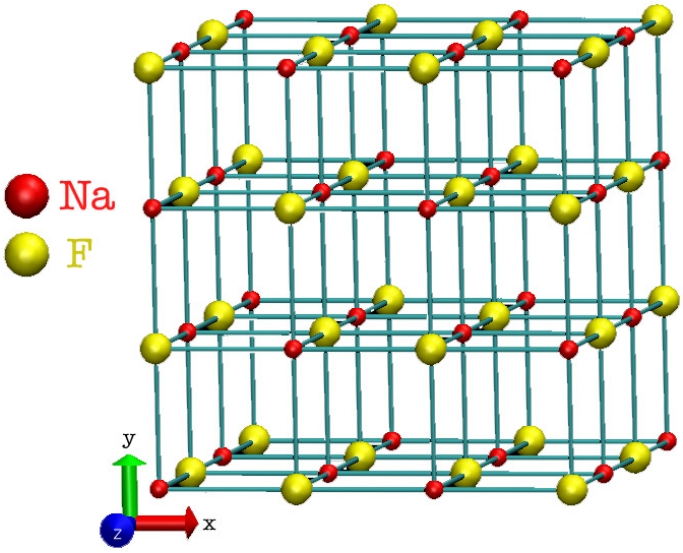

Figure 3.1: The rock-salt structure of NaF.

the thermally distorted rock salt structure, but in addition chose to generate Zinc Blende, CsCl and liquid configurations. Each of these consisted of a cubic simulations cell, the details of which are given in Table 3.3-3.4. With no information about the optimum cell dimensions for the additional structures, we made estimates of 'starting values' using anion-cation bond lengths in rock-salt, taking into consideration that the bond lengths will increase slightly with coordination number. We then equilibrated the systems at constant pressure (using NPT simulations) under the potential derived from Tables 3.1-3.2, ensuring the desired crystal structure was retained in each by comparison of the structure factors of the initial and equilibrated systems. We chose lower temperatures at which to run the CsCl and Blende simulations, which was necessary to retain the structures: at higher temperatures the systems had sufficient energy to undergo the phase transition back to the thermodynamic ground state, the rock-salt structure.

3.2.2 Step two: Forces and Multipoles from *ab initio* Calculations

Given the limited system sizes it was possible to use in *ab initio* electronic structure and Wannier calculations using CASTEP [41], we were restricted to the simulation

Compound	Rock Salt	Zinc Blende	CsCl	Liquid
Unit cell composition	4NaF	4NaF	NaF	4NaF
UC's per simulation cell $xxyxz$	2x2x2	2x2x2	3x3x3	2x2x2
Temperature	1000 K	500 K	800 K	2000 K
Equilibrated dimensions	$19.30a_0$	$19.55a_0$	$18.52a_0$	$22.57a_0$

Table 3.3: Structural information about the four NaF systems set up for fitting purposes.

Species	F^-	Na^+
rock salt	$(0,0,0)$ $(0,\frac{1}{2},\frac{1}{2})$ $(\frac{1}{2},0,\frac{1}{2})$ $(\frac{1}{2},\frac{1}{2},0)$	$(\frac{1}{2},0,0)$ $(0,\frac{1}{2},0)$ $(0,0,\frac{1}{2})$ $(\frac{1}{2},\frac{1}{2},\frac{1}{2})$
Blende	$(0,0,0)$ $(\frac{1}{2},\frac{1}{2},0)$ $(0,\frac{1}{2},\frac{1}{2})$ $(\frac{1}{2},0,\frac{1}{2})$	$(\frac{3}{4},\frac{1}{4},\frac{1}{4})$ $(\frac{1}{4},\frac{3}{4},\frac{1}{4})$ $(\frac{1}{4},\frac{1}{4},\frac{3}{4})$ $(\frac{3}{4},\frac{3}{4},\frac{3}{4})$
CsCl	$(0,0,0)$	$(\frac{1}{2},\frac{1}{2},\frac{1}{2})$

Table 3.4: Fractional coordinates of the atoms within the unit cell for the three crystalline NaF structures.

cells described in Table 3.3. The number of electrons this involved was the same within our choice of pseudopotentials, giving a total of 512 (one per Na and seven per F to represent the electrons considered to be non-core): any larger potential choice of cell would have put this number beyond tractability. However, we chose three configurations from each structure to run *ab initio* calculations on, to improve the statistics for our fits, giving a total of 192 forces from each of the rock-salt, blende and liquid configurations, and 162 from the CsCl. We used a 'stock' ultrasoft pseudopotential [42] for fluorine and a standard norm-conserving one for sodium, and we verified that by our energy cut-off of 1000eV the forces had converged.

From the Wannier localizations we plotted out a selection of the Wannier functions, and a picture from one of the liquid configurations is shown in Figure 3.2. We see three p-type orbitals located on fluoride ions, the grey and yellow denoting the signs of the lobes. The black and green spheres represent the Na^+ and F^- ions respectively. We also see two of these orbitals lying orthogonal to one another on the same ion, all reassuring that both the electronic structure calculations and the Wannier functions derived therefrom have run successfully.

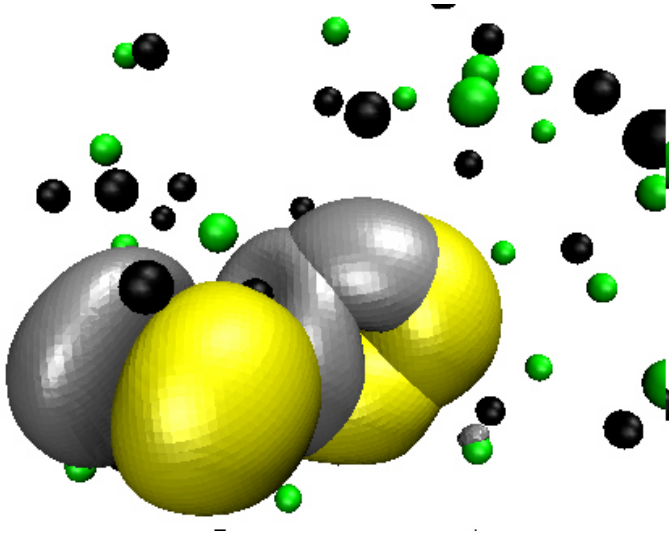

Figure 3.2: Three maximally localized Wannier functions in liquid NaF, plotted as volumetric datasets using VMD.

3.2.3 Step three: First Fitting of Pair Potentials for NaF

Having obtained the forces and dipoles for each configuration we began the fitting process. We started fitting using the simplest model, the RIM, then the DIPPIM model. In both cases we were only fitting to the force-data, though varying all of the parameters, including the dipole parameters α_F, b_{FNa} and c_{FNa} in the latter instance. We went through the fitting process by using each structure separately, then all configurations together in one large fit, and the results are given in Table 3.5 in terms of fit quality χ^2.

Structure	rock-salt	blende	CsCl	liquid	all
RIM	0.2691	0.3377	0.617	0.1572	0.4406
DIPPIM	0.0561	0.2197	0.0370	0.0497	0.1119

Table 3.5: First NaF fitting results in terms of χ^2 for the configurations of each structure and all structures together, using RIM and a DIPPIM potential models.

The improvement on adding polarization to the model is striking: in terms of the fit quality it goes from reducing χ^2 by one third for the blende structure, to reducing it by over a factor of four for the rock salt. The RIM fit quality would not be classed as 'bad' however - we consider a χ^2 of 0.1 or less to be 'good' - and

this can be ascribed to the fairly regular ionic structures in the crystals as well as the large difference in electronegativites which would justify the liquid results, as discussed above.

It was difficult to make sense of the relative fit qualities of the respective structures here. It could be expected that as the temperature is raised in the order blende<CsCl<rock-salt<liquid, the increasingly distorted environments would prove more and more of a challenge to the fitting program, but this is not the order we see. However, in the process of fitting we came to the conclusion that the fitting program had trouble navigating the potential energy surface with respect to this number of parameters. In particular, trying to fit the more 'delicate' polarization parameters alongside the short range parameters resulted in the polarization and charge dipole damping parameters taking unrealistic values in some cases, as well as some of the short range parameters pushing towards unrealistic boundaries, presumably compensating for one another where the fitting program had become stuck in a local minimum which was some way off the mark of the global minimum. Bearing this in mind we can regard these first results as only a rough indicator of what to expect from a more careful undertaking of the fitting, and the relative values between structures would have little meaning.

3.2.4 Fitting a Polarizable Potential for NaF

As a next step therefore, we chose to fit the multipole parameters first, separately, as described and justified in the previous chapter. The results are given in Table 3.6.

The resulting dipolar fit qualities are excellent in every case. What is more, we see an approximate increase in fit quality as the temperature of the configurations is lowered, which is something more of an indicator that the fitting program is finding global minima when using this subset of parameters instead of fitting all at once. The values of the dipole polarizability are all physically reasonable though somewhat larger than the value of 6.78 atomic units from the empirical potential in the work

Structure	χ^2_{dip}	α^F_{dip}/au	χ^2_{quad}	α^F_{quad}/au
rock salt 1000 K	0.00976	9.43	0.335	1.50
blende 500 K	0.0136	8.47	0.156	2.25
CsCl 800 K	0.0224	8.75	0.401	1.68
liquid 2000 K	0.0343	10.15	0.401	1.68
all	0.0245	9.18	0.312	1.68

Table 3.6: Polarization parameters for NaF arising from fit to dipoles and quadrupoles. Polarizabilities are given in atomic units.

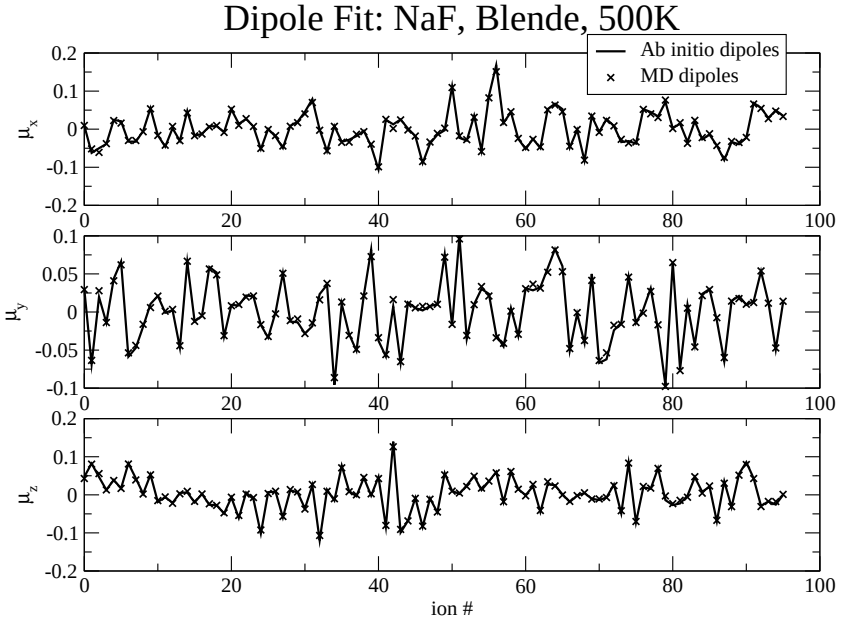

Figure 3.3: Comparison of *ab initio* and fitted dipoles in NaF for the blende structure for a dipolar potential. The abcissa represents the index of the atom, the three configurations placed in sequence, and the ordinate gives values for the dipoles in atomic units.

leading up to this [4]. However these values were subsequently justified by direct calculations of the fluoride ion polarizability [36], which gave values in a variety of crystals in the same range as produced by the fitting process. The quadrupolar fit qualities here are not so good, and we can possibly ascribe this to the relatively low-polarizing nature of the systems where quadrupolar effects play a relatively small role, so the effects are so small as to be hard to fit to.

Following this, we re-fit the forces using a dipolar level potential, optimizing the short-range parameters again while holding the polarization parameters constant at

the newly obtained values, choosing the set from the fit containing all structures. This time a very thorough process of testing the ranges and step-values in the fitting program was carried out for each and every structure to make extra sure a global minimum was reached. The results are given in Table 3.7.

Structure	rock-salt	blende	CsCl	liquid	all
χ^2	0.05019	0.05076	0.04165	0.04864	0.05406

Table 3.7: Force-fitting results, in terms of χ^2, for the series of NaF configurations, by optimization of the short-range parameters post-multipole fitting.

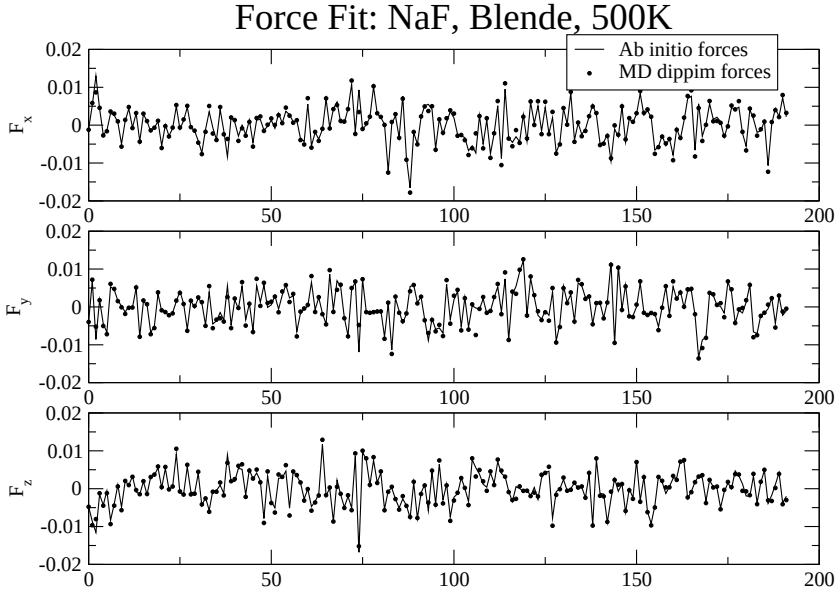

Figure 3.4: Comparison of *ab initio* and fitted forces in NaF for the blende structure for a dipolar potential. The abcissa represents the index of the ions, the three configurations have been placed one after the other along the abcissa, and the ordinate gives the values for the forces (in atomic units).

On average, we see a significant improvement in all of these force fits, having optimized the dipole parameters first. The better fit quality is particularly impressive for the fit containing all configurations. This further validates our method whereby we fit the two independent subsets of parameters separately, and in the fitting hereon this is how we shall start. On moving from a dipolar to a quadrupolar level potential however, we saw no improvement in the fit quality. This backs up our suggestion

that for this system, quadrupolar effects are insignificant enough to make fitting any potential of a higher order than the dipolar level unfeasible.

A plot which compares the *ab initio* to the fitted dipoles is shown in Figure 3.3, and one which compares the forces in a similar manner is shown in Figure 3.4, choosing the blende structure as the example here. The abcissa in this type of plot, which will be used throughout this work, represents the index of an ion in a configuration of the structure indicated and the ordinate gives values for the quantity (force, dipole *etc.*) chosen for comparison for that ion. These plots reveal just how accurate the fitted forces and dipoles are with our potential model.

3.2.5 Fitting a Potential at Differing Densities

Taking into consideration the density at which we had been fitting to this point, it could be argued that rather than fit at the equilibrium density of the empirical potential, it would be more useful to generate configurations at the experimental density to use in the fitting process as these would be more representative of the real system. The experimental density of NaF is 2.84 grams/cm^3 at ambient pressure and temperature and 1.948 grams/cm^3 in the molten state [43]. Table 3.8 gives the densities we had been using in the configurations used so far, all somewhat lower than the experimental densities.

Structure	rock-salt	blende	CsCl	liquid
ρ / gcm^{-3} (equilibrium)	2.10	2.02	2.00	1.31
ρ / gcm^{-3} (modified)	2.75	2.65	2.70	1.95

Table 3.8: Densities of the simulations of NaF.

Therefore, we tried repeating the fitting process at the experimental density: generating configurations using simulations at constant volume with the appropriate cell dimensions, running *ab initio* CASTEP calculations on them, then fitting the polarization parameters to the multipoles followed by the short range parameters to the forces. The cell size for the liquid configurations was unambiguous, but for the high temperature crystalline configurations for which we wish to fit forces, the

experimental density quoted needed to be scaled down a little. The precise value not being too significant for our purposes, and the optimum densities of the non-rock-salt structures also being a point of ambiguity, we chose to use the densities in the second row of Table 3.8. The results of fitting the subset of polarization parameters are given in Table 3.9.

Structure	χ^2_{dip}	α_F/au	Wannier spread range
rock salt, low ρ	0.00976	9.43	1.288-1.424
rock salt, high ρ	0.02872	6.61	1.143-1.308
blende, low ρ	0.0136	8.47	1.259-1.380
blende, high ρ	0.0117	7.17	1.152-1.332
CsCl, low ρ	0.0224	8.75	1.232-1.330
CsCl, high ρ	0.0784	6.51	1.034-1.347
liquid, low ρ	0.0343	10.15	1.222-1.526
liquid, high ρ	0.0394	7.84	1.153-1.462
all, low ρ	0.0245	9.18	N/A
all, high ρ	0.0283	7.07	

Table 3.9: The results of fitting polarization parameters for NaF at differing densities.

Firstly we see that on increasing the density, the fit quality decreases. This is not surprising, as pushing the ions up closer together increases the strength of the interactions and will only accentuate any existing deficits in the potential model. However at this quality of fit for all densities, changes of this magnitude in the value of χ^2 do not give any cause for concern. Just as important a factor in deciding to use the higher-density potential parameters for both the short range and polarization interactions, is that fact that the potential here has been fit to data which samples that in the real structure, despite the poorer fit quality.

In addition to seeing the effect on the fit quality, we find some interesting trends in the polarizability and the 'spread' of the Wannier functions, a measure of the size of the orbitals, on increasing the density. We see that both the polarizabilites on the fluoride ions and the 'size' of the orbitals associated with them decrease on compressing the crystal to a smaller volume: as the compressing effects of the fluoride ion's environment increases, the ions become less diffuse as reflected by

the Wannier spreads and thereby become less distortable/polarizable. This is an interesting new way of demonstrating that a previously-made hypothesis works, with regard to the polarizability of ions decreasing as the crystal lattice size decreases and the confining potential increases [44]. This hypothesis has also been justified in the study directly calculating polarizabilities mentioned in the previous section. Bringing the fitting density up to match the experimental density can also be seen to cause the polarizability to drop to something closely resembling the magnitude of the empirical value. This suggests we have reached the stage of being able to produce potentials from purely *ab initio* considerations with an accuracy in the parameters that has only previously been obtained through fine-tuning to experimental data.

Considering the effect of the density on the polarization parameters, and the fact that the polarizabilities are constants in our model, we chose to use the polarization parameters from a fit omitting the liquid configurations which had a much lower density. This way we obtain parameters which are more taylored for the solid phase. Repeating the force fitting process for the crystalline configurations at the approximate experimental densities, we obtained excellent fit qualities for each of the structures, χ^2 lying in the range 0.0043-0.0424, an improvement on the lower density fits. The resulting potential is given in Table 3.10. This completed the potential fitting process for NaF up to the point where the AlF_3 and NaF pair potentials needed to be combined.

χ^2	B_{FF}	B_{FNa}	B_{NaNa}	α_{FF}	α_{FNa}	α_{NaNa}
0.0172	20.07	67.96	10.20	1.883	2.069	4.666

Table 3.10: The short-range potential and fit quality resulting from fitting all crystalline NaF configurations at the approx. experimental densities. The B and α values are given in atomic units.

3.2.6 Combining the AlF_3 and NaF Potentials

In the process of fitting an AlF_3 potential we obtained a new set of short range F-F parameters as well as a new value for the polarizability. In order to make a

decision as to which would be best to use, we had to consider more than just the fit quality, which in fact proved to be slightly better in the NaF fits. If we take into account the respective structures and interactions therein, in the AlF_3 configurations the fluoride ions sample a more anisotropic environment where polarization plays a bigger role, giving the fitting process better data to work with for the purpose of optimizing multipole and and short-range interaction parameters. Also, the fluorine environments are much more similar to those in cryolite for which this potential is principally aimed. Therefore it was the AlF_3 F-F short range and fluoride polarization parameters that we chose for our best potential.

For consistency, we went back to re-fit the NaF potential, holding the aforementioned parameters fixed in the model. To complete the process for NaF, we try fitting using each level of potential model (acronyms explained in the appendix), and the results are given in Table 3.11.

model	DIPPIM	QUADPIM
RIM	0.01715	0.01625
CIM	0.01692	0.01626
DAIM	0.02063	-
QUAIM	-	0.02111

Table 3.11: Force fit quality for NaF resulting from adding physical effects to the model, stepwise.

This time there is a very small but consistent improvement in fit quality on the addition of quadrupoles to the model: the quadrupolar effects in NaF may have been too small to provide good data for optimizing a quadruploar potential, but on using the parameters optimized from a system where the effect is strong, the description of the small quadrupolar effects that are present benefits. It can be seen that the addition of ion deformation to the model does nothing to improve the fit quality, NaF providing too non-distorting an environment. There is in fact a slight increase in χ^2, owing to the additional parameters making the energy landscape more complex for the fitting program to navigate.

3.3 AlF_3

AlF_3 is a compound which has several phases, though under atmospheric pressure the two predominant ones are the low temperature rhombohedral α-phase shown in Figure 3.5, which undergoes a transition to the cubic phase with an ReO_3 structure at 729 K [45]. Both structures consist of a 3-dimensional network of corner-sharing AlF_6 octahedra, each Al^{3+} bridged by six 2-coordinate fluoride ions. The two structures are very closely related: in the ReO_3 structure the Al-F-Al-F chains are linear in all three directions, but become slightly concertinaed on going to the α-phase. The melting point is 1563 K [46].

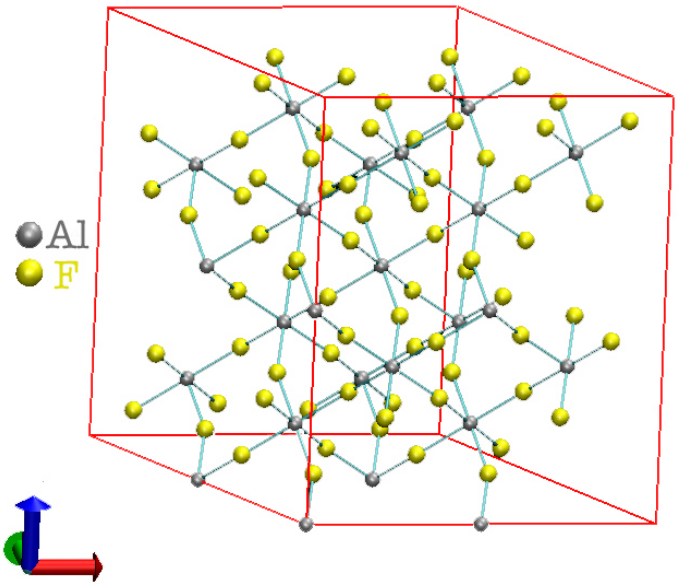

Figure 3.5: Rhombohedral α-AlF_3.

3.3.1 AlF_3 Configurations and *ab initio* Calculations

An empirical potential for AlF_3 was developed and thoroughly tested in previous work [47], and the parameters are given in Table 3.12. The Al-Al short-range parameters from cryolite's empirical potential, from which extracted the initial NaF values, are set to zero; the aluminium ions being so widely spaced in cryolite that the short-range overlap was considered to be negligible enough to omit from the model. This is not so much the case for AlF_3 which has a higher Al density, and

along with the reason of the potential from Chaudhuri *et al.* [1] being well-tested on pure AlF_3 itself, it appeared that this was the best choice for generating our starting configurations.

quantity	α	B	C_6	C_8	f_6	f_8
F-F	2.164	122.77	45.34	487.89	2.9	2.9
Al-Al	2.2	99.5	1.0	0.0	1.9	1.0

Table 3.12: Empirical pair potential parameters [47] used to generate AlF_3 configurations for fitting. Values are given in atomic units.

unit cell lengths	$a = b = c = 6.722a_0$
cell angles	$\alpha = \beta = \gamma = 90°$
unit cell comp.	1 AlF_3 unit
fractional crds (F)	($\frac{1}{2}$,0,0) (0,$\frac{1}{2}$,0) (0,0,$\frac{1}{2}$)
fractional crds (Al)	(0,0,0)
simulation cell	2x2x2 = 32 ions/192 e^-
	3x3x3 = 108 ions/648 e^-

Table 3.13: Structural information about the cubic phase of AlF_3, and details about the simulations cell.

We chose to use the cubic phase in fitting, and generated configurations accordingly. We ran simulations at 800 K and 1200 K in order to gain a wide range of degrees of thermal distortion in the crystals, where the distortion would mirror the the effects of the bent Al-F-Al bridges on the fluoride ion's environment in the α phase. The cell parameters have been reported for both phases [45], and the values for the ReO_3 structure are given in Table 3.13. We had the choice of a simulation cell consisting of two or three unit cells cubed, and in the end we used both: in practice we found the many of the 108-ion configurations were beyond the ability to run *ab initio* calculations using the architectures available to us. We chose Ultrasoft pseudopotentials for both Al and F in the *ab initio* runs, which explicitly modeled three and seven electrons respectively, corresponding to the non-'core' shells. This gave a total of 192 or 648 electrons. With our stringent energy cut-offs of 1000eV we would not normally expect to be able to simulate a system of much more than 500 electrons, so the second system was indeed pushing the size-limit.

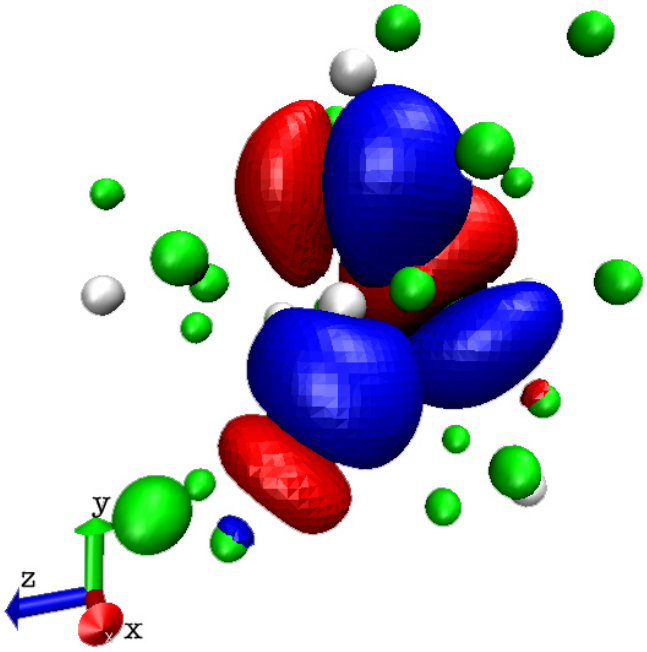

Figure 3.6: Three Wannier functions representing 'p'-type orbitals centred on F^- ions in AlF_3, illustrated from volumetric data sets. (Green and silver spheres = F^- and Al^{3+} respectively.)

The *ab initio* calculations on AlF_3 in the ReO_3 structure ran successfully, and a selection of the Wannier functions are shown in Figure 3.6. As for NaF, we see *p*-type orbitals centered on the fluoride ions, the Al ions having lost all of their valence electrons.

3.3.2 Fitting a Polarizable Potential for AlF_3

The results of the NaF fitting confirmed to us the need for polarization in even the most symmetric structures, so we began the fitting process at the dipolar level, and by fitting the two subsets of parameters - the polarization and the short-range - separately. We began by fitting the polarization parameters, and the results from three types of configurations are given in Table 3.14.

This time as well as the dipole fits being excellent, the quadrupole fits (with one exception) are also very good. The best dipole-χ^2 in particular drops to an astonishingly low value of 0.00529 (where we consider 0.1 to be 'good'). Also, we see a consistency in the values of the resulting parameters here which reassures us

configuration	$\chi^2_{dip}/10^{-3}$	α_F^{dip}	b_{damp}^{FNa}	c_{damp}^{FNa}	χ^2_{quad}	α_{quad}^{F}
3x32 ions at 800 K	5.29	6.792	2.050	1.558	0.2193	1.386
1x108 ions at 800 K	6.09	6.913	2.102	1.621	0.06458	1.417
3x32 ions at 1200 K	10.27	6.769	2.153	1.729	0.02787	1.577

Table 3.14: Results of fitting the polarization parameters for AlF_3, with values presented in atomic units.

that the fitting process is finding an approximate global minimum, and also that a distinct global minimum exists for AlF_3 using our model, independent of the temperature, cell size and configurations used.

The good fit quality of the quadrupoles in AlF_3 can be ascribed to quadrupolar effects playing a significant role in the interactions in this less symmetric structure with more highly polarizing triply charged cations. In these thermally distorted configurations the fluoride ions occupy a bent two-coordinate site, experiencing a large electric field and field gradient, inducing significant dipoles and quadrupoles respectively. The values of the dipole polarizability α_F^{dip} are in the same approximate range as those predicted by fitting NaF at the experimental density.

Holding these polarization parameters fixed, we went on to fit the short-range parameters for the respective configurations, using a dipolar potential model, and the results are given in Table 3.15.

configuration	3x32 ions at 800 K	1x108 ions at 800 K	3x32 ions at 1200 K
χ^2	0.0996	0.0456	0.0461

Table 3.15: Results of fitting the short range parameters for AlF_3 using a dipolar-polarizable model.

The fit quality at the dipolar level proved to be excellent in the latter two configurations and good in the first, showing that a dipolar model can describe the interactions in AlF_3 well.

3.3.3 Fitting Higher Order Potentials for AlF_3

With the improvements seen on adding quadrupoles to the polarization model, unlike in the case of sodium fluoride it is conceivable that raising the level of the potential further to incorporate ion deformation would lead to even better fits. Therefore, as a next step we tried fitting potentials across the full range of models described in the previous chapter. DIPPIM and QUADPIM are the non-deformable cases. The three CIM acronyms represent systems where the anions size is permitted to breath with no, dipolar-, and quadrupolar-polarizabilites. DAIM represents dipolar symmetry deformation and polarization plus breathability, and QUAIM adds quadrupolar symmetry deformation and polarization to the DAIM model. The results in terms of χ^2 are shown in Table 3.16 for the case of the 108-ion configurations at 800 K.

model	DIPPIM	QUADPIM
RIM	0.0456	0.0183
CIM	0.0455	0.0182
DAIM	0.0506	-
QUAIM	-	0.0182

Table 3.16: Force fit quality for AlF_3 resulting from adding physical effects to the model, stepwise.

Looking across the table, we can see in each case that by increasing the level of description of the polarization to the quadrupolar level we improve the force-fit quality. However we see on looking down the table that adding deformation of any type does not make a significant difference. From these observations we can conclude that quadrupolar effects are significant in the system, owing to the highly polarizing nature of the fluoride sites. Shape deformation, like polarization, is a consequence of an asymmetric/distorted environment and the two often go together, however in the case of AlF_3 with approximately linear coordination, there are not any neighbours around the Al-F-Al bond equator to have a distorting effect through overlap, so there is not the information present in the data that the fitting program would require to optimize the parameters associated with these effects. Therefore the quadrupolar-

RIM model is as high a level of potential we can hope to fit well using either the cubic or α-structure of AlF_3.

3.4 Choosing the Appropriate Potential for Simulation

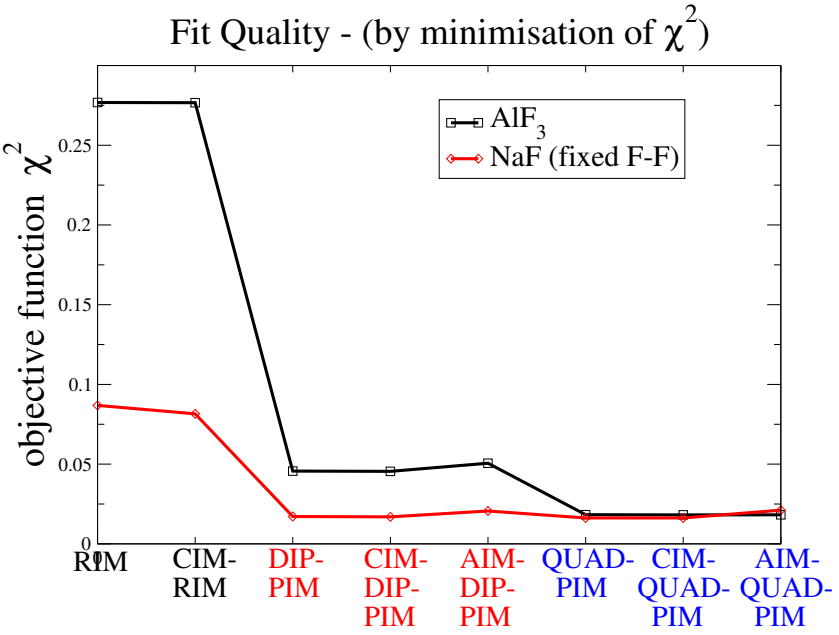

Figure 3.7: Showing how the quality of the fitted potentials changes for NaF and AlF_3 by increasing the complexity of the potential model.

Figure 3.7 shows the improvement in force-fit quality as we add greater detail to our description of the physical effects in the potential model, along the abcissa. For both the NaF and AlF_3 fits it is the introduction of polarization at the dipolar level that can be seen to cause by far the largest improvement in fit quality. In AlF_3 in particular, χ^2 drops by over a factor of five between the rigid ion and dipolar polarizable models.

The most basic 'rigid ion' model proved to be sufficient to produce 'good' fits only for NaF, whose bonding is of such a highly ionic nature that the correction to be gained by allowing formation of dipoles was relatively small. The highly symmetric site of the fluoride ions in NaF in all three crystal structures, in combination with

the relatively small cation charge of '+1', makes for a less polarizing environment. This is not the case for the fluoride ions in AlF_3, where the cation has a charge of '+3', and the coordination number is two, the anions forming non-linear bridges between the Al^{3+} ions in the thermally distorted configurations used. Consequently there is a sustained electric field and field gradient at the fluoride site in AlF_3, but not in NaF.

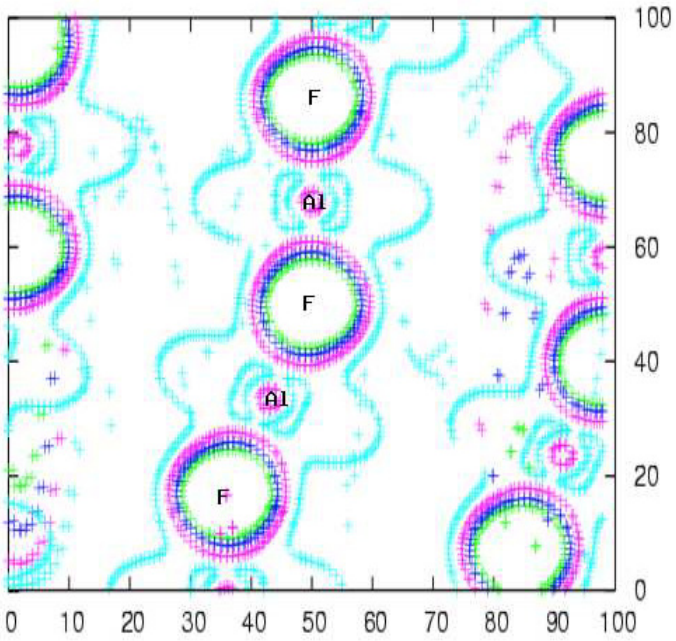

Figure 3.8: Two-dimensional slice of the electron density in the low-temperature perfect crystal structure of AlF_3, from a CASTEP calculation.

We performed CASTEP single-point calculations on a perfect crystal of the low-temperature, lower symmetry, rhombohedral α-phase of AlF_3, then produced data-sets that could be mapped out as 2-dimensional slices of the electron density through the crystal: one of these is shown in Figure 3.8. In this structure, the fluoride ions bridge bent Al-F-Al bonds, where the fields would be more representative of those in thermally distorted configurations of the ReO_3 structure. It can be seen that the fluoride ions are slightly elongated or polarized along the Al-F-Al bonds, emphasizing the need for polarization in any potential model. Beyond the dipolar level, by allowing quadrupoles to form on the anions we clearly saw a further improvement

in the fit quality for AlF_3 but negligible improvement for NaF, for the same reasons. We would expect the effect of introducing the two levels of polarization in cryolite to have a much more similar weight to the effect in AlF_3 rather than NaF, owing to the asymmetry of the anion site in cryolite - shown later in Figure 3.17.

Allowing for ion deformation did not have a significant impact on the fit quality for either AlF_3 or NaF. Although the crystallographic sites in AlF_3 sustain electric fields, and of course both compounds' sites do when thermally distorted, the structures are still highly ionic 3-dimensional networks, and it is plausible that it would take less typically ionic structures containing atoms with a greater covalent tendency for shape deformation to play an appreciable role.

Pair	B^{ij}	α^{ij}
F^--F^-	120.93	2.20
Al^{3+}-F^-	111.43	2.35
Na^+-F^-	73.79	2.10
Al^{3+}-Al^{3+}	93.26	2.91
Na^+-Na^+	163.76	4.73
Al^{3+}-Na^+	0.0	0.0

Table 3.17: Short-range parameters for the best choice of fitted dipolar pair potentials to work with to study cryolite. All values are given in atomic units. The dispersion parameters were set to zero.

α_F	$b_{F,Al}$	$c_{F,Al}$	$b_{F,Na}$	$c_{F,Na}$
6.70	2.10	1.65	1.71	1.87

Table 3.18: Polarization parameters for the best choice of fitted pair potential to study cryolite. All values are given in atomic units.

Despite small improvements to the fit quality on adding quadrupoles and ion deformation to the potential model, excellent fits to the *ab initio* forces for these configurations were obtained with potential models from the level that allowed for dipole polarization of the fluoride ions as the only many-body effect. A decision needed to be made as to which level of the potential model was to be used in the simulation study of cryolite to follow, and taking the consideration of computational

tractability on board alongside these relatively small improvements beyond the dipolar level, the simple dipolar potential seemed like the most appropriate candidate.

Values for all parameters for this chosen potential are given in Tables 3.17-3.18, where the significance of each parameter is shown in Equation 2.2. By fitting to pure AlF_3 and NaF we could not, of course, obtain an Al^{3+}-Na^+ pair potential; given the relatively tiny effect of the interaction of such widely-spaced pairs of ions, we thought it reasonable to omit a short-range repulsive interaction between this pair in our simulations.

3.5 The Structure and Dynamics of Cryolite

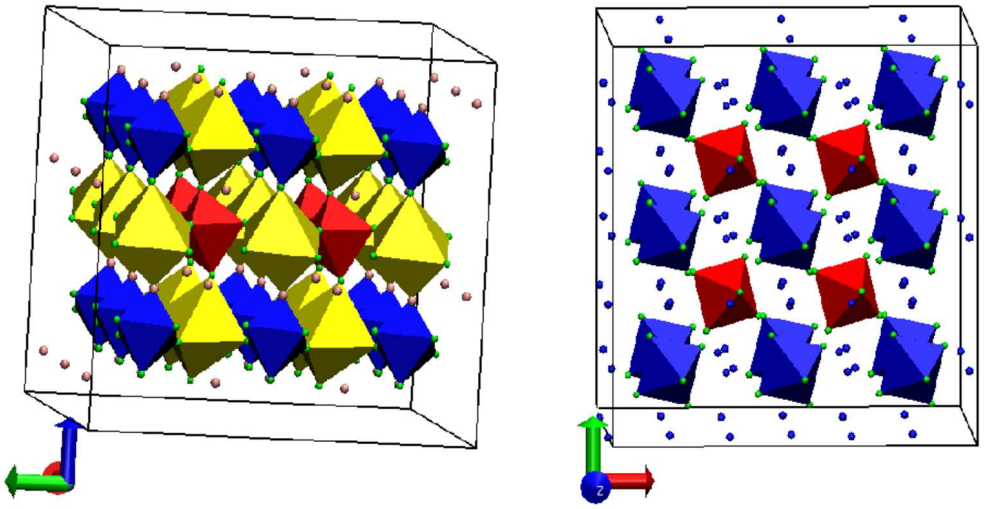

Figure 3.9: The low temperature crystal structure of cryolite. In the left-hand figure, the red and blue octahedra (at the centre of which lie the B sites) indicate the two tilt domains of the AlF_6 octahedra, and the NaF_6 octahedra (at the centre of which lie the B' sites) are shown in yellow. The A-site Na^+ ions are shown as small spheres. In the right hand figure the view down the c-axis is shown and the Na-centred octahedra have been omitted for clarity.

Cryolite, Na_3AlF_6, is a naturally occurring mineral which has the elpasolite crystal structure, a double perovskite ($A_2BB'X_6$) with Na^+ ions occupying both the A and B' sites, and Al^{3+} the B site [48]. As indicated in Figure 3.9 this structure may be viewed as a set of corner-sharing AlF_6 and NaF_6 octahedra (the B and B′-sites) with the remaining Na^+ ions occupying 8-coordinate holes in between these

octahedra (the A-sites). In many perovskites, the regular network of translationally symmetric octahedra is modified by tilting [49, 50], and this is true of the low-temperature phase of cryolite. Below 885 K, the AlF_6 (and NaF_6) octahedra adopt two tilt orientations and the overall crystal structure is monoclinic (but only slightly distorted from orthorhombic) with space group $P2_1/n$ [48, 51, 52]. At this temperature, thermal and optical measurements indicate the transition to a cubic structure occurs [53, 54] of space group F_m3_m [55, 56], with the octahedra aligned, on average, with the crystallographic axes [52]. NMR observations [12, 57, 11] and conductivity measurements [58] show that ionic diffusion in cryolite is surprisingly facile considering that the crystal structure does not appear to show the kind of empty sites characteristic of typical fast-ion conducting crystal, such as the fluorites [59]. In the fluorites such sites allow the formation of thermally activated Frenkel defects [15] and thus mobile vacancies and interstitial ions. In view of the interest in novel material properties of transition metal oxides with the double perovskite structure [60], it is of interest to examine the mechanisms which permit ionic motion in this structure, as this process could prevent the formation of substitutionally ordered phases in target materials.

Conductivity measurements show diffusion of the Na^+ ions persisting down to room temperatures [58]; because the Al^{3+}-F^- interaction is much stronger than that of the Na^+-F^-, the AlF_6 octahedral units remain stable species throughout the solid state. In the regime of rapid sodium diffusion, the structure can be regarded as an open framework of AlF_6^{3+} octahedra [61, 62]. All three of the nuclei have good NMR properties (which is not case for the more technologically relevant double-perovskite transition metal oxides), though ^{27}Al and ^{23}Na are quadrupolar, and there have been several NMR studies of the ionic motion [12, 57, 11]. These studies confirm the exchange of Na^+ ions between A and B′ sites; a rate constant of $\sim 200s^{-1}$ at 473 K is quoted in Lacassagne et al [57], far below the phase transition temperature. The NMR studies also demonstrate appreciable reorientation of the

AlF_6 octahedra [12] well below the phase transition, this results in a narrowing of the dipole and quadrupole broadening. There has been a good deal of speculation that these effects are connected, with the Na^+ motion facilitated by a paddle-wheel type effect involving the AlF_6 octahedra, by analogy with arguments used to explain the Li^+ diffusion in Li_2SO_4 *inter alia* [59]. Above the phase transition at 885 K the AlF_6 octahedra rotate with relative freedom and the Na^+ diffusion is sufficiently rapid as to be observable in quasielastic neutron scattering [63]. Finally, at 1290 K, cryolite melts.

3.6 Testing the Newly-fit Potentials

Crystallographic studies [48, 51, 52] show that in both high and low temperature phases, cryolite can be described as an alternating 3-dimensional network of corner-sharing AlF_6 and NaF_6 octahedra. In the high temperature structure all octahedra are on average aligned with the cell axes in the same manner: two axial bonds along the c or z direction and four orthogonal lying in the ab or xy plane giving an overall cubic arrangement. However, in the low temperature structure the AlF_6 octahedra tilt slightly from their common axes, alternating layers adopting different orientations that are related by reflection in the yz plane. The AlF_6 tilting necessarily causes the interconnecting NaF_6 to adopt a similar alternating tilt-pattern. The tilting results in a monoclinic space group, though the departure of the non-90° angle β is only 0.185° at 295 K and decreases steadily towards the phase transition at 885 K. In our simulations, at finite temperature, we are insensitive to such a small departure from an orthorhombic structure (with our choice of simulation cell, $a \neq b \neq c$, $\alpha = \beta = \gamma = 90°$) and we will discuss the comparison with the experimental structure on this basis.

3.6.1 The Crystal Structure

The fitted dipolar-polarizable potential was found to reproduce the low temperature crystal structure well. The average cell lengths from NPT simulations (at 300 K with

the above constraint on cell angles, at a pressure of 10^{-6}au) [64] are compared with those from X-ray diffraction at 295 K [48] in Table 3.19. The simulation produces a slightly larger unit cell, which is at least in part attributable to ignoring dispersion effects in the fitted potential [14, 31, 5].

Source	a	b	c	$\theta°$	$\phi°$
simulation	5.5121	5.5884	7.8385	19°	±30°
X-ray diffraction	5.4139	5.6012	7.7769	19.5°	±23.5°

Table 3.19: Unit cell lengths (given in Angstroms) and the angles (given in degrees) characterising the AlF_6 tilt domains.

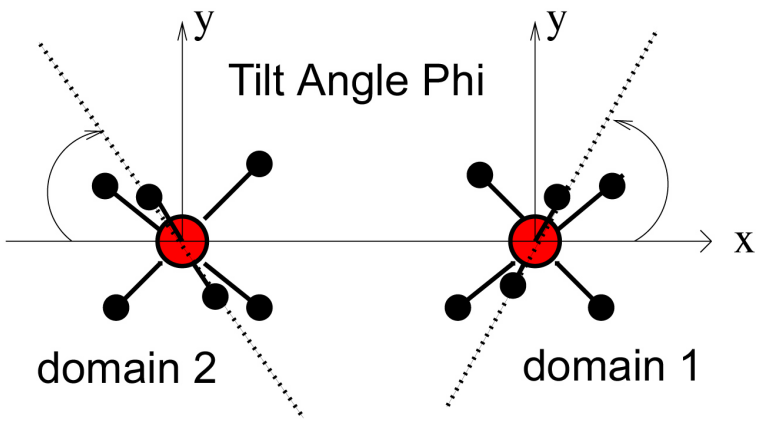

Figure 3.10: Showing the angles ϕ, the tilt orientations of the AlF_6 octahedra in cryolite for each of the two domains.

Angles ϕ and θ characterising the tilts of the AlF_6 octahedra are shown in Figures 3.10 and 3.11. The octahedra may be described as belonging to two tilt domains whose spatial arrangement is shown in Figure 3.9. They possess the same tilt of the axial Al-F bonds from the z axis (angle θ) and oppositely signed angles (ϕ) between the x axis and the projection of the axial Al-F bond onto the xy plane. Table 3.19 gives the average values of θ and ϕ from simulation and experiment at 295 K [48], and these compare well, particularly θ. Figure 3.12 also shows the distribution of angle θ in comparison with the experimentally derived value. Similar results for the low temperature structure are obtained with the empirically constructed potentials.

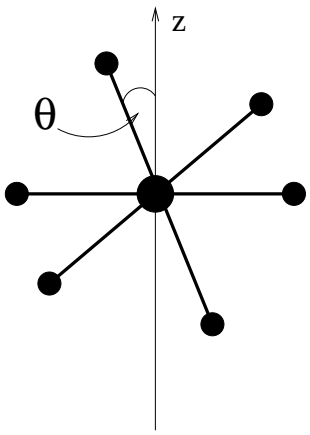

Figure 3.11: Showing angle θ, the tilt of the AlF_6 octahedra from the z-axis.

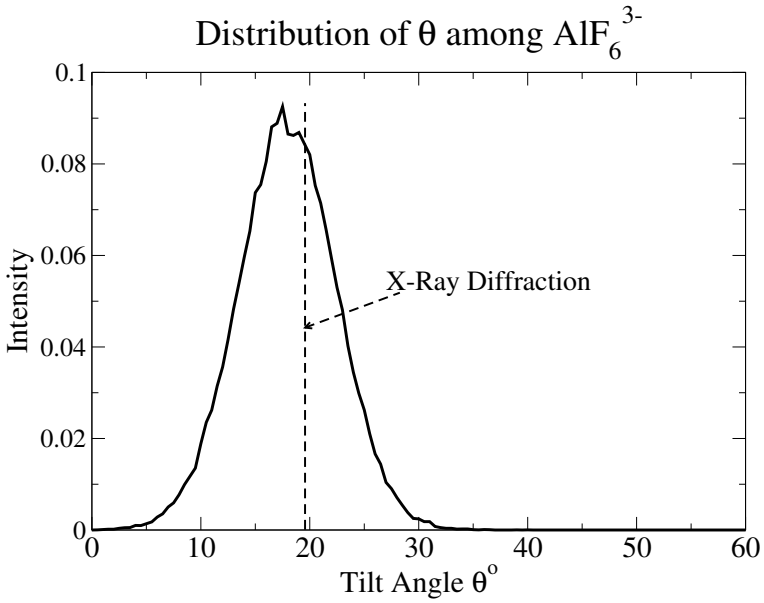

Figure 3.12: Distribution of tilt angle θ in the low temperature phase of cryolite under the fitted potential; comparison with the experimental angle.

3.6.2 The Phase Transition

Experiment shows that the enthalpy and volume differences between the low and high temperature phases are weak and the transition almost continuous [51, 58]. We have not been able to locate the transition by looking for sharp changes in structural parameters (such as cell lengths) or thermodynamic quantities, like the mean potential energy, in a series of NPT simulations as the temperature is raised, in the manner of the previous work on AlF_3 [1]. Instead we see a progressive change in the mean tilt angles of the AlF_6 units and in the anisometry of the simulation cell.

The evolution of the distribution of tilt angles with increasing temperature is illustrated in figures 3.13, 3.14 and 3.16. In Figure 3.13 the probability distribution of the axial tilt θ is shown; it is peaked about a non-zero angle of about 19° at the two lower temperatures and then broadens and re-centres about a zero tilt at the two highest temperatures illustrated (recall that the probability of seeing perfect alignment with the axis is zero). We will associate the temperature T_{trans} at which the distribution broadens and collapses with the phase transition temperature

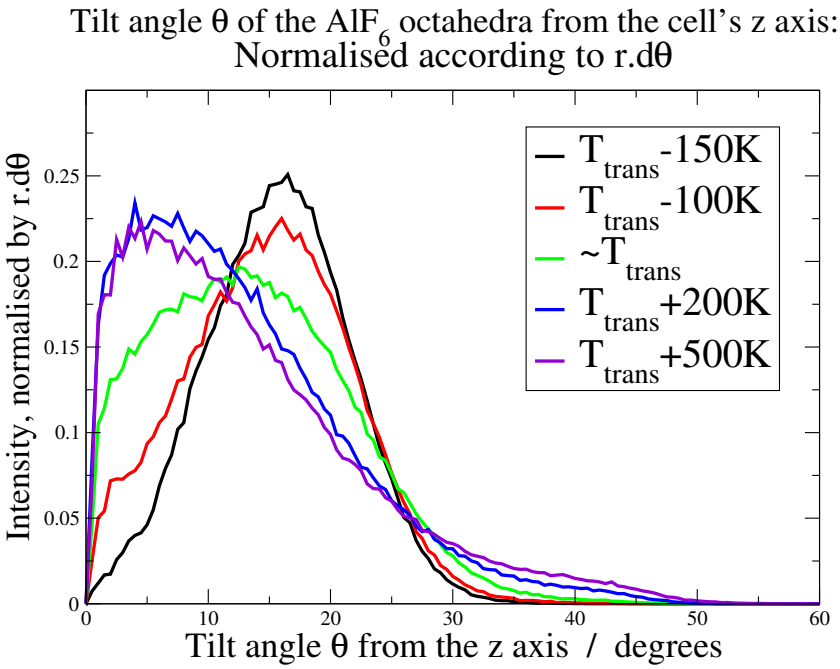

Figure 3.13: The tilt angle θ (degrees) in crystalline cryolite over a temperature range spanning the phase transition, under the fitted potential.

predicted by the simulation. The assignment of a transition temperature by reference to the distribution of tilts is supported by the evolution of average cell lengths, shown in Figure 3.15, which fit the orthorhombic pattern below T_{trans}. As the temperature is raised they coalesce fairly suddenly to give $a = b = c/\sqrt{2}$, consistent with cubic symmetry, at the same temperature as the tilt distribution re-centres about 0°. As we shall see in detail below, the dynamical properties of the AlF_6 units are also consistent with this assignment.

Figures 3.14 and 3.16 illustrate the corresponding behaviour of the angle ϕ; at the low temperature illustrated the distribution is peaked about a tilt of 30° and as the temperature is raised through and high above the phase transition (above T_{trans}) the distribution of the two domains coalesce to form a symmetrical and peak about zero tilt, reflecting the average value. Just below T_{trans}, as assigned above, in Figure 3.16 the distribution becomes symmetrical about zero but shows peaks at finite tilts of about 20°. We will discuss this effect as a consequence of tilt-swapping and examine the associated dynamics more closely in the next chapter. The dashed

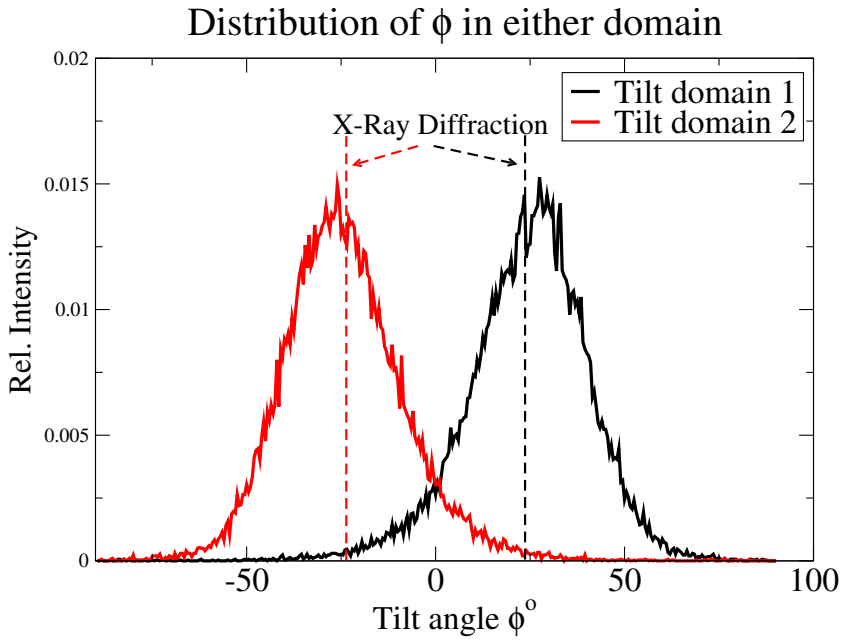

Figure 3.14: The tilt angle ϕ which distinguishes the two tilt domains, in crystalline cryolite at a temperature 200 K *below* the phase transition (300 K using the fitted potential).

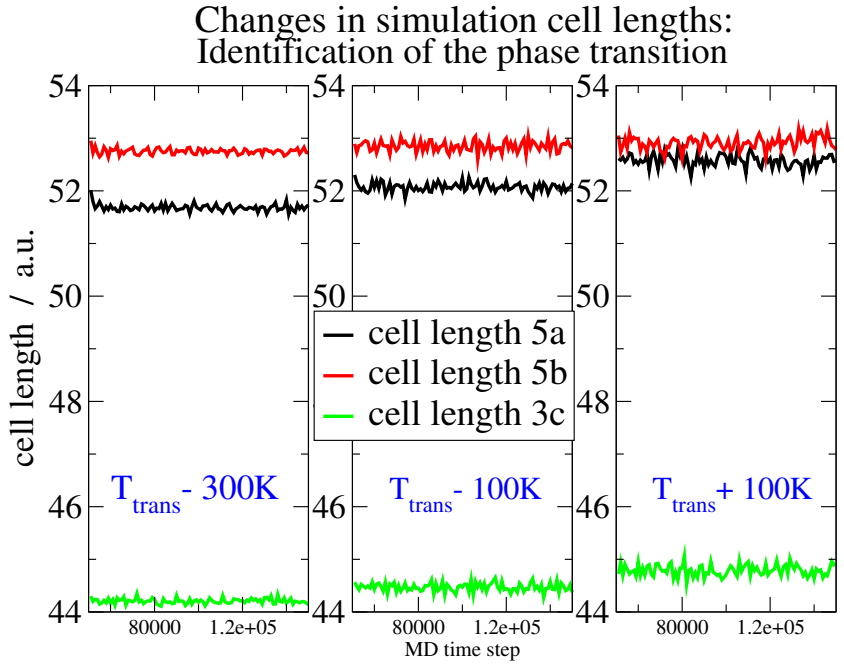

Figure 3.15: Showing the evolution of simulation cell lengths through the approximate point at which we identify the phase transition.

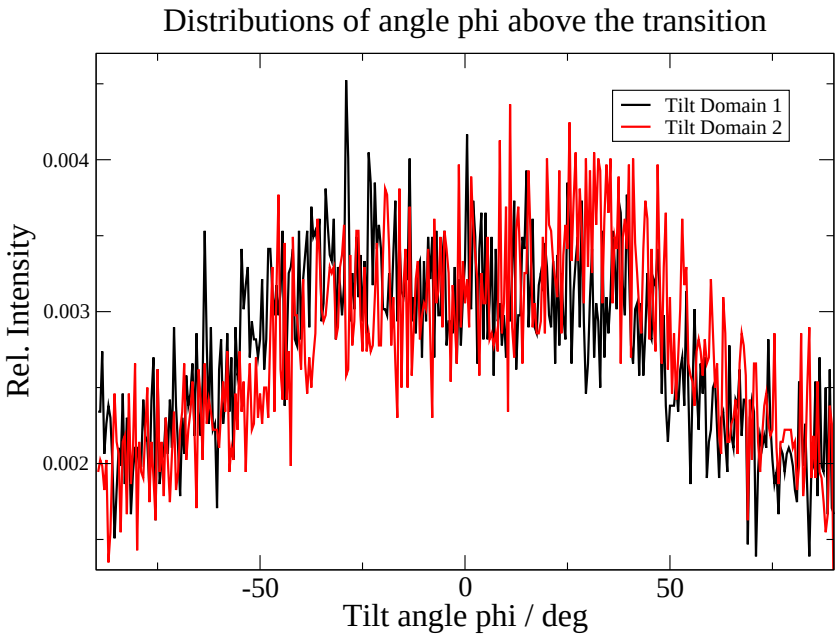

Figure 3.16: The tilt angle ϕ grouped into what would be the two low temperature domains, in crystalline cryolite at a temperature just *above* the phase transition (at 570 K using the fitted potential).

lines show the values of the tilt angles as derived from the crystallography studies, and it can be seen that they are in excellent agreement with the corresponding values in our simulation under the fitted potential.

Both the empirical and fitted interaction potentials produce a similar pattern of behaviour as the temperature is raised, and this extends to the dynamical information we will discuss below as well as the average structure. This suggests that this pattern is robust with respect to changes in the interaction model, it appears that the behaviour predicted by each of the potentials is very similar if they are compared at the scaled temperature T/T_{trans}, where T_{trans} is particular to each potential. However, the actual transition temperature T_{trans} does differ from one potential to another. The *ab initio* parameterised fitted potential gives best agreement with the experimental value (885K) with T_{trans}=550 K, with the transition temperature predicted by the two empirical potentials significantly lower (300-400 K). It appears that the value is particularly sensitive to the Na-F interaction parameters, as these are the parts of the potential which vary most significantly between the different

models (tables 3.1 and 3.17). This makes physical sense because for an AlF_6 octahedron to reorient, at least four neighbouring Na-F bonds must be broken. The actual value of T_{trans} is somewhat disappointing; however, as remarked above, we are dealing with a very weak transition and its location is sensitive to tiny energy differences between the two phases.

The fact that structural and dynamical behaviour is robust to changes in the potential and scales with T_{trans} suggests that we should compare the predicted and experimental observed behaviour at the corresponding scaled temperatures.

3.7 Direct Evaluation of the Fitted Potential and Iterating the Fitting Process

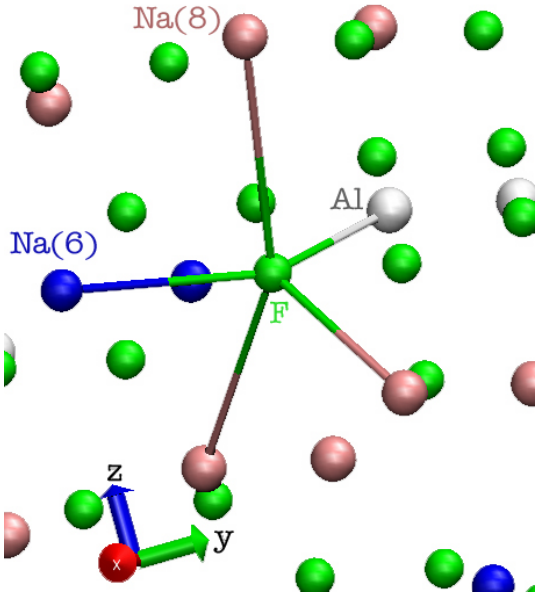

Figure 3.17: Showing the asymmetry of the crystallographic sites of the fluoride anions in cryolite. The numbers in brackets signify the coordination numbers of the sodium sites.

Another way of examining the fitted potential's ability to predict accurate properties for cryolite is by performing further *ab initio* calculations on cryolite itself and comparing the forces and multipoles with those predicted by the interaction model based upon the fits using the information from pure AlF_3 and NaF configurations.

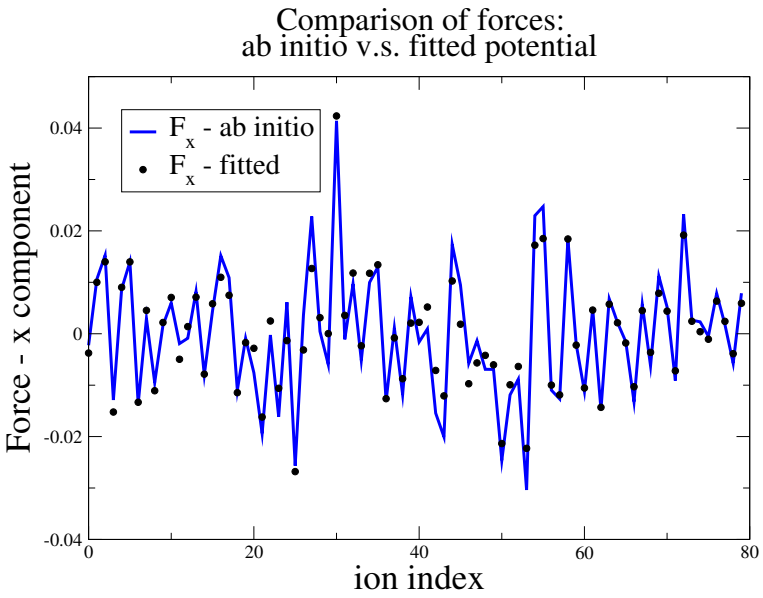

Figure 3.18: The forces (in a.u.) on the ions from *ab initio* calculations on a high-temperature configuration of solid cryolite (solid line) are compared with those predicted by the combined fitted (NaF and AlF_3) potentials (points) for cryolite.

As Figures 3.9 and 3.17 show, in cryolite the fluoride ions are sandwiched between triply charged Al^{3+} ions and singly-charged Na^+ so that they may be strongly polarized in a coordination environment not found in either of the pure materials; consequently, the transferability of the potential to this mixed system was not guaranteed. Nevertheless the comparison of dipoles and forces in Figures 3.19 and 3.18 shows that without further optimisation the fitted potential predicts the induced dipoles very well, and the forces quite well.

Given that the fluoride site in cryolite is even less symmetric than in AlF_3, we would expect the environment to have an even more polarizing and possibly distorting effect, so it seemed very possible that the potential could be refined further by using cryolite configurations as well as NaF and AlF_3. To this end, we tried iterating the fitting process. We generated cryolite configurations using the dipolar model potential fit using NaF and AlF_3, then performed *ab initio* calculations on them. Using the force and multipole data from cryolite itself, we repeated the fitting process, re-optimising the dipole parameters, followed by the short range parameters. The results in terms of χ^2 are given in Tables 3.20 - 3.21 alongside the equivalent

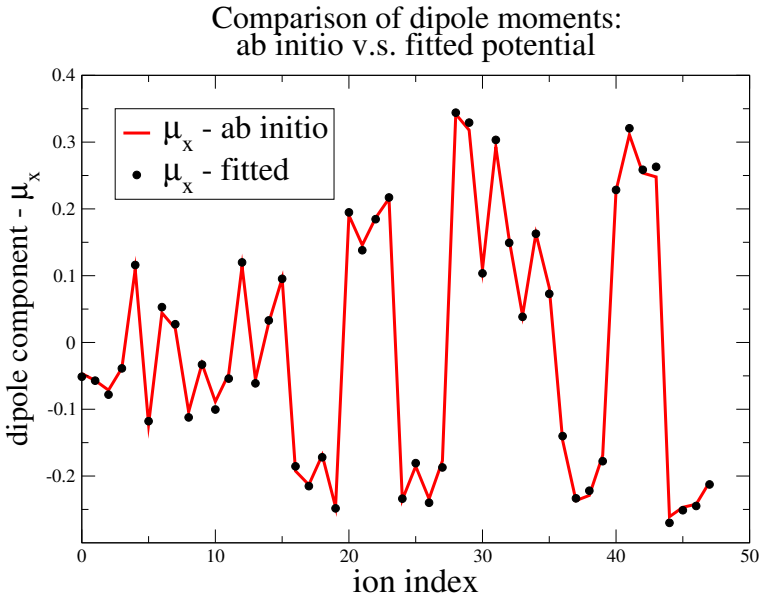

Figure 3.19: The dipoles (in a.u.) on the ions from *ab initio* calculations on a high-temperature configuration of solid cryolite (solid line) are compared with those predicted by the combined fitted (NaF and AlF_3) potentials (points) for cryolite.

results from the NaF/AlF_3 fits for comparison.

	before (AlF_3)	new (Na_3AlF_6)
dipole χ^2	0.00609	0.00137
quadrupole χ^2	0.06453	0.00719

Table 3.20: Multipole fit quality from the second round using cryolite configurations, compared with the quality from the first round using NaF/AlF_3 configurations.

Looking first at the multipole fits, we see a large improvement (a factor of *ca.* five) in the dipole-fit χ^2 on fitting using the cryolite configurations, and in the quadrupole χ^2 we see a massive improvement (a factor of *ca.* ten). The reasons for this we can understand by considering the symmetry of the fluoride sites, NaF>AlF_3 >Na_3AlF_6, where as the symmetry is lowered, there are increasingly strong polarization effects intrinsic in the multipoles we fit to. What is more, in perfect cryolite the fluoride sites sustain an electric field and field gradient, which is not the case in the solid NaF structures or the cubic AlF_3 we used for fitting the potential the first time around. The absolute values of the force-fit χ^2 in cryolite do not generally improve on the NaF/AlF_3, but as mentioned previously, where

	before (NaF)	before (AlF_3)	new (Na_3AlF_6)
no polzn	0.08681	0.2768	0.2654
DIPPIM	0.01715	0.04564	0.02577
QUADPIM	0.01625	0.01829	0.02756
CIM-DIPPIM	0.01692	0.04546	0.02564
CIM-QUADPIM	0.01626	0.01819	0.03011
DAIM	0.02063	0.05059	0.01927
QUAIM	0.02111	0.01820	0.01812

Table 3.21: Force fit quality: second round versus first round of fitting for cryolite.

we have more challenging short-range interactions to describe using our model, the fitting may result in a poorer value of χ^2 but actually produce a better interaction potential because of there being more complex physical effects at work, intrinsic in the data fitted to.

Pair	B^{ij}	α^{ij}
F^--F^-	54.34	2.01
Al^{3+}-F^-	22.70	1.79
Na^+-F^-	100.39	2.19
Al^{3+}-Al^{3+}	55.80	2.91
Na^+-Na^+	163.60	3.46
Al^{3+}-Na^+	149.65	4.50

Table 3.22: Short-range parameters in the fitted quadrupolar potential for cryolite, values given in atomic units.

	polarizability$_F$	$b_{F,Al}$	$c_{F,Al}$	$b_{F,Na}$	$c_{F,Na}$
dipole	6.91	2.07	1.55	1.78	2.11
quadrupole	1.54	2.61	2.13	2.31	3.50

Table 3.23: Polarization parameters in the fitted quadrupolar potential for cryolite, values given in atomic units.

Before moving on to an in-depth simulation study, we repeated simulations of cryolite under the newly fitted potential at the quadrupolar level, (the values of the parameters for which are given in Tables 3.22-3.23), and found that while the first-fit potential reproduced a qualitatively accurate picture of the structure and dynamics, this second round resulted in a new potential which was more *quantitatively* accurate,

giving a phase transition very close to the the experimentally observed one of 850 K. We can attribute this both to a more accurate potential to generate configurations with in the second round of fitting, and also to the environments of the sites in cryolite experiencing greater polarization effects than in NaF or even AlF_3 owing to the lower symmetry, which improved the data we had to work with in the fitting process.

In the next chapter we go on to investigate the structure and dynamics of cryolite using the newly fitted dipolar potential; more recently this same potential has been used in the investigation of molten NaF-AlF_3 systems and the calculation of Raman spectra [65].

Chapter 4

Study of the Ion Dynamics in Cryolite

After showing in the previous chapter that our newly-fit potentials reproduced the structure excellently, as well as the qualitative way the structure evolves with tempterature, we were in good standing to go on to study the ion dynamics of the simulations under these potentials.

While it is undisputed that a considerable amount of ionic motion occurs in solid cryolite, as described in section 3.5, there are some inconsistencies in the results obtained by different groups with regards to their nature and extent. NMR studies indicate the existence of extensive ionic motion but, as yet, they have not been able to present a consistent picture of the ion dynamics. Na_3AlF_6 should be an ideal material for refining NMR techniques to examine the motion of quadrupolar nuclei [11]: however, a notable feature of the NMR results is that there are inconsistencies at a quantitative level between results obtained by different groups and even between the results obtained by the same group on different samples (for example, natural and synthetic cryolite [12]). Furthermore, there are qualitative inconsistencies between the NMR picture of the solid as one sustaining a high degree of ionic motion even at about 450 K and that which emerges from the diffraction data, which indicate that the ions occupy well-defined crystallographic lattice sites with relatively small thermal ellipsoids even above the phase transition at 885 K. Simulations should, in principle, give insight into the character of possible motions and may indicate the

source of these inconsistencies.

Apart from the difficulty of obtaining a sufficiently good description of the ionic interactions to represent the real material, the different timescales of NMR observations and computer simulations present a substantial challenge to the use of the method to enhance the information coming from the experiments. The timescale of the NMR experiment is set by the frequency differences between different lines in the spectrum, and is of the order of 10^{-5} seconds or longer, whereas the total duration of an MD run is unlikely to exceed a nanosecond. Although we may make quantitative comparisons in either the static limit, where all motions are slow compared to the NMR timescale, or the opposite extreme narrowing régime, we cannot follow the evolution of the spectra between these limits. We can only follow the sequence of dynamical events which influence the NMR observations at elevated temperatures, where they occur on the MD timescale, and attempt to extrapolate the information back to the temperatures at which the observations are actually made. This has proven successful in a number of studies of ionically conducting solids [66, 67].

4.1 Octahedral Reorientation

In this section we will investigate the mechanism for the reorientation of the AlF_6 units, suggested by the structural measures discussed above. By octahedral reorientation we would mean any kind of rotational (non-vibrational, non-translational) motion of the AlF_6 octahedra, centred on the Al lattice sites, as seen in Figure 3.9. An immediate picture of this motion is obtained from the mean-squared displacement (MSD) of the F^- ions across a range of temperatures, as shown in Figure 4.1. At low temperatures ($\frac{T}{T_{trans}} < 0.8$), a constant amplitude of <0.4 bohr is maintained throughout the simulation, indicating librational motion of the AlF_6 units.

As the temperature is raised the MSD drifts steadily higher above the vibrational plateau, and at temperatures of about 500 K or more above the phase transition we see this drift tending to a second, higher plateau within the length of the simulations

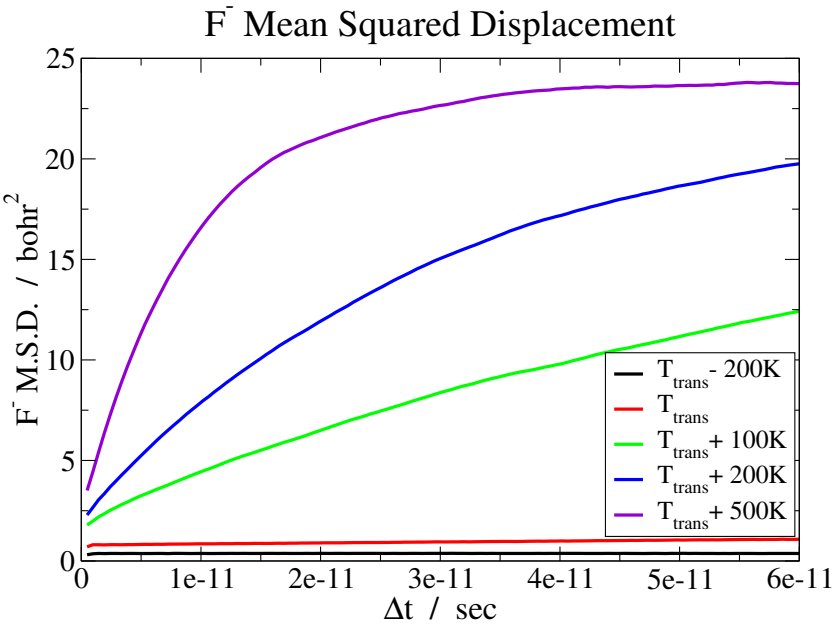

Figure 4.1: Mean squared displacements of the F^- ions in a simulation of cryolite with the dipolar fitted potential.

(6×10^{-11} secs). This second plateau corresponds to an amplitude of around 5 bohr, which can be assigned without doubt to rotational motion: the AlF_6 are discrete, long-lived molecular units on our timescale with an Al-F bond length of approximately $\frac{5}{\sqrt{2}}$bohr, and in a freely rotating octahedron the most probable distance for a vertex to have moved in a time interval much greater than the rotational correlation time corresponds to $r_{Al-F}\sqrt{2}$. At no temperature in the solid phase do we see any further increase of the F^- MSD, which would indicate break-up of the AlF_6 units.

Secondly we calculated the orientational correlation functions of the AlF_6, as shown in Figure 4.2: the P_2 function correlates each Al-F bond vector at time 0 with itself at a time t, its value gives the mean value of the second legendre polynomial of the cosine of the angle, $\Delta\chi$, through which a bond has wandered and has the same angular dependence as the interaction between a pair of dipoles; the dipolar contributions to NMR lineshapes will reflect the character of this function:

$$P_2(t) = \langle \frac{1}{2}(3\cos^2(\Delta\chi(t)) - 1) > . \tag{4.1}$$

At low temperatures ($\frac{T}{T_{trans}} < 0.8$) P_2 quickly decays to a plateau which is then

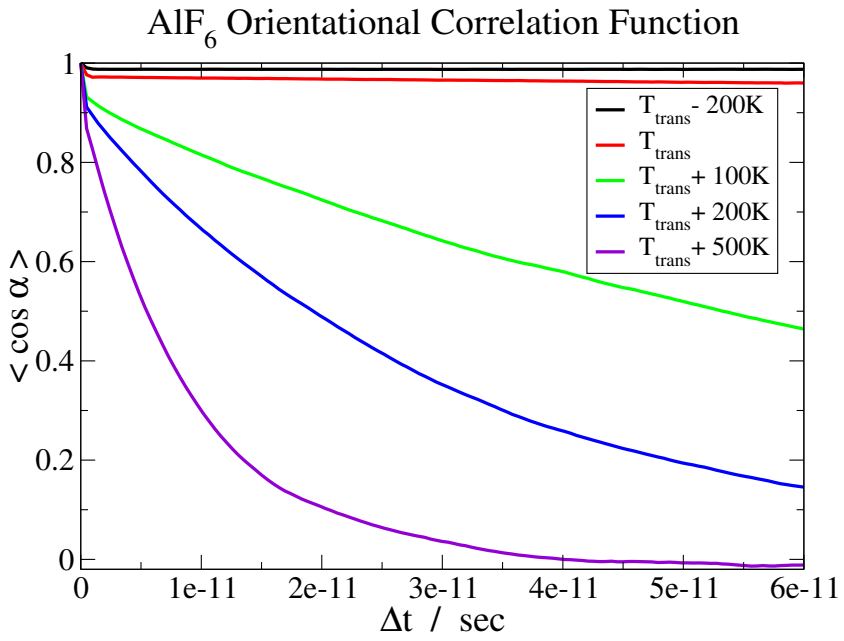

Figure 4.2: Orientational correlation functions of the AlF_6 octahedra in cryolite.

maintained on the simulation timescale. The initial decay is primarily due to the librational motion of the AlF_6 units about their average tilted orientation. The plateau indicates that the mean octahedral orientation is maintained (*i.e.* no reorientation) on the simulation timescale of $\sim 10^{-11}$s. From the difference between the initial value of P_2 and its plateau value, we can calculate a mean amplitude for this librational motion, for which we obtain a value of 9° at T/T_{trans} of 0.55. This amplitude increases slowly with increasing temperature but the plateau is maintained up to $T/T_{trans} \sim 0.8$ at which the librational amplitude is 11°. At higher temperatures, the plateau begins to relax, indicating a non-trivial reorientation of the octahedra on the simulation timescale. At high temperatures (500 K or more above the phase transition) the orientational CFs decay to zero in approximately the same time interval as the MSDs reach their rotational plateau at any given temperature.

4.1.1 The Mechanism of Reorientation

More insight into the nature of the rotational motion can be obtained by following the angular trajectories of one of the initially axial Al-F bonds of an octahedron

throughout a simulation. Such trajectories are illustrated in Figure 4.3 at two temperatures, the figures showing the instantaneous values of Ω, the angle made between the c-axis and the *initially* axial Al-F bonds, for several octahedra. The parameter Ω characterizes the octahedral tilt in the same way as θ but tracks the orientation of the initially axial bond when reorientation sets in. At the lowest temperatures, Ω simply executes small displacements from the average tilt angle. Above, but close to T_{trans}, we see the octahedra rapidly hopping from one preferred tilt orientation to another where they pause for a waiting time which reduces rapidly as the temperature is raised. Note that even at high temperatures, where the octahedra are reorienting quite rapidly (as judged by the decay of the orientational correlation function) and where the *average* tilt angle is zero, the octahedra prefer to occupy sites in which their tilts are close to those of the perfect *low temperature* crystal, the only exceptions being during the almost instantaneous flips between these preferred orientations.

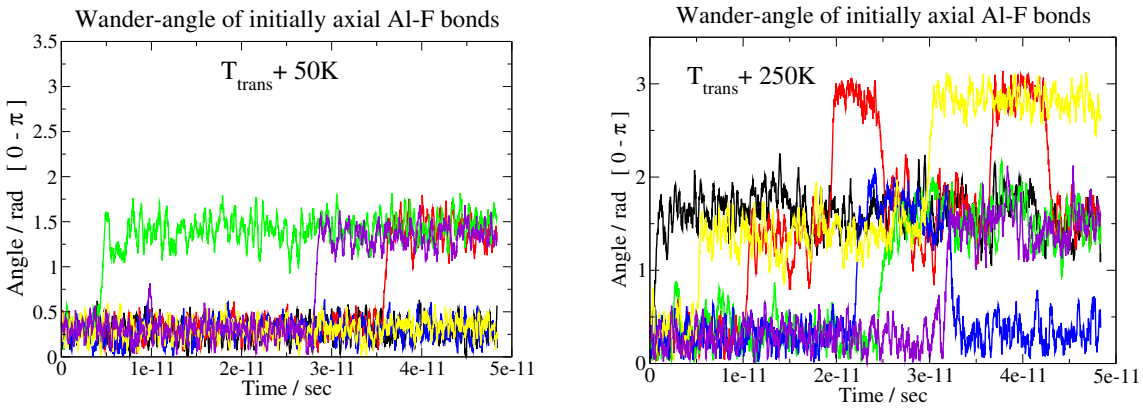

Figure 4.3: The angular path walked by a representative selection of AlF_6 in cryolite at two temperatures to show that, even well above T_{trans} their rotational motion occurs in swift flips between crystallographic fluorine sites rather than in a gradual diffusive motion. These plots were in fact taken from simulations using the empirical potential to illustrate the motion, though the behaviour under the fitted potential is identical about T_{trans}.

It was possible to refine this picture further and determine the axis of the AlF_6 octahedron about which the rotational hop most commonly occurs: the C_2 dihedral axis (the bisector of an adjacent pair of Al-F bonds), C_3 and/or the C_4 (parallel to

a Al-F bond). We did this by taking the sum of the dot products of the normalised bond vectors in each octahedron at time t with themselves at time $t + \delta t$, where δt spans a hop. A C_2 rotation would give a value of -2, C_3 would give 0 and C_4 would give 2 - then taking a running total of each type of rotation occurring throughout simulations at various temperatures, normalised by the number of octahedra. We saw that the *only* axes about which rotation occured were the C_4, which can be rationalised as the type with the lowest energy by the number of Na-F bonds in the neighbouring NaF_6 octahdera which must be broken to allow such a rotation (all six must move in a C_3 or dihedral C_2, but only four for C_4). The asymmetric structure of the crystal below T_{trans} (approximately tetragonal) raised the question of whether there is a preference as to which C_4 axis, if any, the rotation occurs around. A spinning-top type of motion about the axial bonds seemed a reasonable possibility owing to the symmetry. However, we could discern no difference in the rate of rotation around the axial or equatorial bonds at any temperature studied.

4.1.2 Reorientation rates and qualitative comparison with experiment

From the number of C_4 rotations per octahedron in a range spanning just below to far above the phase transition we calculated rotational hopping rates, and from their temperature dependence we derived an Arrhenius-like activation energy E_A. Although no experimentally-derived E_As are available for comparison, our E_As provide a useful measure of the relative energetics of different types of motion. From a simulation with 75 unit cells (1500 ions) we obtained 31 kJ mol^{-1}; similar values were obtained with the empirical potentials. To confirm the accuracy of these values of the activation energy we tried a second method which uses the temperature dependence of the correlation times derived from orientational CFs: these gave virtually identical values.

We saw only a small number of octahedral reorientational hops, resulting in changes of the Ω angle, below T_{trans} which is apparently at variance with the NMR

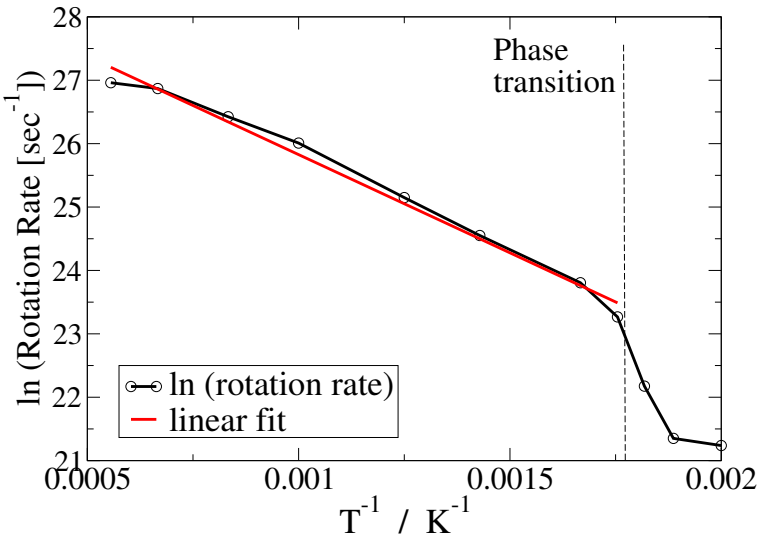

Figure 4.4: An Arrhenius plot of the natural log of the reorientational hopping rate (per AlF_6 unit) versus inverse temperature. The abrupt change of slope occurs at T_{trans}.

observations where narrowing of the dipolar and quadrupolar coupling is observed well below the phase transition. However, we believe that this apparent discrepancy is attributable to the difference between the simulation and NMR timescales. As we have indicated, and as experiment shows, the phase transition is very weak and there is no structural reorganisation at the transition which would disallow the kind of reorientational hop we have illustrated below T_{trans}. We simply see very few of them because our timescale is too short. An Arrhenius plot (figure 4.4) of the hopping rate shows a break of slope in the vicinity of the transition, but confirms that such hops do continue below T_{trans}, albeit relatively infrequently. The experimental data for the electrical conductivity [58] shows a similar step, with the conductivity continuing to decrease with decreasing temperature with approximately the same activation energy below the transition as above. If we imagine that this is also true of the reorientational hops we can extrapolate to estimate the rate of hopping in the temperature range of the experimental NMR spectra, using an Arrhenius Equation with the same activation energy as measured above the transition, *i.e.* 31 kJ mol^{-1}. On this basis, the hopping rate extrapolated to $T_{trans}/2$, corresponding

to about 440 K for the real material, is 0.25 MHz, which is consistent with complete motional averaging of the dipolar and quadrupolar coupling at this temperature. Although the reorientational motion below the transition is very slow on the MD timescale, this extrapolated rate is if anything too large to be consistent with the NMR observations.

The evolution of the reorientational dynamics across T_{trans} we have described seems to be consistent with the X-ray diffraction data, which has been interpreted to indicate a large increase in AlF_6 oscillation rate, the dynamic averaging of the two tilt-domain orientations and the collapse of cell lengths to those of a cubic crystal, when moving through the phase transition [52]. Seeing that reorientation occurs by discrete hops between the low temperature tilted sites, even above T_{trans} offers a way of reconciling the apparently inconsistent pictures which emerge from diffraction and NMR studies. The X-ray study reveals a high temperature structure wherein the AlF_6 are in well defined orientations with respect to the the cell axes, and the F^- thermal ellipsoids are quite small [48, 51, 52], similar in extent to those below the transition. However, NMR studies of the dipolar coupling between ^{27}Al and ^{19}F suggest full reorientation is occurring on the NMR timescale even in the low-temperature structure well below the transition [11] and suggest that reorientation would be very rapid by the temperature at which the transition occurs is reached. We observe the octahedra to adopt a narrow range of orientations with respect to the cell axes for the vast majority of time, which is consistent with the narrow thermal ellipsoids, even when rotation is rapid on the MD timescale, due to the almost instantaneous nature of the reorientational hops and the way they simply exchange the F^- ions between crystallographic sites.

4.1.3 Tilt-swapping

Although the 90°, Ω-changing rotational hops occur only infrequently on the MD timescale in the low temperature phase, investigation of the low amplitude motions indicated in the F^-'s MSDs (introduced in Section 2.4.2) revealed another more

subtle motion which results in a partial reorientation. On plotting the distribution of ϕ as shown in Figure 3.16 at a point just *below* T_{trans}, the clear division into two domains is lost. Both sets of octahedra, initially associated with the two tilt domains, produce the same twin peaked distribution of ϕ, symmetrical about 0° with maxima at the original low temperature values of ϕ, showing that at this temperature both groups sampled the same set of tilts. We then plotted how the mean angle ϕ of each group changed through time, and rather than seeing a fluctuation around zero, which would indicate the randomisation of distribution of octahedra between the two tilt orientations, we saw each group of octahedra simultaneously switch into the opposite tilt orientation in synchrony with the other group. This is shown in Figure 4.5. This occurred up to seven times during a simulation at temperatures where less than one reorientational hop of Ω per octahedron was occurring on the simulation timescale. This "tilt-swapping" motion results in a precession of the axial bond of an octahedron about the *c*-axis, as the octahedra switch between the two orientations shown in Figure 3.10, such that individual Al-F bonds are reoriented through twice the tilt angle $\sim 35°$. Notice that the tilt-swapping motion does not require the breaking of Na-F bonds, unlike the reorientational motion, it merely requires a collective large-amplitude libration.

The relevance of this tilt-swapping motion to experimental studies may be questioned. On energetic grounds it does not seem likely that such a synchronised motion could occur throughout a bulk crystal, as opposed to a periodically replicated simulation cell containing 150 AlF_6 octahedral units. It would seem more plausible if a crystal broke up into smaller domains across which the phase of the tilt was well defined. However, since with both the empirical and fitted potentials and in all simulation cell sizes, we saw this process occurring, it does seem to be a robust feature of the simulation dynamics. The discussion of the diffraction structure in the vicinity of the phase transition contains some suggestions of a motion of this type [48], and the heat capacity of cryolite begins to increase anomalously above the lat-

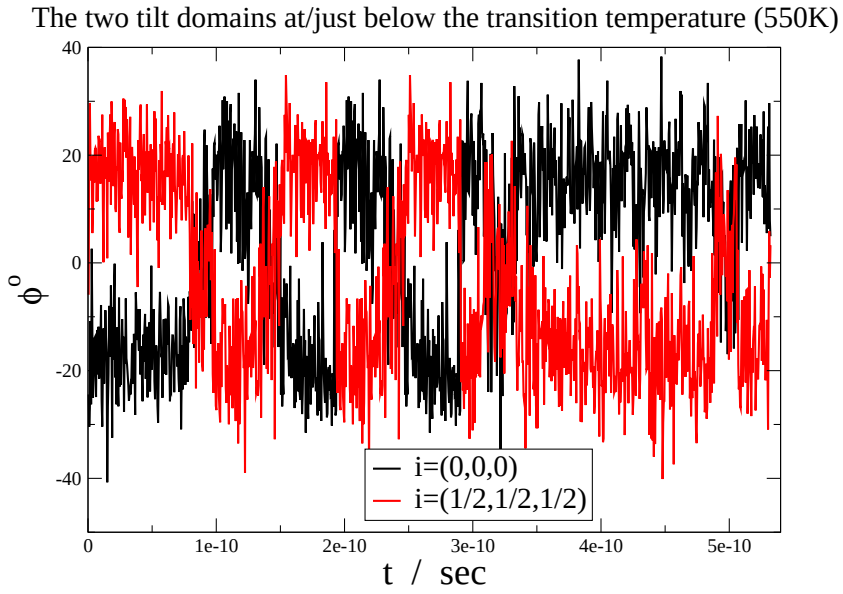

Figure 4.5: Showing the mean angle ϕ of each tilt domain under the fitted potential at the point we identify the transition to begin, 550 K. The value of i indicates the position of the AlF_6 units belonging to each domain within the unit cell.

tice value some 50 K below the transition temperature, indicating the onset of some type of motion not seen at low temperatures. Since the tilt-swapping motion simply swaps F^- ions between the normal crystallographic sites, it is not inconsistent with the diffraction observations of a well-ordered structure and small thermal ellipsoids (figure 4.6). If tilt-swapping does occur the bond reorientation would affect the NMR dipolar coupling or the quadrupole coupling like a large amplitude libration; Kotecha *et al* [11] reported a large angle librational motion from their analysis of their NMR data (figure 4.7), but whether this can really be ascribed to tilt-swapping or to a consequence of the nature of the reorientational hopping dynamics requires further work for clarification.

As the temperature is raised above through the transition and the rate of rotational hops of Ω becomes comparable to the tilt swapping, the octahedral tilts *do* randomise between the two orientations as the mean angle ϕ within each group fluctuates around zero. The distributions in this regime are displayed in the third panel of Figure 3.16, and show that the majority of AlF_6 lie at and in between the angles $\pm\phi$ seen in the low temperature structure. This indicates that there is

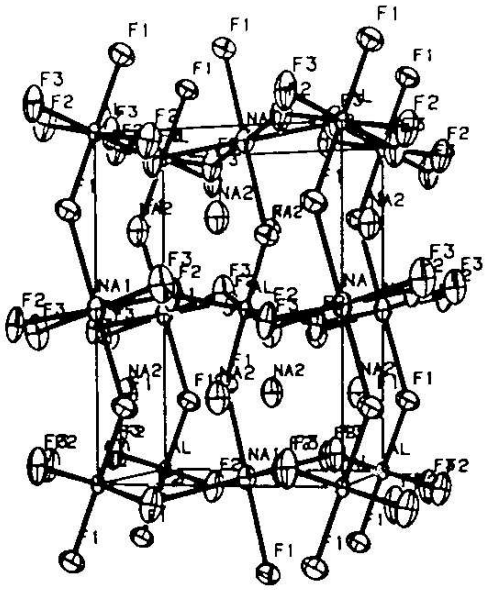

Figure 4.6: Thermal ellipsoids of the F^- ions in the cryolite lattice at 298 K, reflecting 95% probability volume occupation, from [48].

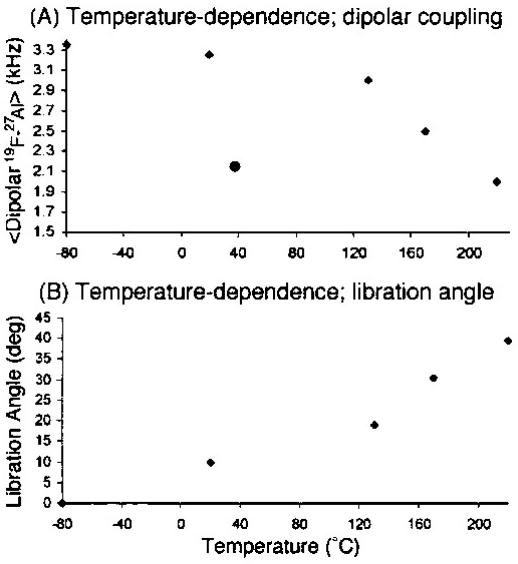

Figure 4.7: Al-F dipolar coupling and the AlF_6 libration angles derived thereby, as a function of temperature, from [11].

still an orientational preference but that there is no correlation between that of one octahedron and its neighbours. To confirm this we calculated the radial distribution functions (RDF) of AlF_6 octahedra lying in 'like' and 'unlike' tilt orientations (as illustrated by the blue and red octahedra in Figure 3.9) with respect to a central octahedron, over a range of temperatures. These are shown at temperatures above and below the fitted potential's phase transition in Figure 4.8. As expected, we saw an excess of *oppositely* tilted AlF_6 units at distances within the first minimum in the RDF of the low temperature structure, which decreased marginally through the synchronised tilt-swapping region, then became zero above the phase transition.

4.2 Defective Cryolite and Sodium Diffusion

NMR studies indicate a significant amount of Na^+ diffusion and exchange between the Na(6) and Na(8) (*i.e.* between the Na^+ ions on the A- and B′-sites shown in Figure 3.9) even at temperatures as low as 200°C[12, 57, 11] (which corresponds to $T/T_{trans} \sim 0.55$). The electrical conductivity [58] due to ionic motion is also found

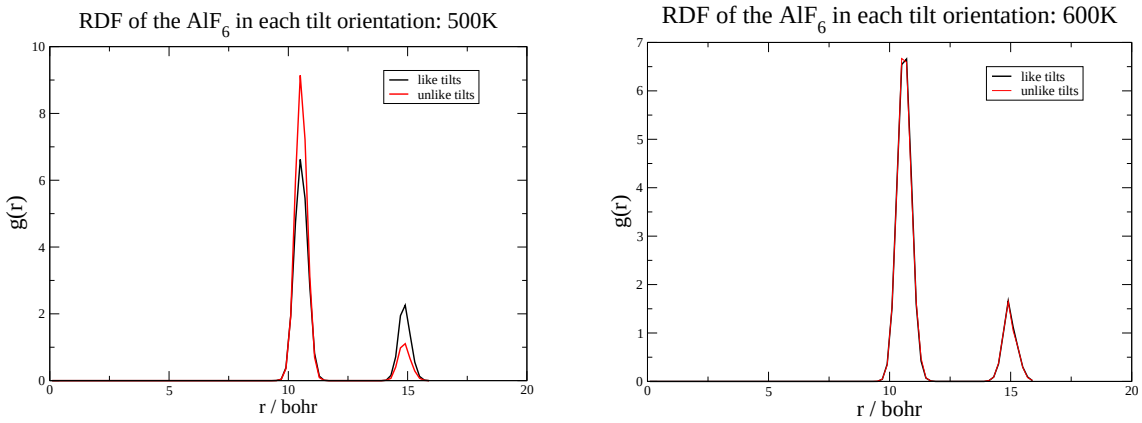

Figure 4.8: Radial distribution functions corresponding to like and unlike tilted octahedra in cryolite, indicating that the domain structure is intact at 500 K (approx. 50 K below the transition) and has been lost 50 K above.

to be appreciable down to these temperatures: it increases in an approximately Arrhenius manner with temperature, with a jump at the phase transition. By calculating the MSD of the Na^+ ions, we expected to see some diffusion occurring in the solid, especially above T_{trans} where the reorientational motion, believed to facilitate diffusion, is quite rapid. Diffusion would reveal itself through a linear increase in the sodium MSDs with time, but this did not occur except within 2-300 K of the melting point ($T/T_{trans} \sim 3.6$). We were able to calculate very rough estimates of an Arrhenius-like activation energy for sodium diffusion in this régime from the temperature dependence of the diffusion coefficients 'D', themselves calculated from the gradient of the MSDs, as shown in Equation 2.21. The E_As were of the order of 100's of kJ mol^{-1}, and far higher than the value of 43 kJ mol^{-1} derived from variable-temperature NMR experiments [12, 57, 11].

4.2.1 The Role of Defects

At first sight this failure to reproduce the experimental data, even qualitatively, would seem to indicate a catastrophic failure of the simulation. However, careful consideration of the phase diagram [69] (figure 4.9) indicates that *defects* are an inherent aspect of the structure of cryolite. The NaF-AlF_3 phase diagram [68] shows that at high temperatures stoichiometric cryolite (Na_3AlF_6) is unstable with respect

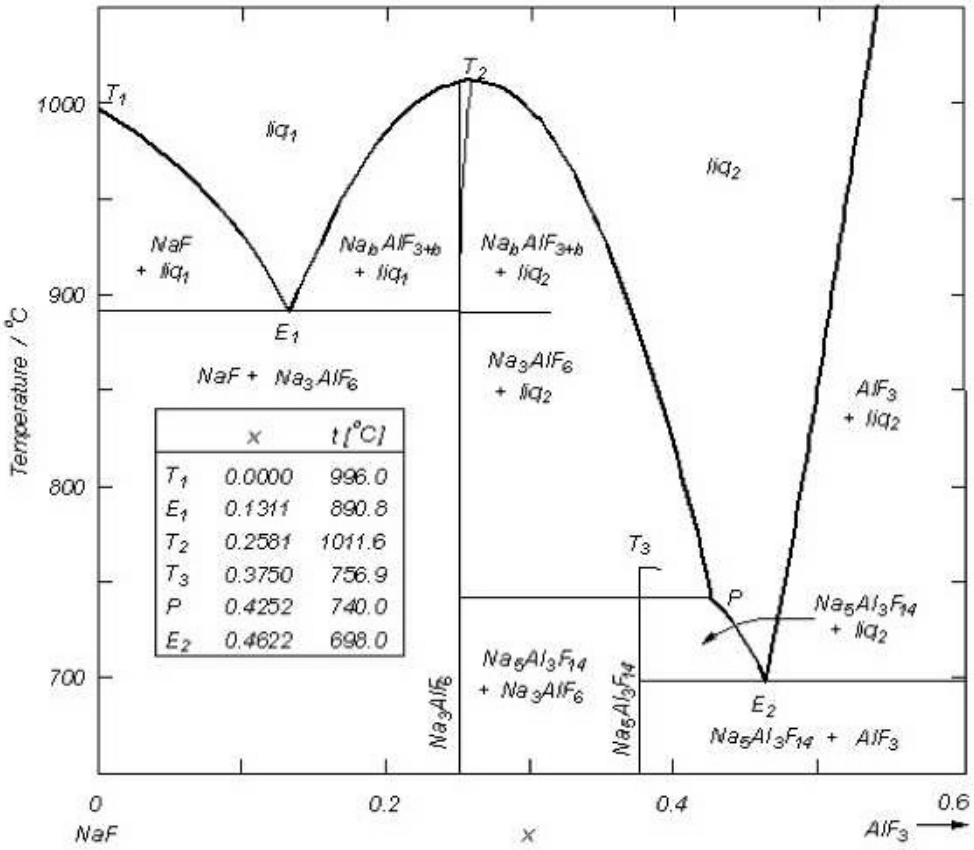

Figure 4.9: The phase diagram of cryolite, from [68], showing the defective nature of the solid at high temperatures.

to an Al-rich defective phase $Na_{3-x}AlF_{6-x}$ and NaF. This is indicated by the fact that the line representing stoichiometric cryolite touches the melting-curve at a point lower than a slightly Al-rich composition. Consequently a sample produced by thermal synthesis will have defects quenched in. We note that Kotecha *et al* [11] reported the presence of peaks due to pure NaF in their NMR study of a synthetic sample. Furthermore, depending on the temperature at which the synthesis is undertaken, different samples could contain different concentrations of defects quenched in, and this could account for the differences in NMR observations between different groups and different samples. Spearing *et al* [12] suggested that defects introduced in the synthesis could be the reason for the differences they observed between NMR relaxation times for natural and synthetic samples of cryolite, but the idea that even natural samples could be intrinsically non-stoichiometric does not seem to have been

considered previously.

Dewing [69] suggested an AlF_4^- entity for the coordination defect in a thermodynamic analysis of the phase diagram, but Kotecha *et al*[11] discounted the existence of 4-coordinate Al from the absence of peaks at the appropriate chemical shift in the NMR data. From the similarity between the crystal structures of cryolite and AlF_3 they proposed an alternative defect which involves only six-coordinate Al. This defect involves substituting an Al^{3+} ion into the position of a six-coordinate (B′-site) sodium and removing two eight-coordinate (A-site) sodium ions from the lattice. This introduces corner sharing between adjacent AlF_6 octahedra, giving a local structure which is the same as in pure AlF_3 and therefore expected to be of reasonably low energy. There will be some strain caused by the fact that the AlF_6 octahedron is smaller than the NaF_6 which it replaces. The defective structure is illustrated in Figure 4.10.

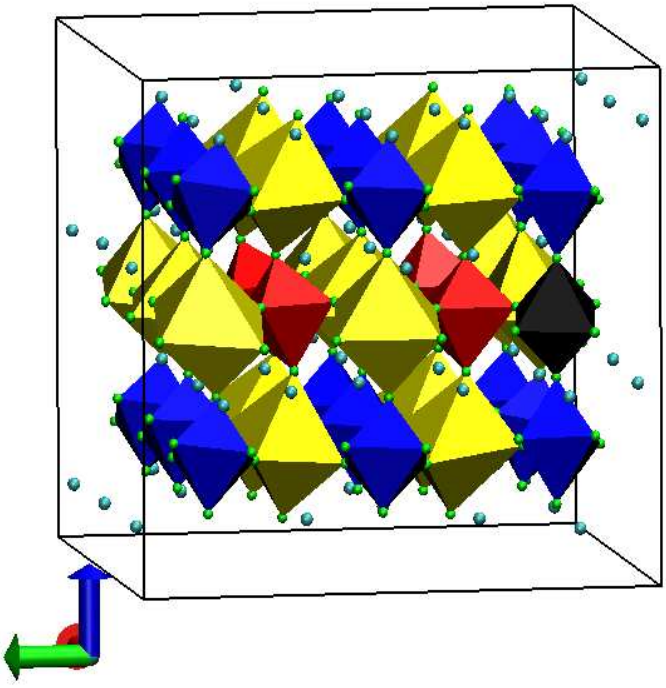

Figure 4.10: Illustrating the introduction of a defect to the structure of perfect cryolite by replacing a six-coordinate sodium with an aluminium (black octahedron), and removing two eight-coordinate sodiums.

This defect also introduces vacancies onto the A-site lattice and is likely to allow

diffusion to occur much more readily than the perfect crystal. The structure of cryolite is close to a cubic-close-packed (CCP) lattice of AlF_6 octahedra (regarded as spheres) with the $Na(6)^+$ (B′-site) ions occupying all of the octahedral holes (one per AlF_6) and the $Na(8)^+$ (A-site) ions all of the tetrahedral holes. This simplified description is depicted in Figure 4.11.

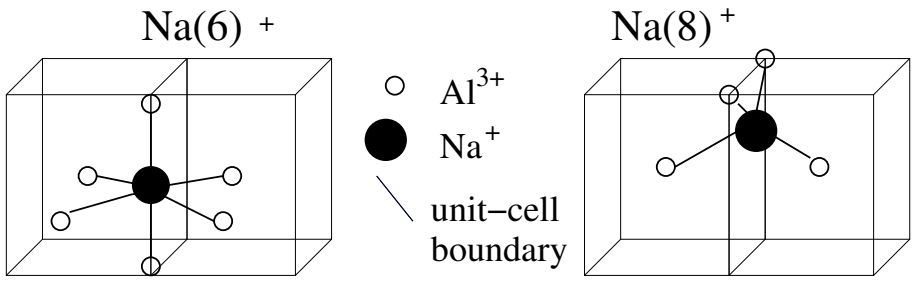

Figure 4.11: Showing the coordination of the Na^+ ions by Al^{3+}, in cryolite.

From this perspective there are no holes remaining in the perfect lattice to facilitate Na^+ diffusion and the "failure" of our simulation of the perfect crystal to give diffusion becomes more understandable. This CCP description of the crystal provides a useful model for understanding the structure *throughout* the solid phase. At all temperatures the $Na(6)^+$ (B′-site) ions are on average octahedrally coordinated by either 6 F^-s in the static structure or 6 rapidly rotating AlF_6 'spheres' in the dynamic structure, but the $Na(8)^+$ (A-site) ions experience a more variable environment: in the static structure they are best described as eight-coordinate, by two F^-s from each of the four surrounding AlF_6 units. The sizes of the sites may be characterised by the rattling amplitude of the Na^+ ions from the heights of the plateaus in the MSDs of the A-site and B′-site ions before diffusion sets in, which are shown in Figure 4.12.

At low temperature, the Na(8) appears to sit in a larger site than Na(6), but as the temperature is raised and the AlF_6 reorientation rate increases (rendering the AlF_6 more "spherical") the site-size becomes smaller than that of the Na(6). In this limit the A-site becomes better described as four-coordinate, by the four surrounding AlF_6 spheres, and the change in size is consistent with the properties of

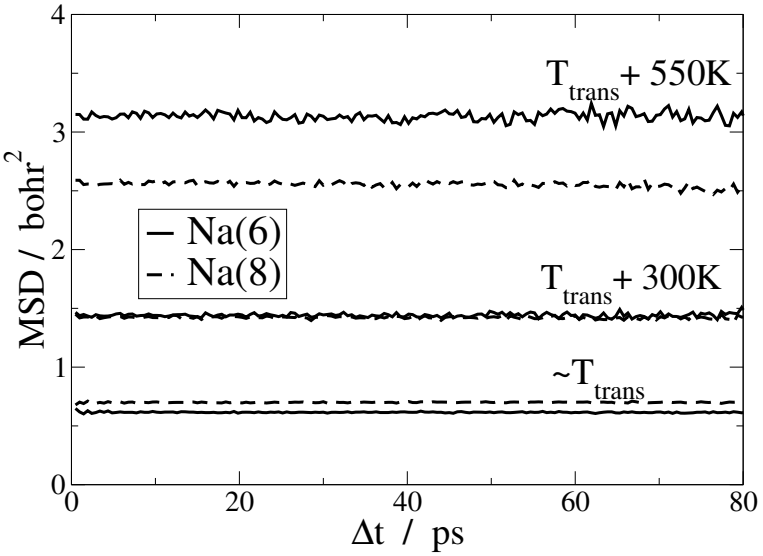

Figure 4.12: Showing the change in relative sizes of the sites occupied by Na^+ ions described as six- and eight-coordinate in the low temperature structure with increasing AlF_6 oscillation rate, as reflected by their rattling amplitudes.

a tetrahedral rather than an octahedral hole. The changing site size, as measured by the sodium ion rattling amplitude, is concurrent with the temperature dependence of the Na-F separations as studied by experiment, which showed that the Na(6)-F bond lengths decrease slightly, while the Na(8)-F bond lengths increase slightly with increasing temperature [70].

4.2.2 Defect formation energies.

We therefore examined the consequences of this type of defect for Na^+ diffusion in the simulations. By introducing one defect we could generate defect concentrations (or percentages of Na^+ ions removed) of $\frac{2}{3}\%$ and 3% in the 75 and 18 unit cell simulation cell sizes affordable to us. Dewing's phase diagram analysis suggest that both these would exceed the actual defect concentration in a well-prepared sample. The 3% defective system is shown in Figure 4.10.

To obtain a measure of the enthalpy required to form a defect at the two concentrations studied, we calculated an average energy difference between the two sides

of the Equation:

$$n(Na_3AlF_6)(s) + AlF_3(s) \longrightarrow (n+1)(Na_{\frac{3n-3}{n+1}}AlF_{\frac{6n}{n+1}})(s) + 3NaF(s) \qquad (4.2)$$

where all the materials are in their thermally equilibrated crystal structures at the same pressure and at temperatures of 100, 300 and 500 K where $(n+1)(Na_{\frac{3n-3}{n+1}}AlF_{\frac{6n}{n+1}})(s)$ indicates the defective simulation cell described above. In this work, $n = 36$ with a 3% defect concentration and $n = 150$ with $\frac{2}{3}$%. The values we calculated are presented in Table 4.1. We checked that the location of the Na(8) vacancies in the defective structure did not influence the calculation of the total energy of defect formation by comparing the results from several simulations with different initial vacancy locations (as we will see below, the Na^+ ions move fairly freely in these calculations so the average energy from an MD simulation represents a sample of a number of vacancy configurations). The differences were at least 1-2 orders of magnitude smaller than the values given in the table. The values in the table indicate that there is no large concentration dependence of the defect formation energy in the concentration range $\frac{2}{3}$-3% as both concentrations give values of approximately 350 kJ mol^{-1} in the range 100-500 K. The energy seems quite large but, since three species can be randomly placed on lattice sites for each defect formed, the entropy of formation will also be quite large and it does not seem unreasonable to expect that these defects could be formed at high temperature at concentrations which are consistent with Dewing's analysis. In fact, an enthalpy of 240 kJ mol^{-1} was reported by him [69] from an examination of the experimental phase diagram at very high temperature, and we would expect the formation energy to decrease in the more expanded lattice at the higher temperatures. We also calculated the formation energies of defective structures obtained by directly removing NaF from the cryolite structure, which create F^- as well as Na^+ vacancies. These energies were all higher than those of the defect illustrated in the figure.

Temp	3% [defects] / kJ mol^{-1}	$\frac{2}{3}$% [defects] / kJ mol^{-1}
100 K	+369	+358
300 K	+342	+423
500 K	+364	+343

Table 4.1: Energy cost of the formation of defects in cryolite at defect concentrations of 3% and $\frac{2}{3}$% / kJ mol^{-1}.

4.2.3 Influence of Defects on Na^+ Diffusion

The introduction of defects increased the rate of Na^+ diffusion very considerably. Examples of the MSDs of the Na^+ ions across the range of temperatures at which diffusion was observed with the fitted potential are shown in Figure 4.13. In addition to the MSDs we calculated site exchange correlation functions, where the exchange is defined only when a $Na(8)^+$ hops to a $Na(6)^+$ site or vice versa, this quantity should be directly related to the NMR exchange time. It is expected that diffusive hops would predominantly occur between these pairs of sites, as they are connected by the *faces* of the coordination polyhedra of the two sites, whereas pairs of Na(6) or Na(8) sites are connected only by vertices. Below the onset of diffusion the function remains at unity throughout the timespan of simulation. As the rate of diffusion increases, the function decays, eventually to zero in the limit of rapid exchange. From the $\frac{1}{e}$ times of each decay curve (figure 4.14), we calculated site lifetimes, and from their temperature dependence we derived an activation energy for site exchange at the two defect concentrations. These were 48 kJ mol^{-1} at the $\frac{2}{3}$% concentration and 30 kJ mol^{-1} at 3%, which reflect huge decreases from the non-defective simulations. Similar values for activation energies were obtained from the Na^+ diffusion coefficients. The value from the $\frac{2}{3}$% defective simulations, the concentration thought to be closest to that in real samples, is in good agreement with the experimental value of 43 kJ mol^{-1} [12]. Furthermore, extrapolating the Na^+ hopping rates from the $\frac{2}{3}$% concentration to the temperature range of the NMR experiments gives values of the same order of magnitude as those seen in the experiments [57, 11].

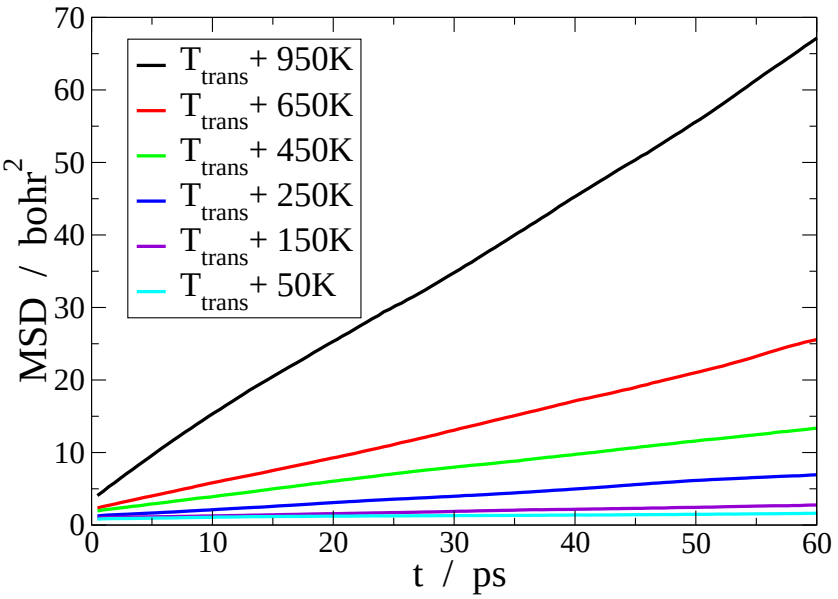

Figure 4.13: Showing the increasing rate of Na^+ diffusion with increasing temperature in defective cryolite.

The higher degree of diffusion in the defective structure is also more consistent with conductivity measurements [58], which are carried out in a temperature range where we are able to detect significant diffusion on the simulation timescale. The activation energy for the ionic conductivity extracted from the experimental data [58] near the phase transition is also about 45 kJ mol^{-1}: at higher temperatures, a higher activation energy is observed which could be due to an increasing contribution from thermally activated defects as the temperature is raised. We can estimate a conductivity value from the Na^+ diffusion coefficient using a Nernst-Einstein formula

$$\sigma = \frac{\rho q^2 D}{k_B T} \tag{4.3}$$

where ρ and q are the number density and charge of the Na^+ ions, and D is their diffusion coefficient. We obtain a value for D of 1.01×10^{-8} cm^{2}s^{-1} at 600 K, just above the transition temperature, for the large cell simulation with the $\frac{2}{3}$% concentration of Na^+ vacancies. This gives a conductivity of 7.2×10^{-4} Ω^{-1}cm^{-1}. The experimental value just above the transition is 3.2×10^{-4} Ω^{-1}cm^{-1}. Since the ionic mobility and conductivity will be proportional to the number of defects at low defect concentrations we can see that a sample with a smaller concentration of defects

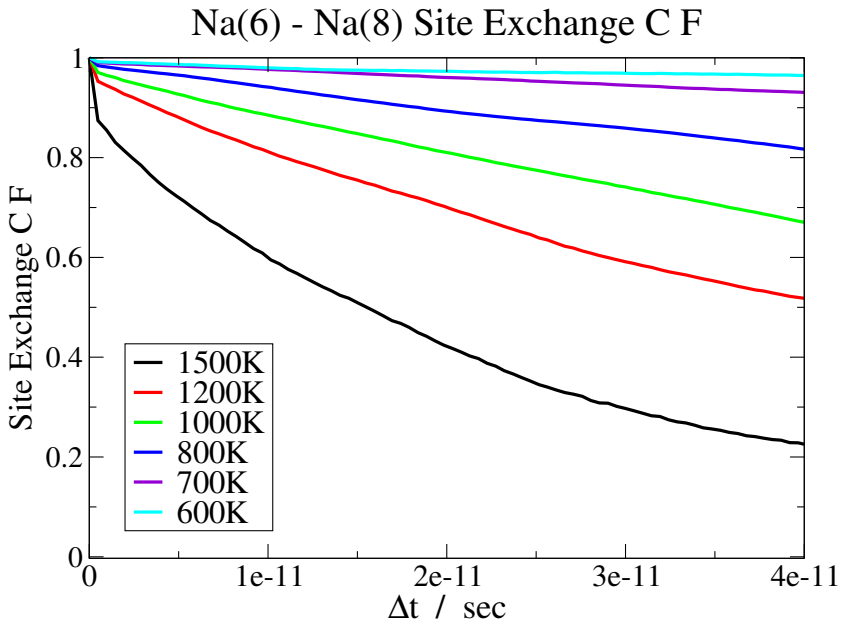

Figure 4.14: Showing the increasing rate of A-site to B'-site hopping with increasing temperature in defective cryolite. Here the colours are indexed by absolute temperature and correspond to the same scheme as the temperature with respect to T_{trans} in Figure 4.13.

than we have been able to accommodate in the simulations would give a similar conductivity to that reported in the Landon paper [58].

The decrease in the diffusion E_A on moving up from a $\frac{2}{3}$% to 3% defect concentration is very small compared to that of moving from 0% to $\frac{2}{3}$%, indicating that the introduction of only a very small number into a perfect sample, and variations in that number, would lead to a huge difference in the rate of Na^+ diffusion. This would cause large differences between experiments on different samples in conductivity measurements, and in the temperature of NMR Na(8)-Na(6) line coalescence, for example. To confirm that the E_As were accurate, we also calculated values from the temperature dependence of the MSDs: the E_As derived by either method were indistinguishable within our error, which supports our suggestion that diffusion occurs in a series of hops alternating between Na(6) and Na(8) pairs only.

We have verified that phase transition temperatures and the properties of the AlF_6 reorientational motion discussed in earlier sections are not significantly affected by the introduction of these defects.

4.2.4 Coupling between diffusion and AlF_6 rotation

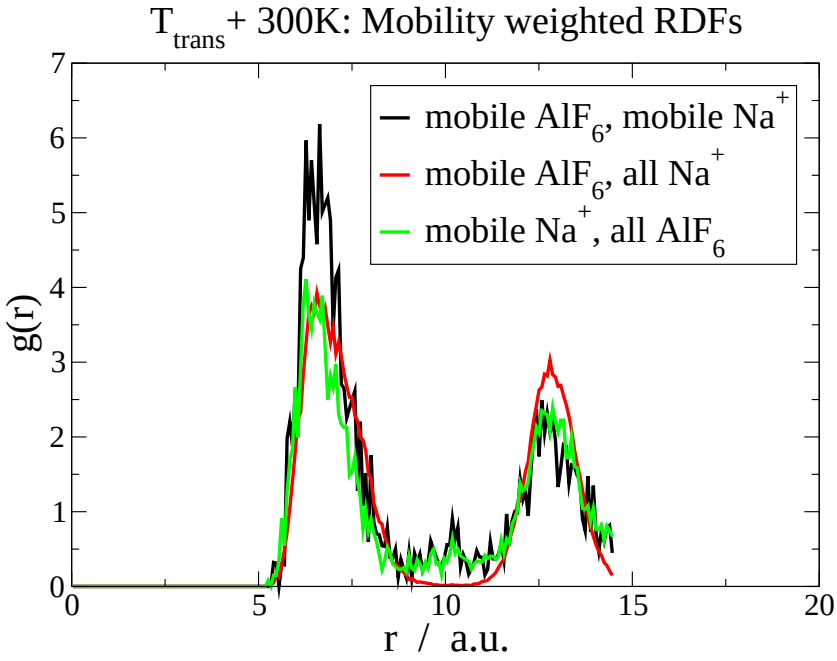

Figure 4.15: Showing the excess of mobile-mobile Na^+-AlF_6 pairs in cryolite at lower temperatures.

These findings support the first part of a proposition made by Spearing *et al*, on the basis of their NMR measurements [12]: "diffusion is by a vacancy mechanism, and the diffusion rate is controlled by oscillation of the AlF_6 octahedra". We attempted to investigate the second part of the statement by calculating mobility-weighted radial distribution functions (RDF) at each simulation temperature, in the hope that they would reveal a local mechanistic link between AlF_6 rotation and Na^+ diffusion. This quantity, similar to functions introduced by Gebremichael *et al* [71] to characterize motion in glasses, is obtained by dividing up the simulation trajectory into time windows of a certain length. Na^+ ions are "mobile" during the window if they translate by more than the distance between two Na^+ sites during this time interval. Similarly an AlF_6 unit is "rotationally mobile" if it undergoes at least one 90° hop in that time. The mobility weighted RDF gives the probability that a rotationally mobile AlF_6 unit is found at a distance r from a mobile Na^+ ion; it gives the spatial distribution of these subsets of ions. Comparison of this with

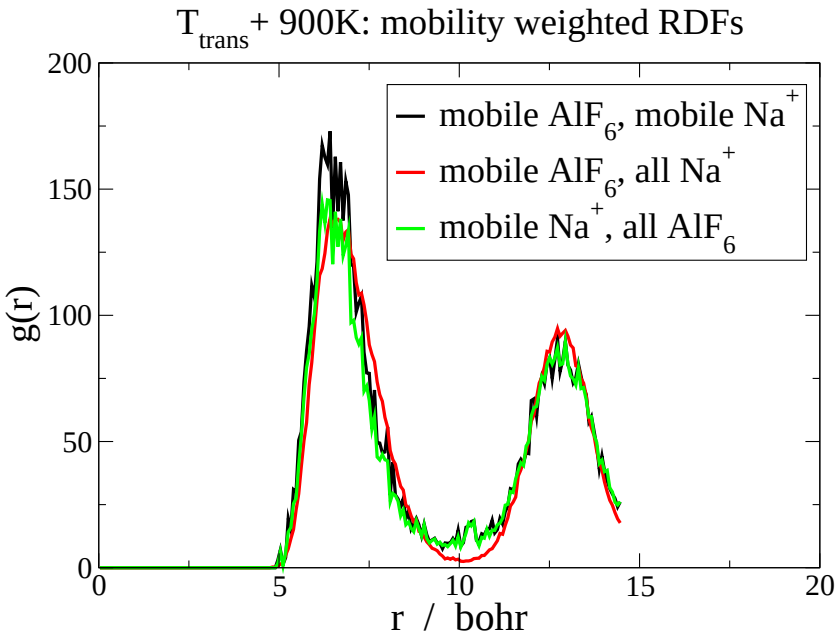

Figure 4.16: Showing how the excess of mobile-mobile Na^+-AlF_6 pairs in cryolite is lost as the temperature is increased even higher above the simulation phase transition.

the normal RDF in Figures 4.15 - 4.16 reveals an excess of mobile-mobile pairs at short separations, through the enhancement of the first peak. The effect is most pronounced at lower temperatures. This indicates that diffusion *is* promoted by the reorientation of an adjacent AlF_6 unit, but the correlation is not so strong as to suggest that reorientation is *necessary* for a diffusional jump to occur.

4.3 Summary of Cryolite Study

The *ab initio*-derived polarizable interaction potential appears to have reproduced the structure and dynamical properties of crystalline cryolite rather well. There is a significant discrepancy between the predicted and observed temperature for the transition to the high temperature cubic form, but the structures of the two phases are good. When the results for the dynamical behaviour are compared with experimental data on the reduced temperature scale T/T_{trans} there seems to be semi-quantitative consistency. There are several significant findings from our study for the interpretation of the experimental data on the ion dynamics. Firstly, a

model for the reorientational dynamics of the AlF_6 octahedral units emerges which consists of infrequent $\pi/2$ hops between the tilted positions of the low temperature crystal; this motion persists above the phase transition even though in this phase the crystal structure is cubic and the octahedra are, on average, aligned with the crystallographic axes. The extrapolated rate of this reorientational motion is at least qualitatively consistent with the NMR data. The model appears to reconcile the NMR observation of relatively rapid reorientation at low temperature with the diffraction observations of a well-defined crystal structure with fairly narrow thermal ellipsoids. In addition, we observe a "tilt-swapping" motion which is coherent and extends across the unit cell just below the phase transition and becomes incoherent above it. We observe no significant diffusion of the Na^+ ions *for the perfect crystal*, except close to melting.

However, noting that thermodynamic data shows cryolite to be intrinsically non-stoichiometric, we introduced a physically motivated postulate for the structure of a low energy defect and demonstrated that this greatly facilitated the diffusive motion. With a defect concentration of less than 1%, estimated conductivities were brought into agreement with experimental data, and the extrapolated rate of exchange of Na^+ ions between sites agreed with that obtained from NMR measurements. The introduction of defects in this concentration range does not appear to change the reorientational dynamics substantially. Finally, we have shown a way of confirming that the AlF_6 reorientation does facilitate Na^+ diffusion on neighbouring sites.

In future work, we will examine more sophisticated potential models in order to improve the transition temperature and to bring the experimental and simulation temperature scales into agreement. This will enable us to attempt quantitative comparisons with NMR data, at least in the fast motion régime, and with results emerging from quasielastic neutron scattering studies on the defective, high-temperature crystal.

Chapter 5

Developing Potentials for Molecular Ions

This chapter describes the development of the fitting process and our MD code to work with materials in which the bonding cannot all be described by an extended ionic model. The degree of success we expected in potential fitting for cryolite was fairly high, knowing that the bonding in the compound can be well-described by an extended ionic model: we had a certain degree of confidence that our potential model was sufficient to produce a 'good' correlation with the forces and dipoles from *ab initio* electronic structure calculations, based on the success of the previous work on oxides [14]. However compounds containing molecular ions were a new area, and their highly directional structures were another point of uncertainty, so there was little precedent for assuming we would be as successful at fitting potentials for these systems.

The systems studied are $Mg(OH)_2$ and $Cs_2UO_2Cl_4$, both chosen as compounds of significant scientific and technological interest, with simple molecular geometries (A-B and A-B-A) with which to start to develop a molecular ion model and the corresponding fitting techniques. Layered double hydroxides such as $Mg(OH)_2$ have a very wide intercalation chemistry [15, 40] as a result of the relatively weak interlayer bonding enabling the accommodation of ions and/or molecules [16, 17], making them of great technological interest through their absorption and anion exchange properties. Their uses include those as catalysts, catalyst supports [18], and they

are also involved in filtration, separation and membrane technology [19]. The uranyl ion is involved in both nuclear fuel processing and the extraction of uranium ore, and is discussed in chapter 7.

5.1 The Molecular Ion Model and Incorporating it into the Fitting Process: An Overview

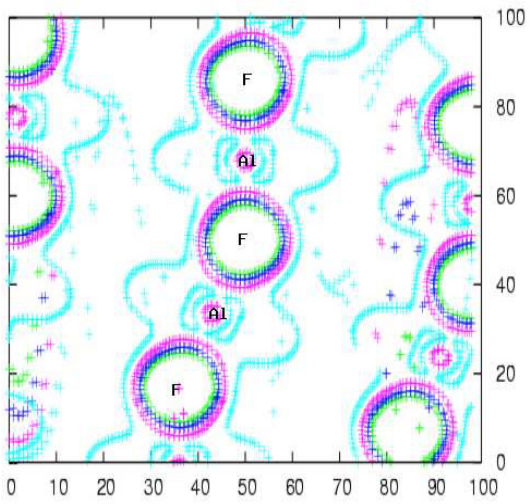

Figure 5.1: Two-dimensional slice of the electron density in AlF_3

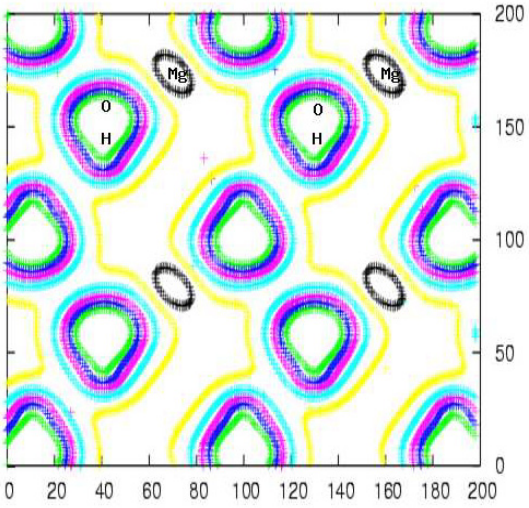

Figure 5.2: Two-dimensional slice of the electron density in $Mg(OH)_2$

From electronic structure calculations we can plot 2-dimensional slices of the electron density through planes of atoms in the crystals: in AlF_3 (and Na_3AlF_6) each atom appears discrete, even though the octahedra behave like molecular units. In $Mg(OH)_2$ the Mg^{2+} ions are discrete but the density is delocalised around the $(OH)^-$ molecular ions. This can be seen in Figures 5.1 and 5.2.

Firstly we had to decide how to model the molecular ions. We saw two potential methods, both of which employ a full atomistic model and treat the intermolecular interactions in the same way as the standard code (using Coulomb, short-range and dispersion interactions), but these terms are not included between atoms in the same molecule. In one, we introduce harmonic springs between bonded pairs of M-X in an 'MX_n'-type molecule to maintain the bond lengths, and another set between the X-X pairs to maintain the bond angles. The interaction energy between pairs is

then given by $E_{ij} = \frac{1}{2}k(r_{ij} - r_0)^2$, where r_0 is the equilibrium bond length.

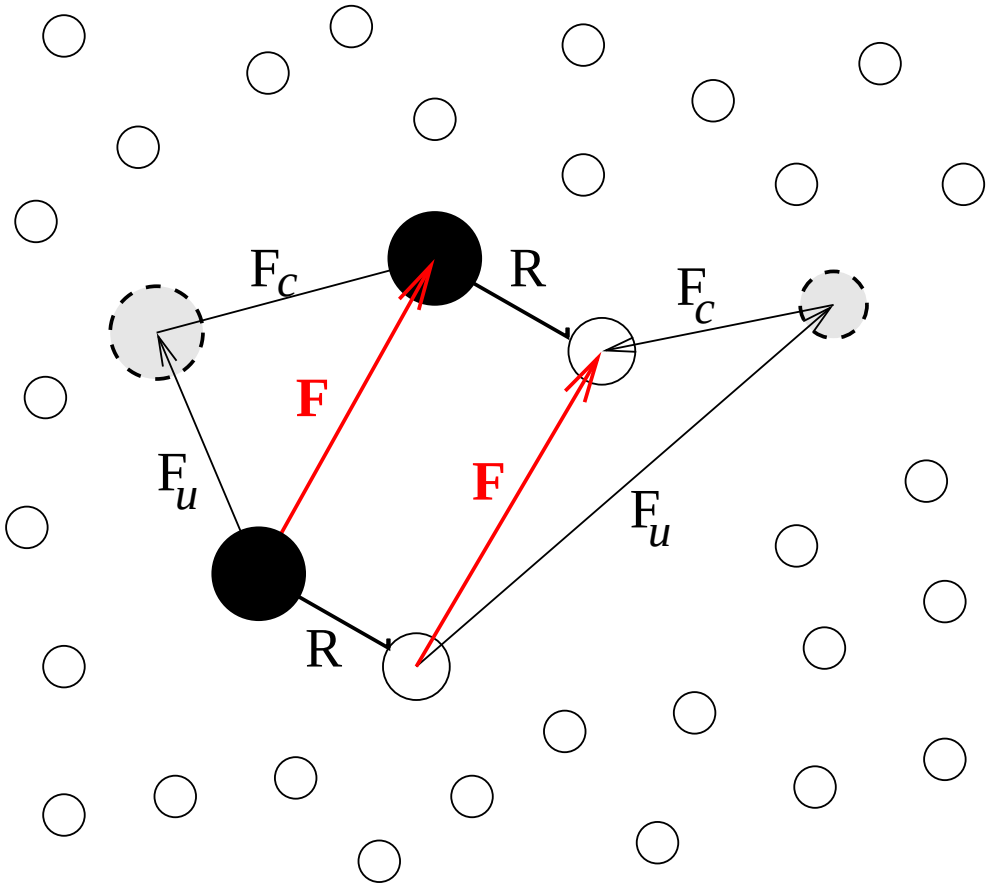

Figure 5.3: The forces involved in the constraint algorithm 'SHAKE'.

In the second method we replaced the springs with constraints which keep the molecules' bond lengths and angles fixed to their 'perfect' values. In order to enforce the constraints we encorporated the SHAKE algorithm [72] into our MD code. The steps involved in SHAKE are shown diagramatically in Figure 5.3, where $\mathbf{F}_u$, $\mathbf{F}_c$ and $\mathbf{F}$ are the unconstrained, constraint and resultant non-shape-changing forces respectively. SHAKE is a two-stage algorithm based on the Verlet integration scheme [24], to which we had to switch the MD code from the Velocity-Verlet scheme. In the first stage the Verlet algorithm calculates the motion of the atoms in the system assuming an absence of the rigid bond forces: the atoms move under force F_u. The positions of the atoms at the end of this stage do not conserve the distance constraint R required by the rigid bond, and a correction is necessary. In the second stage the

deviation in the length of a given rigid bond is used retrospectively to iteratively compute the constraint force F_c needed to conserve the bond length.

To be able to fit a potential with either model, we needed to make modifications to the existing fitting process. Beginning with the 'springs' model, we continued to fit the force on each ion, but needed to add an extra variable to the set that the fitting program has to refine values for - the force constant(s) k for each pair of species, reflecting the appropriate stiffness of the bonds. The other parameter introduced was r_0, the equilibrium bond length, which we chose to hold fixed at the crystallographic value.

With the constrained-geometry model, we needed to make significant changes to the fitting process, but there are several ways in which this method should be superior to both the regular fitting process and that where springs are incorporated. Firstly, though the harmonic springs are a reasonable approximation to use for the intramolecular forces in a classical model, we do not expect them to accurately mirror the form of the intramolecular forces from *ab initio* simulations, so it seems sensible to omit them if possible. This is both because their contribution to the forces is not likely to improve the fit quality, and because the addition of an extra variable to the fitting process further increases the complexity of the energy landscape which the fitting program is required to find the minimum of, where we suspected that in the case of the cryolite fits that fitting more variables in the more complex potential models resulted in it being less likely that the global minimum was found (for example, the final point on the AlF_3 line in Figure 3.7, representing the AIM-model with quadruploar polarization). Secondly, the workings of the constraint algorithm SHAKE involve iteratively modifying the forces on each atom within a molecule after the unconstrained forces have distorted the molecule's shape from one step to the next, until the ideal molecular geometry has been regained. By tapping into SHAKE at an appropriate point in each geometry iteration, we can accumulate the modifications to the forces to calculate the 'shape changing forces',

or the force on each atom in every molecule which would contribute to changing the molecular geometry at each timestep. By subtracting these from the total force on each ion, we obtain a set of 'non-shape-changing' forces which are completely **intermolecular** in origin. It is these purely intermolecular forces which we feed the fitting program to fit the potentials to. We believe this is the ideal set-up as it is the extended ionic model described for the cryolite work which the Madden group have been working with and honing for several years, and by excluding contributions from any covalent interactions we will still be using this model which we have seen can very accurately replicate the forces in and behaviour of simulations of various materials. Also, using constraints helps to simplify the fitting process: it both reduces the number of variables to be optimised, making it more likely that a global minimum is reached, and reduces the number of physical phenomena our potentials are required to replicate, where we know our extended ionic model is not adequate to describe the covalent bonding within molecular ions.

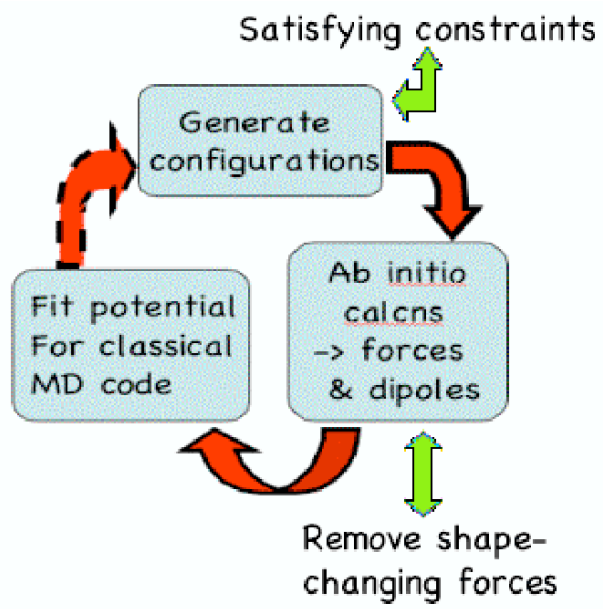

Figure 5.4: Modifications made to our fitting process in order to fit potentials for molecular ions, where the molecular geometry is held rigid using the SHAKE algorithm.

The way we modify our original fitting process is shown in Figure 5.4.

- The ions move independently under the potential created by the surrounding distorted crystal with force $\mathbf{F_U}$.
- SHAKE calculates the constraint force $\mathbf{F_C}$ required to keep the molecular geometry fixed.
- We tap into SHAKE at each iteration to calculate the non-shape-changing forces $\mathbf{F}$.
- The non-shape-changing forces must be purely intermolecular in origin, so it is these which we fit our potentials to.

We use an empirical potential to generate configurations which must now satisfy the molecular geometry constraints. As a first approximation in both methods we fix the equilibrium or constrained interseparations to values derived from crystallography. We then run single point *ab initio* calculations on them using CASTEP [41] to obtain forces and multipoles. The shape-changing forces are removed from the *ab initio* set, and we fit the non-shape-changing forces from our simulations to these by varying the parameters in the potential model.

5.2 Developing the Potential Model for Flexible Molecules

This section describes how we incorporated the 'springs' method into our MD program and the model we used. For the non-polarizable potential model the only part of the MD code which needed to be changed significantly was the short range energy routine, in order to replace the intramolecular Fumi-Tosi interactions with harmonic spring terms. We accumulate the energy U_{harm} by summing over the energies associated with each harmonic spring:

$$U_{harm} = \sum_{bonded\ pairs} k_{ij}(r_{ij} - r_0)^2 \tag{5.1}$$

where i and j represent the bonded atoms in a pair with separation r. The equilibrium separation is denoted r_0. Since the nature of the interaction between each

species combination is different, the value of the spring constant k changes if the respective species of i and j change. We then calculate the force on each ion in a bonded pair arising from the spring interaction:

$$F = -\frac{dU}{dr_{ij}} \qquad F_x = -\frac{\partial U}{\partial x_{ij}} = -\frac{dU}{dr_{ij}}\frac{\partial r_{ij}}{\partial x_{ij}} = -2k_{ij}(r_{ij} - r_0)\frac{x_{ij}}{r_{ij}}, \tag{5.2}$$

where x_{ij} is the x-component of separation r_{ij}, and F_x is the x-component of the force arising due from the interaction of j and i. The contribution of the spring interactions to the stress is omitted because for each molecule the total of the purely intramolecular forces is zero, where the stress is calculated by:

$$S_{ij}^{\alpha\beta} = \Sigma_{ij} F_\alpha d\beta \qquad e.g. S^{xy} = \Sigma_{ij} F_x dy \equiv \Sigma_{ij} F_y dx \tag{5.3}$$

and Σ_{ij} sums over all pairs i and j within the molecule. In addition to the spring interactions, short-range Fumi-Tosi and Coulomb interactions are included between atoms which are not in the same molecule.

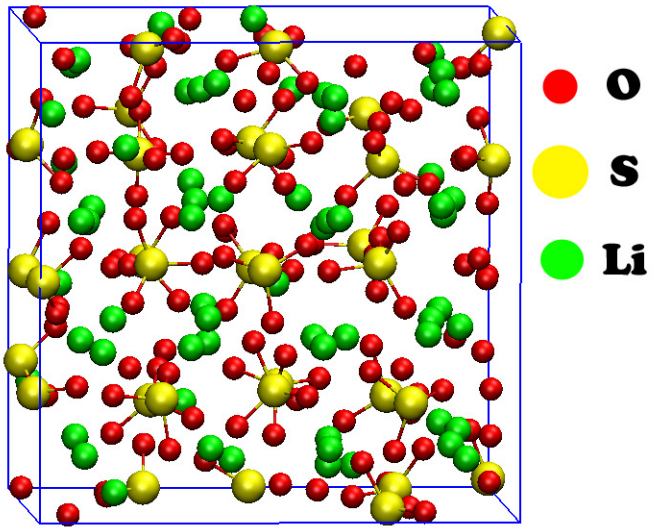

Figure 5.5: A snapshot from a test simulation of Li_2SO_4, view along the c-axis.

We ran our first tests of the modified MD program, experimenting with and without removing the contribution of the spring interactions to the stress. For these initial tests we ran simulations on an Li_2SO_4 system of 224 atoms (see Figure 5.5), as previous work on this compound [73] had produced an empirical potential we could

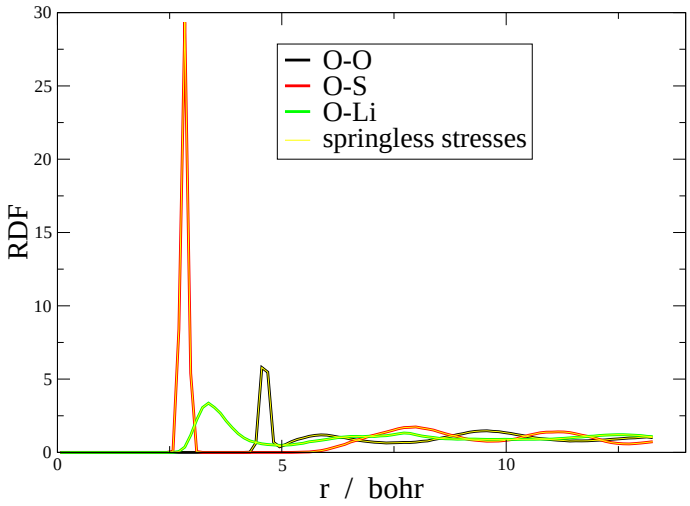

Figure 5.6: The RDFs of each species in Li_2SO_4, with and without the intramolecular springs contributing to the stress.

use, where the spring constants had been refined empirically to best reproduce the in-crystal molecular modes of the sulphate ion. (Where the properties of a molecule or ion in a crystal environment often differ from those in a gaseous environment). This potential required 2 sets of spring parameters k and r_0: one set between the directly bonded S and O atoms and the other between the terminal O atoms. The S-O spring constant k took a larger value of 0.1363 a.u. as this represents stretching vibrations which have a higher energy associated with them than the O-O bending vibrations (0.1132 a.u.). We found no difference in the behaviour of the system in the two simulations: the partial radial distribution functions of each species as calculated throughout the two runs are shown in Figure 5.6. These show that the yellow lines which represent the RDFs without the spring contribution perfectly overlay the lines representing the simulation where the springs did contribute to the stress.

For a triatomic molecular geometry (linear or bent) there needs to be an extra three-body interaction in order to keep the bond angle close to the appropriate equilibrium value. We chose a bending term in the form of Equation 5.4:

$$U_{bend} = U_0(1 - \cos^2\theta) \tag{5.4}$$

where U_0 is the equivalent of the stretching force constant k, and θ is the angle of deviation from the equilibrium bond angle. We calculate the value of $\cos A$ using the Cosine rule, as shown in Figure 5.7.

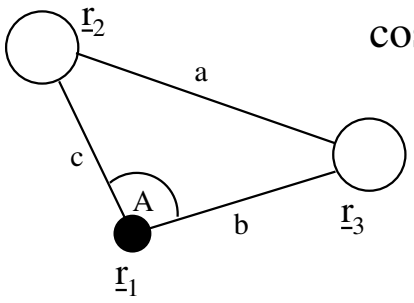

$$\cos A = \frac{b^2 + c^2 - a^2}{2bc}$$

Figure 5.7: To illustrate the calculation of the MX_2 bending energy.

The force on each atom in the molecule due to the bending interaction is a function of the position of all three atoms, and it can be written, for example using the x component of the force on atom 1 as:

$$F_{1x} = -\frac{\partial}{\partial x_1} U(r_{12} r_{13} r_{23}) = -\left(\frac{\partial r_{12}}{\partial x_1} \frac{\partial U}{\partial r_{12}} + \frac{\partial r_{13}}{\partial x_1} \frac{\partial U}{\partial r_{13}} \right) \tag{5.5}$$

where r_{12} denotes $r_2 - r_1$. We work through each derivative in turn as shown in Equations 5.6 and 5.7:

$$\frac{\partial r_{12}}{\partial x_1} = \frac{\partial}{\partial x_1} \left[(x_2 - x_1)\mathbf{i} + (y_2 - y_1)\mathbf{j} + (z_2 - z_1)\mathbf{k} \right] = \frac{\partial}{\partial x_1} \left(x_{12}^2 + y_{12}^2 + z_{12}^2 \right)^{\frac{1}{2}} = -\frac{x_{12}}{r_{12}} \tag{5.6}$$

$$\frac{\partial U}{\partial r_{12}} = \frac{\partial U}{\partial \cos\theta} \frac{\partial \cos\theta}{\partial r_{12}} = -2U_0 \cos\theta \left(\frac{1}{r_{13}} - \frac{r_{12}^2 + r_{13}^2 + r_{23}^2}{2 r_{13} r_{12}^2} \right) \tag{5.7}$$

Similarly:

$$\frac{\partial r_{13}}{\partial x_1} = -\frac{x_{13}}{r_{13}} \qquad \textit{and} \qquad \frac{\partial U}{\partial r_{13}} = -2U_0 \cos\theta \left(\frac{1}{r_{12}} - \frac{r_{12}^2 + r_{13}^2 + r_{23}^2}{2 r_{12} r_{13}^2} \right). \tag{5.8}$$

The resulting equations for the x component of the force on each atom due to the bending interaction are given in Equations 5.9 to 5.11.

$$F_{1x} = 2U_0 \cos\theta \left(\frac{x_{12}}{r_{12}} \left(\frac{\cos\theta}{r_{12}} - \frac{1}{r_{13}} \right) + \frac{x_{13}}{r_{13}} \left(\frac{\cos\theta}{r_{13}} - \frac{1}{r_{12}} \right) \right) \tag{5.9}$$

$$F_{2x} = 2U_0 \cos\theta \left(\frac{x_{12}}{r_{12}} \left(\frac{1}{r_{13}} - \frac{\cos\theta}{r_{12}} \right) + \frac{x_{23}}{r_{12} r_{13}} \right) \tag{5.10}$$

$$F_{3x} = 2U_0 \cos\theta \left(\frac{x_{13}}{r_{13}} \left(\frac{1}{r_{12}} - \frac{\cos\theta}{r_{13}} \right) + \frac{x_{23}}{r_{12} r_{13}} \right) \tag{5.11}$$

5.3 Testing the Molecular Ion Potential Model

To test the triatomic code we set up some simulations of $Cs_4U_2O_4Cl_8$, which has the monoclinic crystal structure shown in Figure 7.1. The space group is c2/m (unique axis b) and the cell lengths and angles are given in Table 5.1.

cell length a / bohr	22.5416
cell length b / bohr	14.5578
cell length c / bohr	10.9902
cell angles α, γ	90.0°
cell angle β	100.02°
r (U-O) / bohr	3.3637 ($= \frac{1}{2}$r(O-O))

Table 5.1: Cell lengths and angles of monoclinic $Cs_4U_2O_4Cl_8$.

First we set up a simulation using the standard atomic-ion code, which uses the full ionic charges on each atom (U^{6+}, O^{2-}, Cs^+ & Cl^-) such that the 'molecules' are held together only by Coulombic attraction. We would not expect a purely ionic description to represent this system well, but the test is useful for comparison with the molecular ion code. We constructed a 'large' simulation cell of 24 unit cells (stacked $a \times b \times c$: 2x3x4) which gave a repeating cell with dimensions of approximately 44 bohr^3. The cell contained 432 atoms, including 48 uranyl ions. We put together a test interaction potential by mixing empirically-tuned pair potentials which had been used in previous work on Cs-La-Cl-O mixtures[74]. The Cl^-, O^{2-} and Cs^+ parameters we took directly as the pair potentials developed for the code are roughly transferable between materials, and for U^{6+} we used the La^{3+} short-range potential parameters, as the higher charge on the 'uranium ion' leads it to contract closer to the size of the La^{3+}.

Secondly we set up a simulation of the same size using the newly developed molecular ion code. For this we used the same short-range potential parameters for the intermolecular interactions, but in addition needed values for the spring constants and equilibrium distances between the U-O and O-O pairs. The separations we obtained from a crystallography study [75] and are given in Table 5.1. The

fractional coordinates of the atoms within the unit cell are given in Table 5.2.

Atom	Multiplicity Wyckoff letter	x,y,z	fractional coordinates
Cs	4m	$x = 0.6653$ $z = 0.32254$	(x,0,z) (-x,0,-z) (x+$\frac{1}{2}$,$\frac{1}{2}$,z) (-x+$\frac{1}{2}$,$\frac{1}{2}$,-z)
U	2a		(0,0,0) ($\frac{1}{2}$,$\frac{1}{2}$,0)
O	4m	$x = 0.1162$ $z = 0.2362$	(x,0,z) (-x,0,-z) (x+$\frac{1}{2}$,$\frac{1}{2}$,z) (-x+$\frac{1}{2}$,$\frac{1}{2}$,-z)
Cl	8j	$x = 0.89895$ $y = 0.74870$ $z = 0.20570$	(x,y,z) (-x,y,-z) (-x,-y,-z) (x,-y,z) (x+$\frac{1}{2}$,y+$\frac{1}{2}$,z) (-x+$\frac{1}{2}$,y+$\frac{1}{2}$,z) (-x+$\frac{1}{2}$,-y+$\frac{1}{2}$,-z) (x+$\frac{1}{2}$,-y+$\frac{1}{2}$,z)

Table 5.2: Atomic fractional coordinates in $Cs_4U_2O_4Cl_8$.

We started with values for the spring constants k obtained by scaling down a value of k_{OH} taken from a Morse potential shown later in (table 5.5) used in a previous simulation study of $Mg(OH)_2$ [76], to reflect the weaker U-O bond energy. Using this as a starting value, we adjusted k_{UO} until we found values at which the system was stable in our simulations: 0.1363 Hartree/a_0^2 for U-O, 0.1032 Hartree/a_0^2 for O-O, and 0.1 Hartree/a_0^2 for the bending constant.

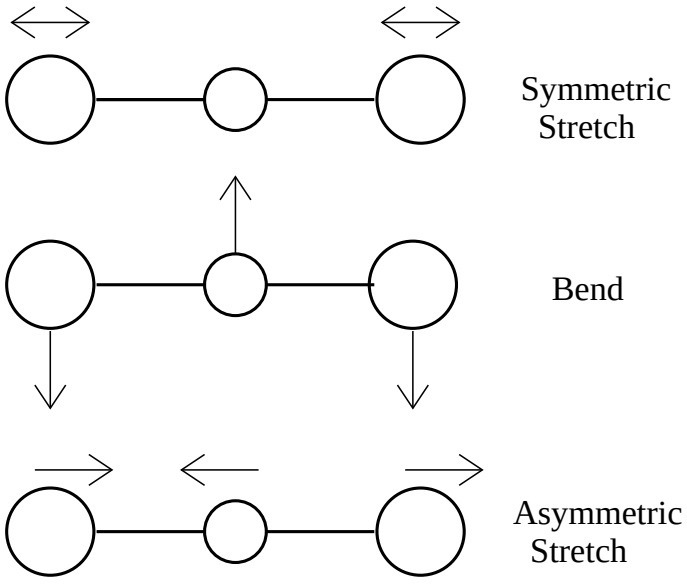

Figure 5.8: The three normal modes of vibration of a linear MX_2 molecule.

We went on to calculate the relative velocity correlation functions of the atoms within the molecular ions in the simulations with both the simple ionic model and

the molecular ion model with springs. We used simulations of 10,000 steps with a timestep of $2.4188\times10^{-16}s$ (10 atomic units), corresponding to a frequency well below the vibration frequencies of the UO_2^{2+} molecular ions. The 3N-5 normal modes of the linear molecule are the symmetric and anti-symmetric stretches and the bending mode, shown in Figure 5.8.

The quantities correlated at times t and $(t + \delta t)$ for each of the three functions are shown in Equations 5.12 to 5.14, where $\delta\mathbf{v}$ is the relative velocity of a pair and $\delta\hat{\mathbf{r}}$ is the unit vector separation of the pair. (Each of the x, y and z components for the bend are correlated separately then averaged over.)

$$V_{symm} = \delta\mathbf{v}_{U,O1}.\delta\hat{\mathbf{r}}_{U,O1} \quad + \quad \delta\mathbf{v}_{U,O2}.\delta\hat{\mathbf{r}}_{U,O2} \tag{5.12}$$

$$V_{asymm} = \delta\mathbf{v}_{U,O1}.\delta\hat{\mathbf{r}}_{U,O1} \quad - \quad \delta\mathbf{v}_{U,O2}.\delta\hat{\mathbf{r}}_{U,O2} \tag{5.13}$$

$$V^x_{bend} = \delta v_{UO1} - (\delta\mathbf{v}_{U,O1}.\delta\hat{\mathbf{r}}_{U,O1})\delta x_{U,O1} \quad + \quad \delta v_{U,O2} - (\delta\mathbf{v}_{U,O2}.\delta\hat{\mathbf{r}}_{U,O2})\delta x_{U,O2} \tag{5.14}$$

Then the correlation function is calculated as shown in Equation 5.15.

$$C(\Delta t) =< V_i(t_0)V_i(t_0 + \Delta t) > \tag{5.15}$$

Figures 5.9 - 5.10 show the velocity correlation functions for each interaction model. The set calculated from the simple ionic model can be seen to collapse as the correlation time increases, the bending mode being virtually non-existant, showing that there is little or no occurrence of distinct vibrational frequencies in the molecules using this description of the bonding. However, the set corresponding to the spring-model maintain a steady amplitude of the order of 10^{-5}, the two stretching vibrations being slightly better described than the bending mode which gradually loses amplitude over time. The bending mode is a weaker, lower energy vibration which would be more disrupted by introduction of a triatomic to a condensed, thermally distorted environment. The initial amplitude the two stretching vibrations from the ionic model simulation are an order of magnitude larger than those from the spring-bonded simulation: this would be due to the Coulomb and

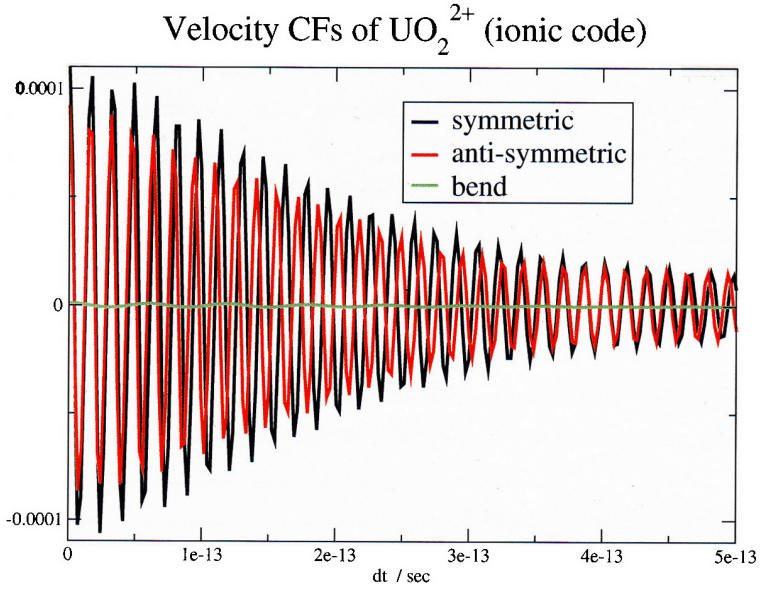

Figure 5.9: Velocity correlation functions corresponding to the normal modes of vibration of the UO_2^{2+} molecular ion, calculated from a simulation using a simple ionic model.

short range repulsive interactions being removed between atoms within the same molecule, reducing the forces from nearest neighbouring atoms, it could also be a result of the springs adding damping to the motion of the atoms under the Coulombic and short range forces from the surrounding non-covalently-bonded environment.

Figures 5.11 - 5.12 show the Fourier transformed velocity correlation (VCF) functions for each interaction model, a means of calculating the vibrational spectrum. The VCFs can be calculated in a similar way to the cage- and orientational-correlation functions, shown in Equations 2.25 and 2.28 respectively, where functions of the relative velocity of ion-pairs v_{ij} are the quantities correlated, themselves as a function of Δt. Each function of v_{ij} represents a vibrational mode. In the springs-simulation, all three vibrational modes have a distinct and relatively narrow range of resonance frequencies, indicating the basic behaviour of the molecules is well reproduced using this model. The results from the ionic-model simulation reveal that the bending mode is not reproduced at all with this model, and the two stretching modes fall at a high and very similar frequency, the two resonances having largely been picked up from the thermal motion of the ions.

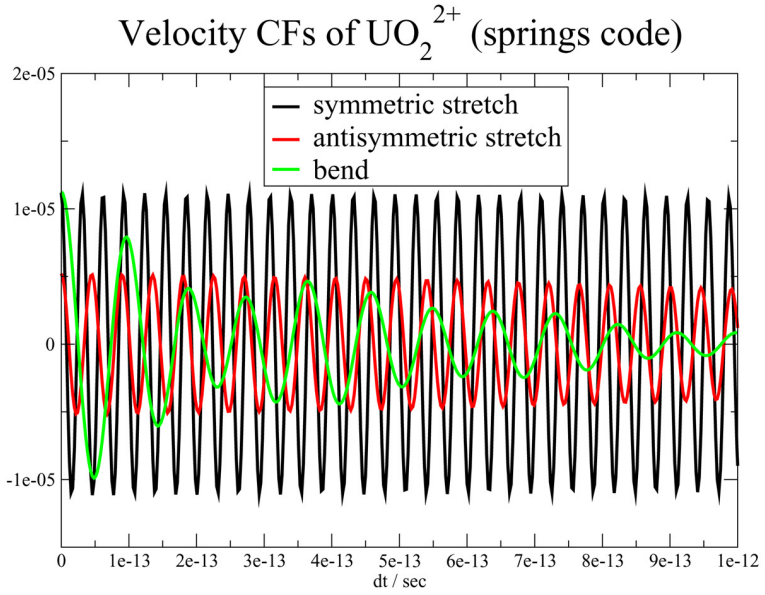

Figure 5.10: Velocity correlation functions corresponding to the normal modes of vibration of the UO_2^{2+} molecular ion, calculated from a simulation using springs to represent the intramolecular interactions.

source	exp'tal range	atomic ion model	molec. ion model
symm. stretch/cm^{-1}	860-880	2050	1075
asymm. stretch/cm^{-1}	930-960	2100	735
bend/cm^{-1}	199-210	indistinguishable	360

Table 5.3: The range of vibrational frequencies for each of the three modes of the uranyl ion from experimental studies [77], compared with those in our simulations of $Cs_4U_2O_4Cl_8$ under different potential models.

It has been established that the experimental frequencies of the uranyl ion over a wide variety of compounds lie in the ranges given in Table 5.3 [77], and these are compared with the frequencies from the two types of simulation. Firstly we see that the magnitude of the frequencies predicted by the molecular model are much closer to the experimental ones, the atomic ion model predicting frequencies in a much higher range. The symmetric and asymmetric stretches do not follow the correct sequence in the molecular ion model, however this is not a worry given how roughly we came up with values for the spring constants. Also, the bend and the symmetric stretch are on the high side while the asymmetric stretch is on the low side in this model, however the conclusion we can draw from this comparison as a whole is that

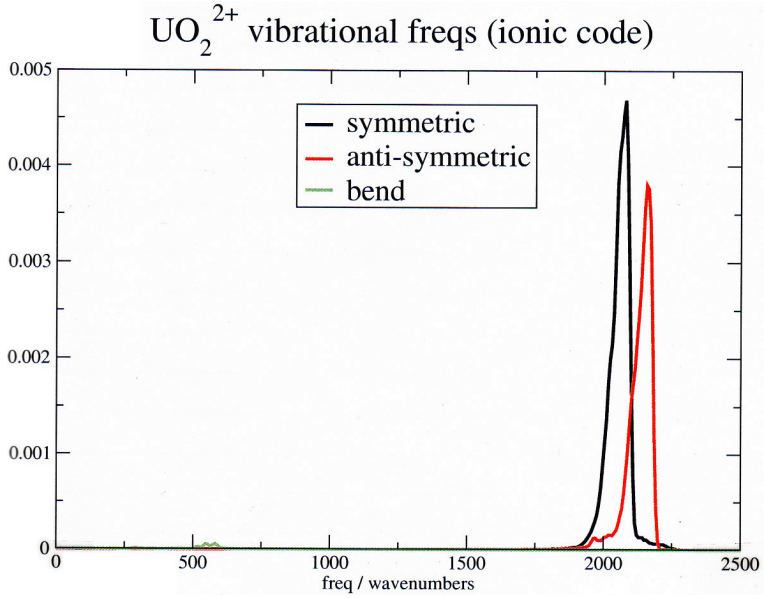

Figure 5.11: Vibrational modes of the UO_2^{2+} molecular ions, the Fourier transforms of the V.C.F.s in Figure 5.9.

the molecular ion model with springs is a huge improvement on the atomic ion model for this system containing ions within which the bonding is covalent.

5.4 First Attempts at Fitting Potentials Using A Flexible Molecular Model: $Mg(OH)_2$

The structure of $Mg(OH)_2$ of 'Brucite' has been determined by neutron diffraction [78]. The space group is P3m1; z=1 (group 164) with one formula unit per unit cell and the structure consisting of approximate $Mg(OH)_6$ octahedra. It is shown in Figure 5.13. The structure is layered along the *c*-axis with the O-H bonds directed vertically into the opposing layer, the layers being staggered as can be seen in Figure 5.13. The O-H bond-length is 0.95Å [78] and the positions of the ions within the unit cell are shown in Table 5.4.

In order to generate configurations for the purpose of *ab initio* single point calculations to obtain forces, dipoles, etc... we required an empirical potential to work with. Previous simulations [76] of H adsorption onto Fe_3O_4 have been performed using a Morse potential to describe the intramolecular O-H interaction. The form

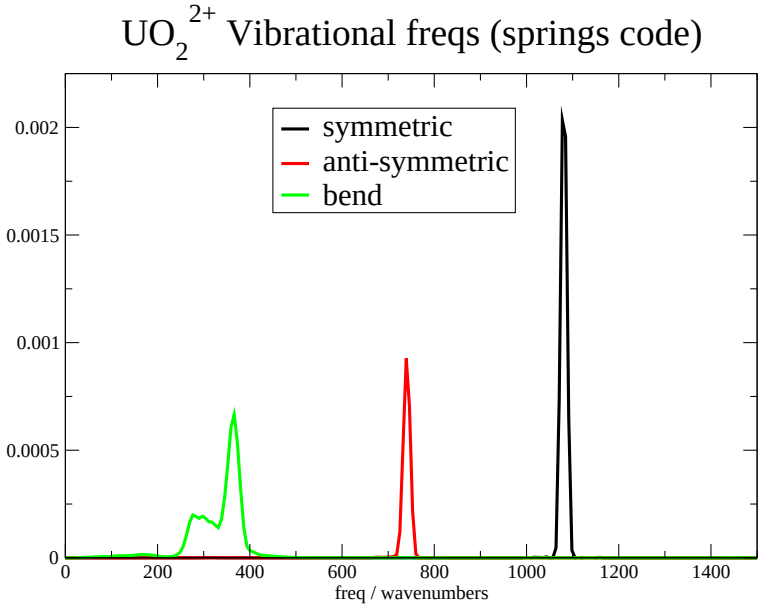

Figure 5.12: Vibrational modes of the UO_2^{2+} molecular ions, the Fourier transforms of the V.C.F.s in Figure 5.10.

ion	coordinates
Mg	(0,0,0)
O, H	($\frac{1}{3}$,$\frac{2}{3}$,z), ($\frac{2}{3}$,$\frac{1}{3}$,-z)

Table 5.4: Fractional coordinates of the atoms in $Mg(OH)_2$, where z_O=0.2203, z_H=0.4130.

of the Morse potential is given in eqn. 5.16:

$$U_{Morse} = D(1 - e^{-a(r_{ij}-r_0)})^2 \tag{5.16}$$

We can obtain an approximate harmonic spring potential ($U = k(r_{ij} - r_0)^2$) from a Morse potential, as shown in eqn 5.17:

$$U_{Morse} = D_{ij}(1-e^{-a_{ij}(r_{ij}-r_0)})^2 \approx D_{ij}(1-(1-a_{ij}(r_{ij}-r_0)))^2 = D_{ij}a^2(r_{ij}-r_0)^2 \tag{5.17}$$

Therefore $k_{ij} = D_{ij}a_{ij}^2$.

For the short-range interactions between atoms in different molecules, we used the Fumi-Tosi parameters from previous simulations of $MgCl_2$ [79] (shown in Table 5.6, all in atomic units). We omitted the O-H intermolecular short-range interactions, this being a reasonable thing to do as there is very little electron density

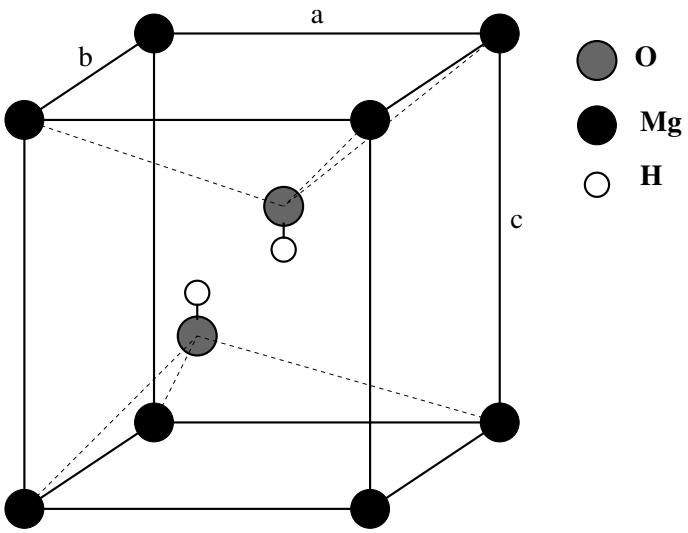

Figure 5.13: The structure of $Mg(OH)_2$.

parameter	value (orig. units)	value (our units)
D_{ij}	7.0525 eV	0.2588 hartree
a_{ij}	3.1749 $Å^{-1}$	1.6801 $bohr^{-1}$
k_{ij}	71.0891 eV/$Å^2$	0.7305 hartree/$bohr^2$
r_0	0.95 Å	1.795 bohr

Table 5.5: Morse and the corresponding harmonic spring parameters describing the O-H interactions.

surrounding the almost bare H nuclei. For the Coulomb interactions, we had to take into consideration the way that on each atom within a molecular ion the charges are not the standard full ionic charges, owing to delocalisation of the electron density around each molecule: we only know that the sum of the atomic charges is the full molecular charge of -1. The Morse potential from which we derived our spring potential used atomic charges of -1.4 on the oxygen and +0.4 on the hydrogen, so for consistency and in the hope of constructing a stable potential we used those values.

We set up some simulations over a range of temperatures of 4x4x3 unit cells, containing 240 ions, to test the stability of the potential and that a structure approximately like that determined in [78] was retained. This empirical potential only retained the structure at very low temperatures, after which the rather delicate layered structure collapsed into something resembling a liquid. As we require a rea-

ion pair	'B_{ij}' (a.u.)	'a_{ij}' (a.u.)	C_6	C_8	f_6	f_8
O O	100.0	1.53	222.3	7455.5	1.7	1.7
O Mg	125.0	1.8	30.0	300.0	1.56	1.05
Mg Mg	10.0	3.0	5.8	15.0	1.64	1.09

Table 5.6: Fumi-Tosi parameters used in empirical $Mg(OH)_2$ potential, derived from $MgCl_2$ potential. All values in atomic units.

sonable degree of distortion in the structure to gain a varied set of forces for the fitting program to work with, we thought it best to at least start by using liquid configurations to perform CASTEP single point calculations on. An empirical potential would be unlikely to reproduce a layered structure such as this accurately and we thought the best procedure would be to start introducing solid distorted crystal configurations at a later stage where the fits were iterated by generating new configurations with the first fit potential and feeding them back into CASTEP, repeating the process and refining the potential further.

So, for the purpose of generating configurations that CASTEP could work on we had to reduce the size of the simulation cell to something that would correspond to a computationally tractable number of electrons and an approximately cubic box. We chose a cell containing 36 $(OH)^-$ ions and 18 Mg^{2+} ions (3x3x2 unit cells). This summed up to 288 electrons, where one belonged to each hydrogen ($1s^1$), eight to each oxygen ($2s^2 2p^4$) and two to each magnesium ($3s^2$), the lower shells in the latter two being considered part of the core and not pseudized. We used norm-conserving pseudopotentials for each of the atoms, of which that for oxygen had previously been developed for ionic rather than covalent systems, but once again it seemed a good starting point and a more taylored set of pseudopotentials could be developed for use in further iterations of the fitting process.

In the first attempt at fitting $Mg(OH)_2$ potentials we used the crystallographically derived O-H bond length of 1.795 a_0, the partial charges of -1.4 and +0.4 on the O and H, and fixed the dispersion parameters from the empirical potential. As starting values for each of the parameters to be fit, we used the values from the

empirical potential, including the spring constant of 0.7305 hartree.a_0^{-2} derived from the Morse potential. The aim was to fit a simple non-polarizable potential at this stage in order to keep things simple and ensure the fundamental process was working as we expected. This meant there were a total of 13 parameters to fit; the Fumi-Tosi exponent and pre-exponential factors α_{ij} & B_{ij} for each of the six pair-combinations (Mg-Mg, Mg-O, etc...) and the O-H spring constant k_{OH}. We expected to obtain fairly poor force fits using this simple model, and this turned out to be the case as the result was a χ^2 of 4.361. Although poor, it was evident on comparing the sets of *ab initio* and fitted forces that they were the same configuration and followed the same trends fairly closely, confirming that our basic method was sound.

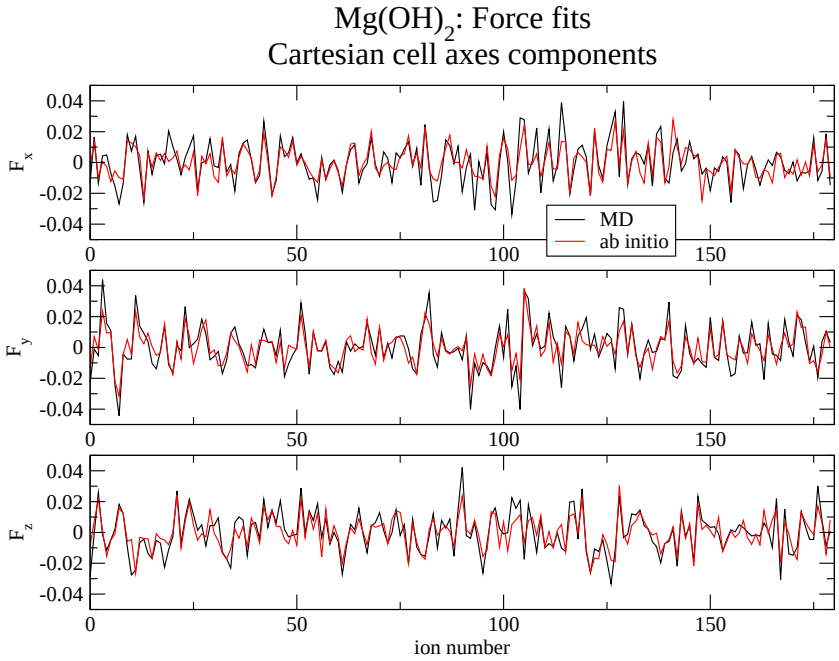

Figure 5.14: Comparison of *ab initio* and fitted forces (in atomic units) from the first attempts at fitting a $Mg(OH)_2$ potential with O-H spring-interactions, fitting both the spring constant k and the equilibrium bond length r_0.

In an attempt to improve the fit, we found the routine of changing the starting parameters had no real effect, though we tried changing them to the values from a very well tried and tested MgO potential [80] to optimize the starting position. Looking at the final values of the parameters from the first fit it could be seen that the O-O pre-exponential was pushing the upper boundary, which matches the

behaviour of the same parameter in the fitting process for the MgO potential. This is a particularly important, structure-defining parameter as the O-O interaction defines the layered structure of the $Mg(OH)_2$ crystal. However on raising the ceiling to allow B_{OO} to become unusually large, we saw no improvement in the fit quality and as in previous fits the other parameters (particularly α_{OO}) could be seen to shift to compensate for the increasing effective oxygen radius.

As an experiment to observe the effect on the fit quality, though it was not desirable as a 'final method' as we wish to replicate the structures accurately, we tried fitting the equilibrium bond length for the spring-loaded O-H bonds along with the parameters from the first fit. This turned out to improve the fit significantly, bringing χ^2 down to 0.845, and the bond length contracting from 1.795 to 1.764 a_0. The force components from the *ab initio* and fitted potentials are compared in Figure 5.14. The fitted 'MD' forces are a little larger on average but on the whole these were decent fits for a non-polarizable model and bode well for further work with this method. The shortening of the bond length suggests that perhaps there is some small discrepancy between the known crystallographic bond length and the effective equilibrium bond length in the CASTEP simulations. One possibility is that this was an issue with the specific pseudopotentials we used, though they had been tested enough before in work on different materials for us to know they were reasonable. However this was one of the factors which spurred us on to find a way to eliminate the intramolecular interaction from the fitting process, hence the major part of the work in this area being with the constraint-method which has this advantage.

Before properly formulating the constraint-method however, we foresaw another possible method which was to change the Cartesian frame of the forces on each atom in the diatomic molecules, resolving them *along* and *perpendicular to* the bonds. Were the problem to be the forces along the bonds, which seemed a likelihood as we would not expect the harmonic spring interaction to resemble the form of the

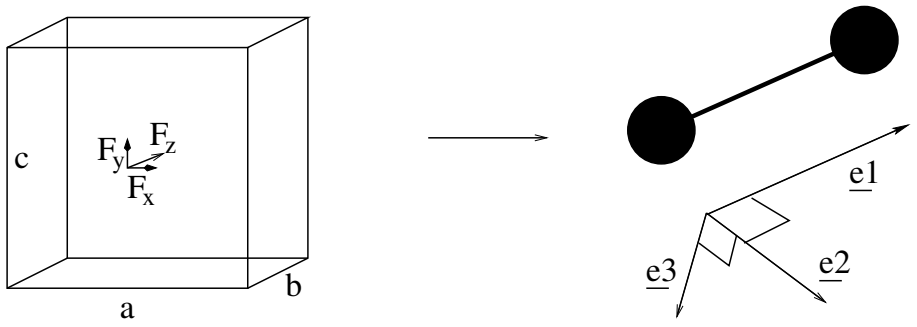

Figure 5.15: Transformation of the frame of the forces on the atoms in each OH^- molecular ion from partial alignment with the cell axes to the bond frame.

intramolecular potential from the *ab initio* calculations, we could then try fitting the forces perpendicular to the bonds to find values for the Fumi-Tosi parameters. These values could then be fixed in a subsequent fit of forces along the bond axes in order to find the optimum value for the spring constant k_{OH}. The transformation of the forces is shown in Figure 5.15, using Equations 5.18 to 5.20.

We first find the unit vector parallel to the bond $\hat{\mathbf{e}}_\mathbf{1}$, then any unit vector perpendicular to it $\hat{\mathbf{e}}_\mathbf{2}$ by taking the cross product with an arbitrary vector. The remaining Cartesian component $\hat{\mathbf{e}}_\mathbf{3}$ is found by taking the cross product of the other two. We multiply each of these by the original force $\mathbf{F}$ to calculate the components in the molecular frame.

$$\hat{\mathbf{e}}_\mathbf{1} = \frac{dx_{OH}}{|\mathbf{r}_{OH}|} + \frac{dy_{OH}}{|\mathbf{r}_{OH}|} + \frac{dz_{OH}}{|\mathbf{r}_{OH}|} \tag{5.18}$$

$$\hat{\mathbf{e}}_\mathbf{2} = \frac{\hat{\mathbf{e}}_\mathbf{1} \times (1,0,0)}{|\hat{\mathbf{e}}_\mathbf{1} \times (1,0,0)|} \quad ; \quad \hat{\mathbf{e}}_\mathbf{3} = \hat{\mathbf{e}}_\mathbf{1} \times \hat{\mathbf{e}}_\mathbf{2} \tag{5.19}$$

$$F_{parallel} = \hat{\mathbf{e}}_\mathbf{1}.\mathbf{F} \quad ; \quad F_{perp\ 1} = \hat{\mathbf{e}}_\mathbf{2}.\mathbf{F} \quad ; \quad F_{perp\ 2} = \hat{\mathbf{e}}_\mathbf{3}.\mathbf{F} \tag{5.20}$$

So, upon modifying the fitting program to fit the forces on the oxygens and hydrogens in the molecular frame, we ran a fit with same starting, step and boundary values as for the fit shown in Figure 5.14. The *ab initio* forces are shown alongside the fitted forces resulting from this fit in Figure 5.16. The resulting value of χ^2 for this was 1.028: similar if a little larger to the same forces fit in the original frame. We would not expect χ^2 to be identical for each because although the force vectors are the same, it is the individual components we fit so the data points are different.

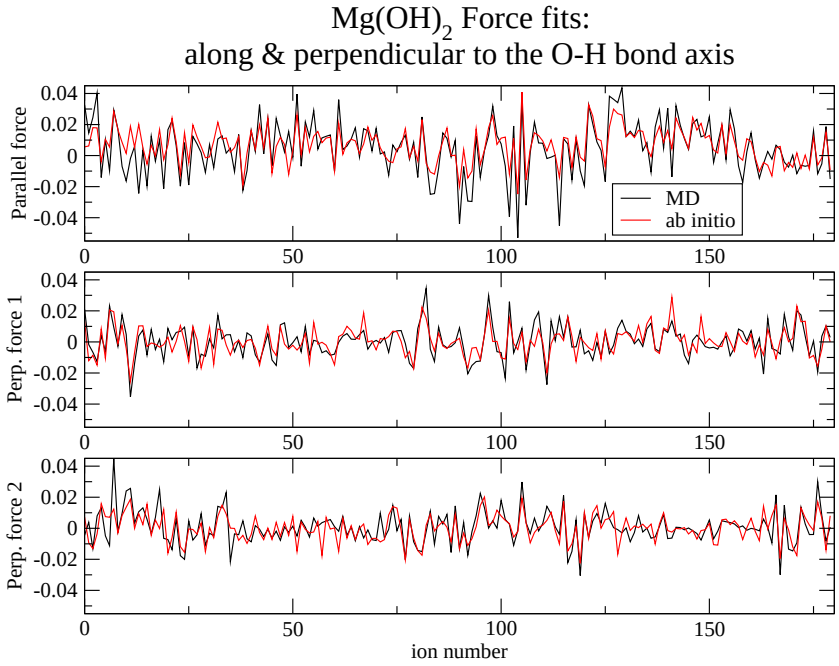

Figure 5.16: Comparison of *ab initio* and fitted forces (in atomic units) from the first attempts at fitting an $Mg(OH)_2$ potential: with O-H spring-interactions, fitting both the spring constant k and the equilibrium bond length r_0.

As suspected would happen, it can be seen in Figure 5.16 that the *ab initio* and fitted 'MD' forces do not coincide so well along the axes parallel to the bonds as along the perpendicular axes. In addition to the poorer fit quality of the parallel forces, the *ab initio* set also appear to have a finite positive average value, confirming that the equilibrium bond lengths we used are not the same as CASTEP would predict for these configurations. The fitting program has therefore attempted to replicate the positive forces along the bond axes, introducing quite a major unwanted artifact into the resulting potential, as well as further complicating the process. This discrepancy along with over-simplicity of the spring potential are what we went on to attempt to overcome using the constraints method, as further work fitting the individual components in the molecular frame did not prove useful.

5.5 Fitting Intermolecular Potentials Using Constraints: Developing the Basic Method

In order to constrain the molecular geometries we needed to incorporate the SHAKE algorithm into our MD program, as described in section 5.1. SHAKE requires use of the Verlet algorithm [24] (Eqn. 5.21) in which no velocities appear rather than the Velocity-Verlet which is that which our code uses to move the atoms from one timestep to the next, so this was the first change we made.

$$\mathbf{r}(t+\delta t) = 2\mathbf{r}(t) - \mathbf{r}(t-\delta t) + \delta t^2 \mathbf{a}(t) \tag{5.21}$$

A set of undetermined multipliers represent the magnitudes of the forces directed along the bonds, which are required to keep the bond lengths constant. For each timestep the Equations of motion are solved without considering constraints, then SHAKE finds the magnitude of the constraint forces and corrects the atomic positions.

For the case of the diatomic O-H, with equilibrium bond length d_{OH}, the non-shape-changing forces $\mathbf{F}$ are given by:

$$m_H \mathbf{a}_H = \mathbf{f}_H + \mathbf{g}_H = F_H \tag{5.22}$$

$$\mathbf{r}_{OH}^2(t) - \mathbf{d}_{OH}^2 = 0 \tag{5.23}$$

where f_H are the forces arising from the interaction potential and g_H are the constraint forces. Obeying the constraint in Equation 5.23 and choosing the hydrogen atom, the sequel to its Equation of motion becomes:

$$\mathbf{r}_H(t+\delta t) = \mathbf{r}'_H(t+\delta t) + \frac{(\delta t)^2}{m_H}\mathbf{g}_H(t) \tag{5.24}$$

where $r'_H(t+\delta t)$ is the unconstrained position of the hydrogen immediately after the Verlet step. From Newton's 3rd law and the fact that we know the constraint forces to be directed along the bond, we have:

$$\mathbf{g}_H = \lambda_{OH}\mathbf{r}_{OH}(t) \quad : \quad \mathbf{g}_O = -\lambda_{OH}\mathbf{r}_{OH}(t) \tag{5.25}$$

So Equation 5.24 becomes:

$$\mathbf{r}_H(t+\delta t) = \mathbf{r}'_H(t+\delta t) + \frac{(\delta t)^2}{m_H}\lambda_{OH}\mathbf{r}_{OH}(t) \tag{5.26}$$

$$\mathbf{r}_O(t+\delta t) = \mathbf{r}'_O(t+\delta t) - \frac{(\delta t)^2}{m_O}\lambda_{OH}\mathbf{r}_{OH}(t) \tag{5.27}$$

Then by combining Equations 5.26 and 5.27 we can write the equation:

$$\mathbf{r}_H(t+\delta t) - \mathbf{r}_O(t+\delta t) = \mathbf{r}'_{OH}(t+\delta t) + (\delta t)^2\left(\frac{1}{m_H} + \frac{1}{m_O}\right)\lambda_{OH}\mathbf{r}_{OH}(t) \tag{5.28}$$

Since we know the LHS $|\mathbf{r}_{OH}(t+\delta t)|^2$ is equal to the constant d_{OH}^2, we can square both sides of 5.28 to get a quadratic in λ_{OH} (or n quadratic equations for n bonds in a molecule) which can be solved to find the optimum positions consistent with a constrained molecular geometry. It is worth noting that the resulting equation means that the accuracy of the SHAKE algorithm and hence the precision of the molecular geometry is dependent on the timestep (δt) to the fourth power, so it is particularly important to use a small increment.

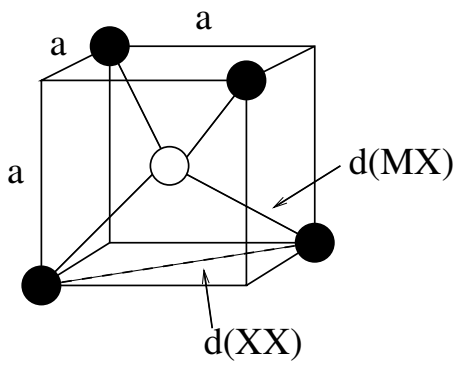

$$d_{MX} = \frac{\sqrt{3}}{2}a \tag{5.29}$$

$$d_{XX} = \sqrt{2}a \tag{5.30}$$

$$d_{XX}^2 = \frac{8}{3}d_{MX}^2 \tag{5.31}$$

Figure 5.17: Constrained interatomic separations in tetrahedral molecule.

As well as coding the constraints for diatomic molecules, we went on to extend the method for triatomic 'MX_2' and tetrahedral 'MX_4' type molecules. With the latter two we tried two different options that arose with the constraints: fixing the distance between the central and terminal atoms only, thus allowing flexible bond angles but fixed bond lengths, and fixing both the M-X and X-X distances to give completely rigid molecules.

Having coded the constraints into our MD program, the next step was to find a way to extract the constraint or non-shape-changing forces from both the *ab initio* sets used in a fit, and from the sets the MD code iteratively produces during the fit as the potential is optimised. This is not an entirely straightforward or a documented process: SHAKE does not work with forces, rather with positions, as shown in Equation 5.24, and the iterative nature of its finding the atomic positions meant that we had to extract the **g** factor for each atom at each iteration as the positions were nudged around, and accumulate them into an array. The non-shape-changing forces are then given by adding g to the unconstrained force **f** as in Equation 5.22.

Some error was introduced into the constraint force extraction because the values of **g** we were working with were very small compared to the magnitudes of **f**. (This can be seen ahead in Figure 5.21 where the constrained and unconstrained forces resulting from a fit are compared.) In order to check the accuracy was acceptable we compared the final positions $\mathbf{r}_i$ predicted by SHAKE, with those obtained by using Newton's laws with the extracted constraint forces - the results are shown for five constraint variations over three different systems in Table 5.7. The tolerance is the precision to which we required SHAKE to match the ideal bond length for each molecule.

System	tolerance (d_{ij})	10^{-4}	10^{-8}	10^{-12}
$Mg(OH)_2$, fixed lengths	# iterations	1	1-2	2-3
	consistency in $\mathbf{r}_i$	4-6 dp	4-6 dp	4-6 dp
$Cs_4(UO_2)_2Cl_8$, fixed lengths	# iterations	2	4	6
	consistency in $\mathbf{r}_i$	4-6 dp	4-6 dp	4-6 dp
$Cs_4(UO_2)_2Cl_8$, fixed lengths & angles	# iterations	2-3	NA	NA
	consistency in $\mathbf{r}_i$	4-6 dp	NA	NA
Li_2SO_4, fixed lengths	# iterations	2-3	7	11
	consistency in $\mathbf{r}_i$	7-8 dp	7-8 dp	7-8 dp
Li_2SO_4, fixed lengths & angles	# iterations	1-5	26-138	200-350
	consistency in $\mathbf{r}_i$	6-7 dp	6-7 dp	6-7 dp

Table 5.7: Accuracy of the extracted constraint forces.

Extracting the non-shape-changing forces from the *ab initio* sets required us to

code a 'dummy' SHAKE routine into the fitting program, within which we accumulated the *ab initio* non-shape changing forces.

During the testing it became apparent that the simulations with the rigid triatomic MX_2 have stability problems when we try to be too rigorous with the constraint-accuracy SHAKE has to work to. We believe this is due to the particular symmetry of the molecule: with 3 fixed lengths it is possibly over-constrained, as it only needs the X-X and one M-X bond fixed to remain rigid. Removing one of the M-X constraints does not and did not help when we tried it, but a solution has been reached for this problem in other work by using a different method [81, 82]. This method uses an algorithm which is non-iterative, so the occasional instance of divergence arising from a failure of the iterative method we use to optimise the constraints in a particular molecule does not arise. This method has been successfully tested with the carbonate molecular ion [83]. However our method here was adequate for the purpose of developing the fitting procedure. Another result of these tests was that we could see that the accuracy of the extracted forces did not increase on tightening SHAKE's geometry tolerance below a factor of 10^{-4} for the fixed lengths. The accuracy seemed rather to be system-dependent, though always at an acceptable level. The number of iterations increased with the number of constraints as would be expected.

5.6 Fitting Intermolecular Potentials Using Constraints: First Results

5.6.1 The First Fits, Using a Rigid Ion Model

Now ready to start the fitting process using the constraints method, we used the best potential from the harmonic spring fits to generate new sets of $Mg(OH)_2$ configurations for CASTEP to perform calculations on, this time obeying the bond length constraints. The radial distribution functions relative to the oxygen atom are shown in Figure 5.18. The O-H peak exhibits a single sharp peak at the con-

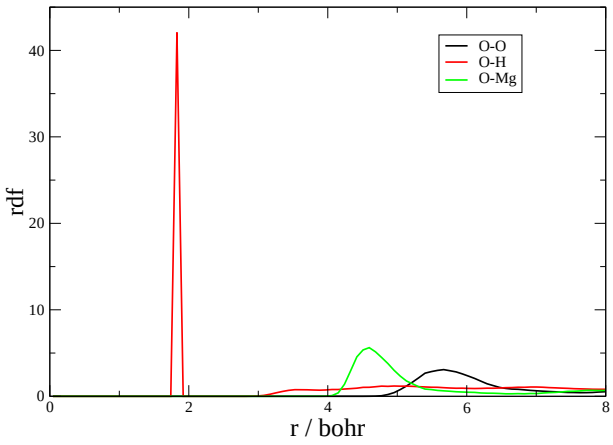

Figure 5.18: Radial distribution function of the atoms in the simulation of $Mg(OH)_2$ from which we took configurations of constrained molecular geometry for use in CASTEP calculations.

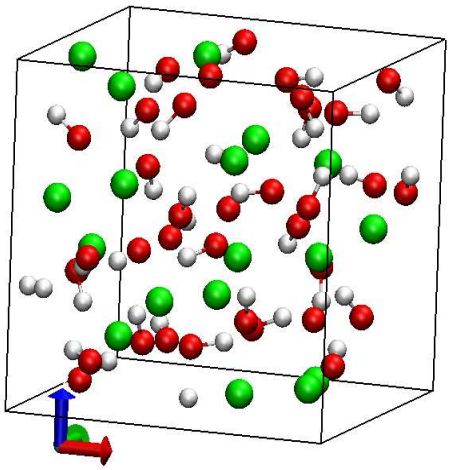

Figure 5.19: Snapshot of a near-liquid $Mg(OH)_2$ simulation from which our fit-configurations were extracted: red=O, white=H, green=Mg.

strained bond-length as would be hoped. The simulation was run at a temperature of 500 K, which with the potential we used resulted in near-liquid configurations, as suggested in the snapshot taken in Figure 5.19. This is acceptable for the first round of fitting and a wide range of forces will be sampled this way, though in refining the potential further it would be a good thing to include crystalline configurations as well in order to fine-tune the parameters to reproduce forces which would closely resemble those within the structure we wish to replicate.

We began fitting using the simplest form of interaction potential: the rigid ion model, fixing the O-H bond length at the crystallographic value, as in the spring-bonded fitting, and as a starting point using the partial charges of $O^{1.4-}$ and $H^{0.4+}$ which were suggested by the makers of the Morse potential from which our empirical potential was derived. We chose three configurations from the simulation, the total number of atoms for which the data was used in the fitting process being 270. The forces resulting from this first fit are shown in Figure 5.20 alongside the *ab initio*-derived forces. The fit quality χ^2 was 3.68; better than the equivalent fit using intramolecular springs which produced a χ^2 of 4.36. As a further comparison, we calculated the value of χ^2 corresponding to the *ab initio* forces and those predicted by

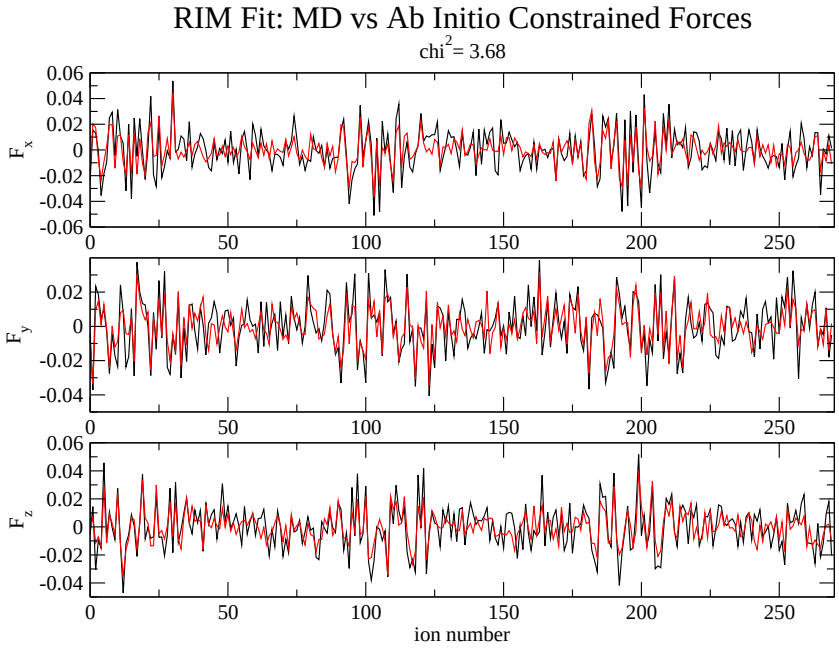

Figure 5.20: Comparison of *ab initio* forces and those predicted by our first RIM potential using the constraints method. (Forces given in atomic units.) In these diagrams with the simulation cell set-up we have used, the forces on the respective ions lie in the following ranges along the abscissa: oxygen 1-36, 90-126, 180-216; hydrogen 37-72, 127-162, 217-252; magnesium 73-90, 163-180, 253-270.

the original empirical potential. The newly fitted potential compared even better here, with the empirical potential having a χ^2 of 8.14. The a comparison of the *ab initio* versus the empirical model forces is shown in Figure 5.20, and they are evidently some way off the mark. Given that the empirical potential is a direct analogue of the Morse potential used in previous work, this comparison of the forces emphasizes the need for development of more accurate interaction potentials for this type of material.

For better insight into the forces we were dealing with, we plotted out the forces before and after the shape-changing components had been removed by SHAKE in the fit, as shown in Figure 5.21. This comparison of **g** and **f** from Equation 5.22 helped us to picture what exactly was going on in the fitting process. As can be seen, the amount SHAKE has to change the forces in order to nudge the atoms back to form molecules of fixed shape is tiny compared to their total magnitude.

Another way of gaining more insight into the process was to plot out the forces

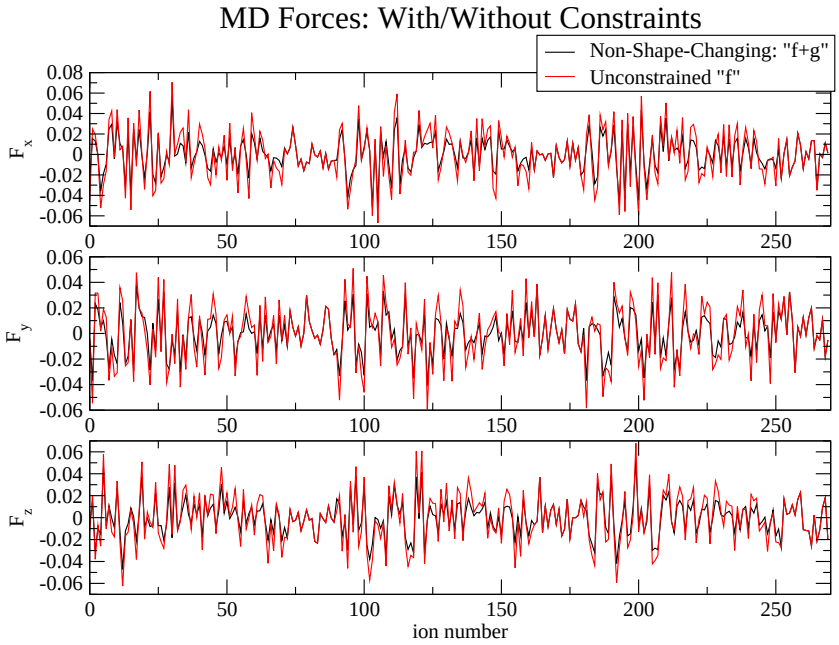

Figure 5.21: Diagram of the forces (in atomic units) on each atom in a fit before and after the constraints have been applied.

between pairs as a function of separation under the fitted potential, alongside the radial distributions functions for the respective pairs. This is done in Figure 5.22, and gives an idea of how much each pair sample each other's potential walls relative to the other pairs. It shows the O-O and O-Mg force-curves overlapping the corresponding R.D.F.s to a much greater extent than the Mg-Mg: the resulting pair potentials for O-O and O-Mg should therefore be based upon a more reliable set of short-range forces as the ions sample each other's potential walls more fully than the Mg-Mg pairs. In practical terms, this means it is debatable how far it is feasible to refine the Mg-Mg parameters, as their contribution to the total short-range repulsive force on the other is drowned out by the other surrounding ions. It may therefore be best to fix the Mg-Mg parameters at what seem to be appropriate values based on occasional fits along the way and allow the fitting program to focus on optimising the O-O and O-Mg parameters.

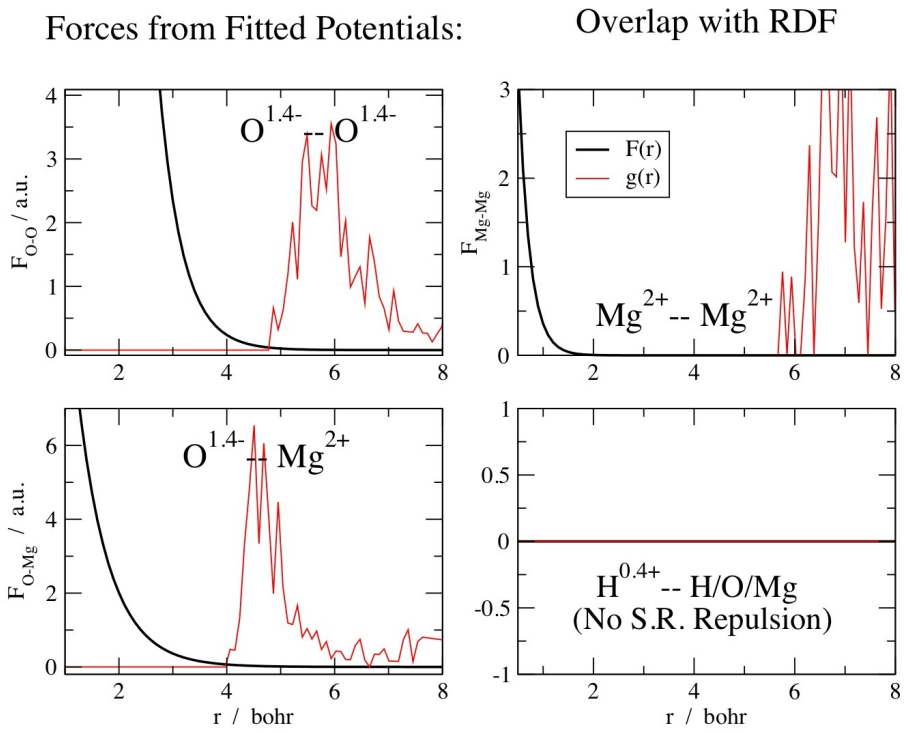

Figure 5.22: Plots of the radial distribution functions versus the forces between pairs of a function of separation, for the $Mg(OH)_2$ configurations used in our fits.

5.6.2 Refining the RIM Potential by Considering the Intramolecular Charge Distribution

As the next step in refining the potential, we thought more carefully about how the charge should be distributed within the molecules. We know that the charges on the O and H atoms in the $(OH)^-$ ion are not the full ionic charges of -2 and +1, and that previous work [76] has suggested -1.4 and +0.4. However, as their short range part of the potential proved quite off the mark in predicting the forces within the $Mg(OH)_2$ system (at least as to be consistent with CASTEP's forces), it certainly seemed a likely area for improvement. So, as the most straightforward thing to try first, we fit the forces at several incremental charge distributions within the OH^- molecular ions. The results are shown in Figure 5.23 and Table 5.8.

From this series of fits we see that the full ionic charges produce a very poor agreement between the fitted and *ab initio* forces, as would be expected since the bonding in the OH^- molecular ion is covalent and the electron density delocalised

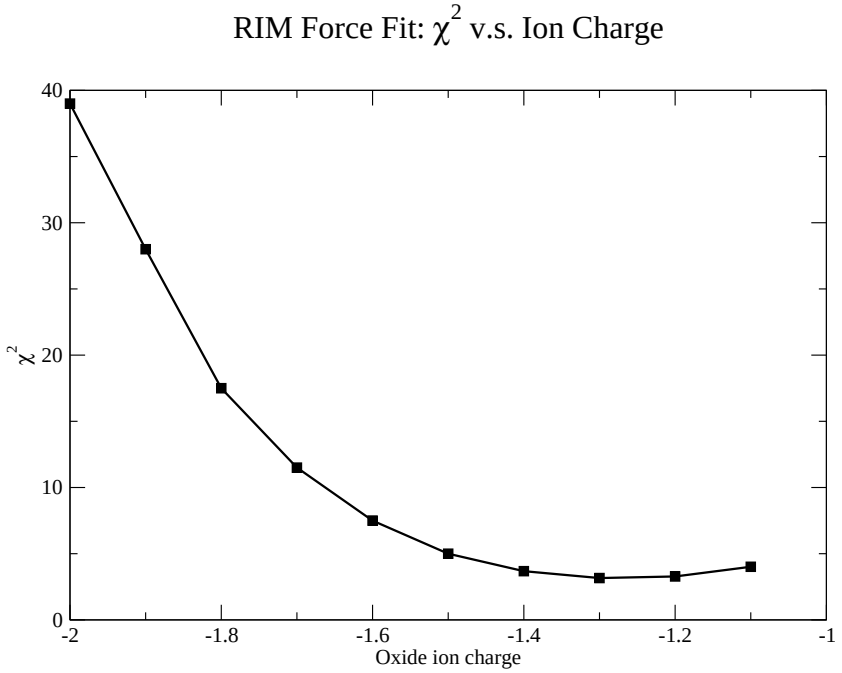

Figure 5.23: RIM fit quality versus oxygen charge in $Mg(OH)_2$.

Q_O	2.0-	1.9-	1.8-	1.7-	1.6-	1.5-	1.4-	1.3-	1.2-	1.1-
Q_H	1.0+	0.9+	0.8+	0.7+	0.6+	0.5+	0.4+	0.3+	0.2+	0.1+
χ^2	39	28	17.5	11.5	7.5	5.0	3.68	3.16	3.28	4.01

Table 5.8: RIM fit quality versus partial charges on the O & H atoms in $Mg(OH)_2$.

around the whole molecule, as evident from our calculations shown in Figure 5.24. A comparison of the *ab initio* and fitted forces from the fit with full ionic charges and a χ^2 of 39 is shown in Figure 5.25. It can be seen that the forces from the fitted potential are much larger than the *ab initio* ones, due to the large Coulombic contributions from the high ionic charges.

The fit parameter χ^2 reaches a minimum of 3.16 in our fits at a charge of Q_H=0.3+, looking like the absolute minimum is reached a little lower at a charge Q_H of around 0.28+. These are somewhat lower magnitudes of the charge than the values from the Morse and empirical potentials, suggesting the charges predicted by CASTEP are more evenly distributed around the OH^- molecular ions.

As an extension of this method, we modified the fitting program further to include the charges on the oxygen and hydrogen atoms as fit-parameters, to hopefully

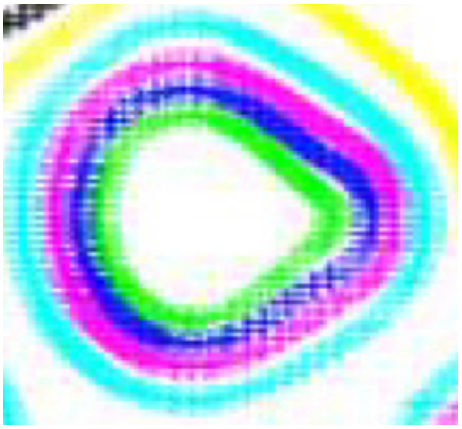

Figure 5.24: Contour map of the electron density in an $(OH)^-$ ion: the concentric contour lines represent levels of equal electron density, where the density increases closer to the ion.

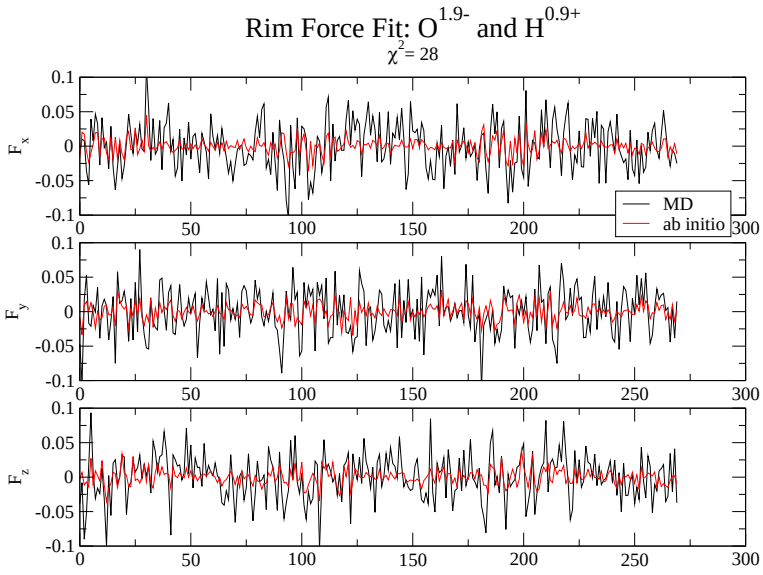

Figure 5.25: Comparison of *ab initio* and fitted forces using fixed charges of 1.9- and 0.9+ on the O and H atoms. Forces are in atomic units.

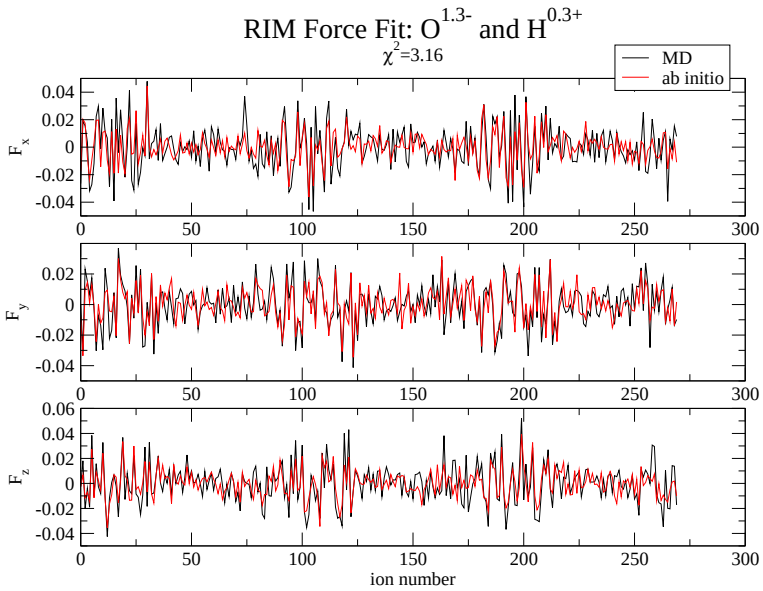

Figure 5.26: Comparison of *ab initio* and fitted forces using fixed charges of 1.3- and 0.3+ on the O and H atoms. Forces are in atomic units.

pin down the optimum partial charges. Firstly we tried fixing the short range parameters at their values from the best fit which had a corresponding charge of $O^{1.3-}$. This gave a marginally higher χ^2 of 3.17, which makes sense as we were reducing the number of degrees of freedom in the fit, and gave partial charges of $O^{1.288-}$ and $H^{0.288+}$, closer to the minimum in Figure 5.23. Next we tried fitting the charges along with the short range parameters. This way, we hoped to find the true minimum of χ^2 and the optimum corresponding partial charges. However this did not result in any significant improvement in fit quality, giving a χ^2 of 3.15 and partial charges of $O^{1.273-}$ and $H^{0.273+}$ which look to be directly in the minimum of Figure 5.23.

5.6.3 Modeling the Short Range Repulsion for the Hydrogen Atom

In our modeling of the hydrogen short range interactions so far we have made the basic assumption that since the H^+ ion has no electrons, there will therefore be no overlap repulsion of the shells with those of surrounding atoms, and we have set the Fumi-Tosi pre-exponential parameters B to zero, as seen in Figure 5.22. It can

also be seen in the plots comparing the *ab initio* and fitted forces so far that the forces on the hydrogen atoms coincide the least well, where the H atoms lie in the ion number range 37-72, 127-162, and 217-252. So this makes it worthwhile paying closer attention in particular to the pair potential parameters involving hydrogen. In reality however we know that there is a not insignificant electron density surrounding the H nuclei in molecular systems such as this, which can be seen in the way the contours encompass the entire OH^- molecular ions in Figure 5.2.

We then tried fitting the same configurations, but using finite short range hydrogen interaction parameters this time, and including them in the fit. This produced the best match in forces yet: a χ^2 of 2.34 and an improvement in the fit quality of the forces on hydrogen (though they still appear to match the least well of the three species), as can be seen in Figure 5.27.

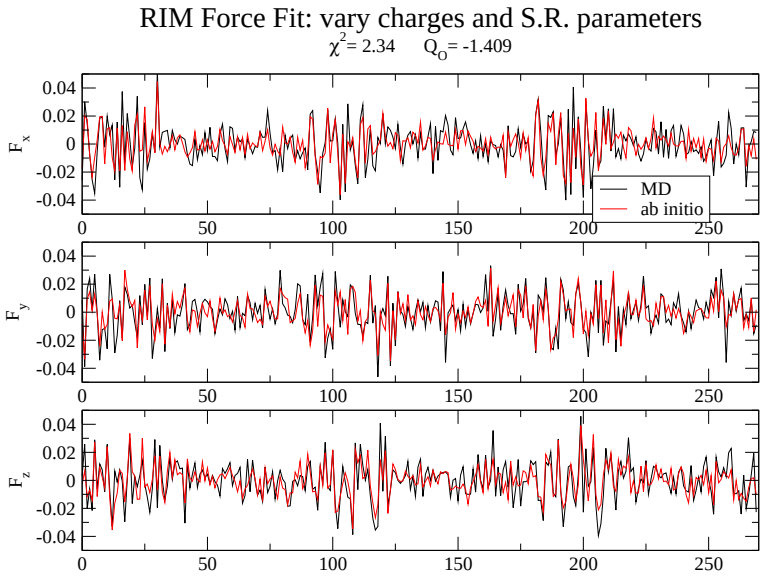

Figure 5.27: Comparison of *ab initio* and fitted forces on adding short-range hydrogen interactions to the $Mg(OH)_2$ potential model. Forces are in atomic units.

So by omitting the short range H interactions so far, we had been using an over-simplistic model, and it appears that by accounting for the electron density delocalised onto the H atoms we improved the force fit quality on all species in the system, especially those on the hydrogens. This minimum of 2.34 we had reached

Fit Method	χ^2
Empirical potential	8.14
Unconstrained with harmonic springs	4.36
Constrained, fitting to intermolecular forces	3.68
Constrained, also fitting partial charges	3.15
Constrained, adding s.r. H interactions	2.34

Table 5.9: Improvement in fit quality for $Mg(OH)_2$ as we refine the fit method for the RIM potential.

was not yet a 'good' value of χ^2 but we had made significant improvements from the first attempts, outlined in Table 5.9. Also, it would be expected that polarization would play a larger role with molecular than atomic systems, as molecular ions are more diffuse than atomic ions. Therefore the next step was to go on to extend the molecular ion model to incorporate polarization and modify the fitting technique to optimise the associated parameters. This work is presented in the next chapter.

Chapter 6

Potentials with Polarizable Molecular Ions

6.1 First Tests: Looking at the Effect of Atomic Polarization

This section describes how we developed the polarization model for the O-H^- molecular ion and modified the fitting procedure to work with it. As a first step it seemed a good idea to try simply allowing the oxygen atoms to form dipoles as if the system were atomic, using the same method as for the dipolar cryolite, AlF_3 and NaF simulations in chapters three and four. This was a relatively quick and easy way to see what sort of improvement in fit quality we could expect on adding polarization to the model: we would expect it to be a significant difference given the great improvements brought to the force-matching in atomic systems by allowing the anions to form dipoles, where the more diffuse electron density delocalised around a molecule renders it much more polarizable than an atom of similar mass, so the corresponding force fits should therefore be more greatly affected on moving from a rigid-ion to a polarizable model for a molecular system.

In the first attempt we stuck to using just the forces on the atoms as our fitting-data, in order to get the direct comparison of fit qualities with the RIM potentials from the previous section. Allowing the oxygen atoms to form dipoles, we then fixed the polarization parameters to the values given in Table 6.1 while fitting the potential: these values were taken from a previously fitted MgO potential [80].

α_O	b_{OH}	c_{OH}	b_{OMg}	c_{OMg}
10.0	2.1	1.0	1.71	1.866

Table 6.1: The polarization parameters we used to get an initial picture of the improvement in fit quality that could be expected by adding polarization to the potential model for a molecular system ($Mg(OH)_2$); values are in atomic units.

Fitting the short range parameters (including those for hydrogen) and the partial charges on the O and H atoms, as in the best RIM fit, we saw a significant improvement in fit quality, χ^2 dropping from to 2.34 to 0.9, which was excellent incentive for continuing along these lines. The partial charges tended to similar values as before, $O^{1.19-}$ and $H^{0.19+}$.

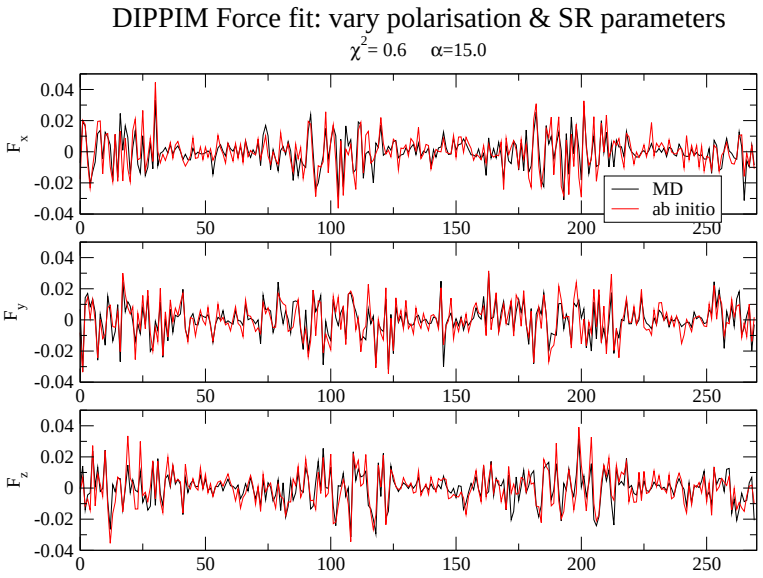

Figure 6.1: Comparison of *ab initio* and fitted forces in $Mg(OH)_2$ on allowing the oxygen atoms to form dipoles, fitting the short range parameters and the polarization parameters all together. Forces are in atomic units.

Next we tried allowing the polarization parameters to vary as well as the short-range parameters, while keeping the partial charges fixed at $O^{1.2-}$ and $H^{0.2+}$, the approximately optimum values suggested by the work so far. The result was another great improvement in the fit quality - χ^2 reached a value of 0.60, and the comparison of *ab initio* and fitted forces are shown in Figure 6.1. In this we see a similar improvement in fit quality across all species, showing the important role polarization

of just one species plays, system-wide.

In this fit we fixed the boundaries of oxygen's polarizability α_O to values that would be generous for the atomic ion, allowing it to vary between 5 and 15 atomic units. The values of the polarization parameters produced from this fit are given in Table 6.2. The value predicted by the fitting program pushed right up against

α_O	b_{OH}	c_{OH}	b_{OMg}	c_{OMg}
15.00	2.13	1.30	1.91	2.25

Table 6.2: Potential parameters produced on fitting the polarization and the short-range parameters all together for a dipolar-polarizable $Mg(OH)_2$ potential. All values in atomic units.

the upper boundary of 15 au, which is somewhat larger than the typical values used for the polarizability of O^{2-} ions in ionic solids such as MgO (though not unreasonable). Considering that oxygen's polarization here is actually representing what should be the polarizability of the entire $(OH)^-$ molecular ion, it is not at all surprising that the fit is behaving in this way. On increasing the upper fit boundary of α_O however and fitting again, α_O increased further but χ^2 increased slightly too - this was suggestive of a fit which was being fed too many parameters to optimise. Adding the partial charges into the fits at this stage turned out to have the same effect.

6.2 The Molecular Polarization Model

The next step was to attempt to model the polarization more carefully. Through this we hope to gain a better understanding of the system so as to be able to model it more accurately. Also, this way we would be able to fit the polarization parameters first, separately, as we did in the cryolite work which means a smaller number of parameters to optimise at a time, defeating the problem we saw creeping in the last fit. The results so far were obtained by simply fitting to the forces and allowing oxygen's dipole parameters to vary.

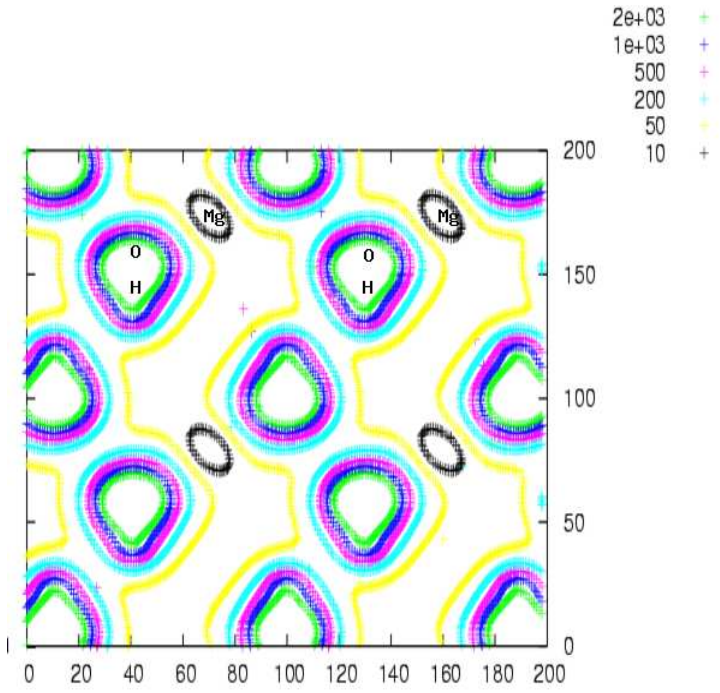

Figure 6.2: Slice of the electron density across the whole $Mg(OH)_2$ simulation cell; a plane coinciding with a layer that contains each of the the three atomic species to illustrate the similarity between the electron density encompassing the discrete Mg^{2+} ions and the OH^- pairs. The axes-scales represent the 200^2 grid points upon which the density slice was calculated.

Looking at the cross section of the electron density across the entire unit cell shown in Figure 6.2 it is apparent that it is wrong to think of the orbitals as belonging to the individual O and H atoms: the surface cuts through all three species and to a best approximation the OH^- molecular ions appear as single entities like the Mg^{2+}, but aspherical. We used this to illustrate the need for partial charges within the molecules in the last section but this also strongly suggests the need for *full molecular polarizabilities*. The density is a property of the whole molecule and we cannot expect an atomic polarization model to accurately represent the true polarization in the system.

So, we needed to find ways to calculate the molecular polarizabilities from both the available *ab initio* data and our classical MD code, to allow us to fit a dipolar-polarizable potential model and run simulations using it. We know a molecular dipole is calculated using Equation 6.1, and is made up of contributions from the

nuclei (the 'permanent' part, $\boldsymbol{\mu}_{perm}$) and the electrons (the 'induced' part, $\boldsymbol{\mu}_{ind}$, which depends upon the surrounding crystal environment):

$$\boldsymbol{\mu} = \boldsymbol{\mu}_{perm} + \boldsymbol{\mu}_{ind} = \Sigma_i Q_i \mathbf{R}_i \tag{6.1}$$

where Q_i are the charges in either model, and $\mathbf{R}_i$ are the displacements from a chosen centre in the molecule.

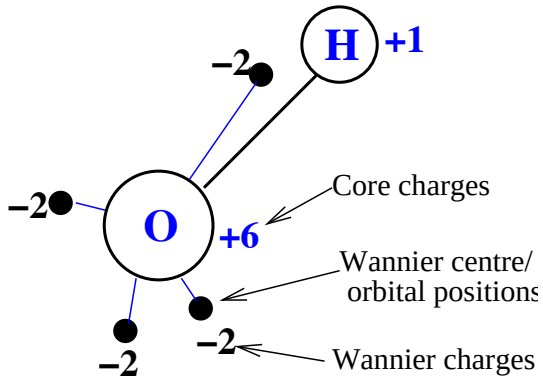

Figure 6.3: Contributions to the full molecular dipole within the $(OH)^-$ ion, as calculated using data from an *ab initio* CASTEP simulation. (The positions of the orbitals were drawn in retrospect from work described later in the chapter.)

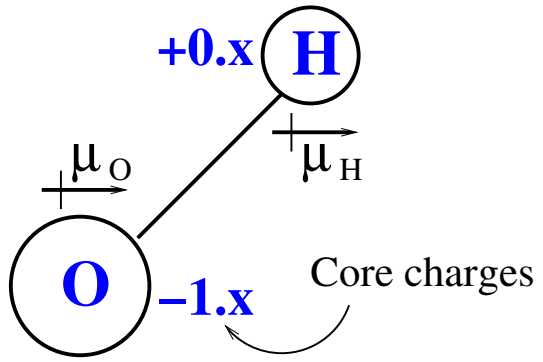

Figure 6.4: Contributions to the full molecular dipole within the $(OH)^-$ ion, as calculated using data from a classical simulation. (The parameter x is the decimal that must be substituted into the charges on both atoms to ensure a total fixed molecular ionic charge of -1.)

We can calculate the permanent dipole straightforwardly, though its physical breakdown in either type of simulation is different: in the classical simulations we do not explicitly model the electrons and the only charges are the ionic ones we

assign to the nuclei, so in the hydroxide ion we would assign the partial charges on either atom to Q_i. In the *ab initio* simulation however, our choice of pseudopotential defines how many electrons we model explicitly and therefore the size of the core charges. Our pseudopotentials for the O and H atoms were 'neutral' and contained 6 and 1 electrons with core charges of +6 and +1 respectively, the 1s shell being treated as 'core' in oxygen's pseudopotential. As a result the value of the permanent dipole is only ever the same for the two methods in the extreme case where we take oxygen as the origin and use full ionic charges of -2 and +1 on O and H respectively, which we know not to accurately represent the system in our classical simulations.

Calculation of the induced dipoles is necessarily different for each type of simulation as well: these differences are the main reason why it did not seem useful to simply fit the induced dipoles alone from our MD code to the *ab initio* set - the physical basis is not quite the same for each, though when combined with the permanent dipole they go to make up the same property. The method and model by which each is calculated is described in the following points:

- The *ab initio* induced dipoles are calculated by summing over the charges of all the electrons explicitly modeled in the pseudopotentials. We perform CASTEP Wannier localisations to determine the positions of the four Kohn-Sham orbitals distributed around each molecule to obtain the necessary values of R_i, as shown in Figure 6.3. All the explicitly modeled electrons occupy orbitals associated with the hydroxide ions, resulting in each OH^- having a total of four Wannier functions associated with it.

- The induced dipoles for each atom as derived from the classical MD code are calculated using a conjugate gradients algorithm which uses a fixed polarizability to set the approximate magnitude, and uses the variations in the electric field at each nucleus to determine the precise values. The induced *molecular* dipole is then found by simply summing over the individual atomic dipoles within that molecule (shown in Figure 6.4). This can be proved by expanding

the atomic dipoles as an imaginary set of charges, and changing the coordinate origin to any one of the atoms in the molecule.

An issue arises with the calculation of the atomic induced dipoles in the latter case though, which for atomic systems has always been done using Equation 6.2.

$$\boldsymbol{\mu} = \alpha \mathbf{E} = \alpha \left(\mathbf{E}_q + \mathbf{E}_{sr} + \mathbf{E}_{did} \right) \tag{6.2}$$

The origin of the induced dipoles can be broken down into three contributions to the electric field $\mathbf{E}$: the Coulombic contribution $\mathbf{E_q}$ from surrounding ions, the short-range damping $\mathbf{E_{sr}}$ and the dipole-induced-dipole $\mathbf{E_{did}}$. The latter is not an issue in our work with the diatomic OH^- molecular ion since we only allowed the oxygen with appreciably deformable valence orbitals to be polarizable. However with this molecular model we should no longer be including short-range and Coulombic contributions from atoms within the same molecule, so we made modifications to cut them out. Since only the oxygen is modeled as polarizable, the induced molecular dipole is simply equal to the induced atomic dipole μ_O.

6.3 Testing and Understanding the Molecular Polarization

To help us put together a picture of the polarization and its contributors we first looked at the induced dipoles as calculated by our MD code and extracted the values with and without intramolecular contributions to the electric field, as well as the values with just the short range *or* just the Coulomb terms contributing. The results are plotted in Figure 6.5. From this we see that the dipoles with just one contribution (not a physically realistic scenario) are roughly the mirror images of each other with relatively large magnitudes, showing the short range and Coulombic effects tend to cancel each other out. We also see that the dipoles with neither or both contributions are fairly similar and follow the same pattern, the former being slightly larger. We can rationalize the relative sizes using structural considerations:

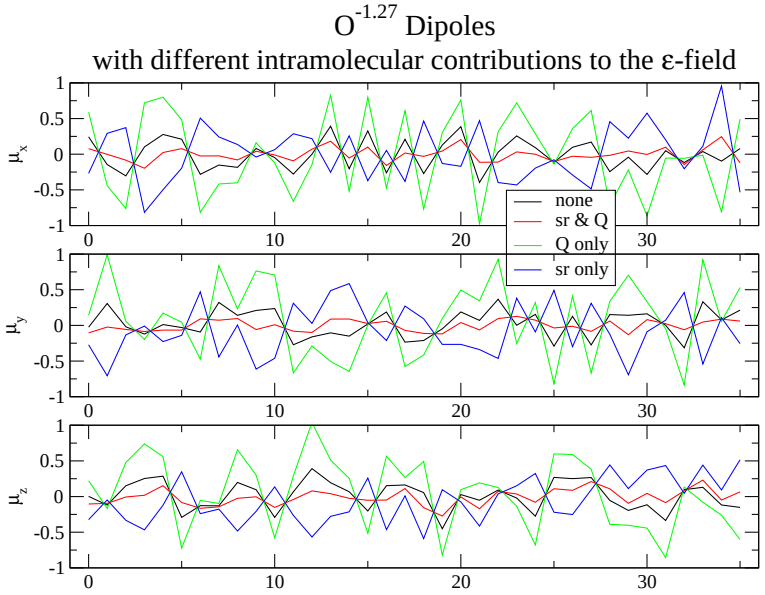

Figure 6.5: The induced molecular dipoles in a thermally distorted solid $Mg(OH)_2$ configuration, in atomic units, calculated with and without intramolecular contributions to the electric field from Coulomb (Q) and short range (sr) effects.

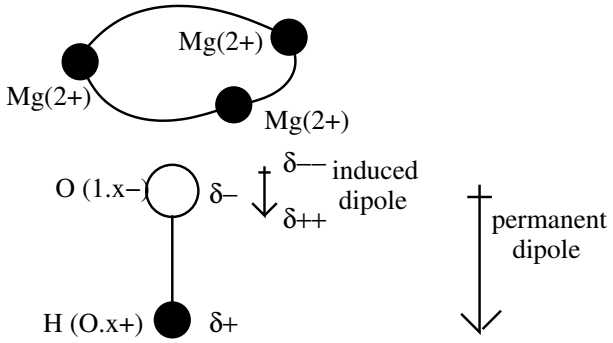

Figure 6.6: Showing the environment of the OH^- ion to help explain the polarization effects in our simulations of $Mg(OH)_2$.

the unit cell is depicted back in Figure 5.13, and the environment of the OH^- ion can be thought of as roughly linear with a tripod of three Mg^{2+} ions lying at the oxygen-end as drawn in Figure 6.6. Without the intramolecular effects, this cluster of positive charges at one end can exert a larger polarization on the oxygen atom. The accordance of these polarization effects with the known structure also (importantly) confirms that our potential model is working well.

We also looked to compare the induced molecular dipoles with the permanent ones - these are plotted alongside each other in Figure 6.7. The induced dipole

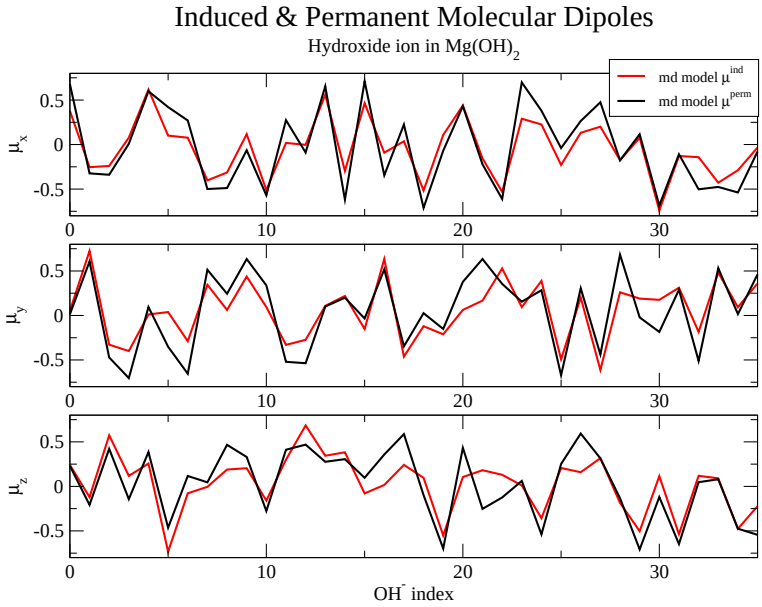

Figure 6.7: Permanent and induced components of the hydroxide ions' molecular dipoles from our simulations of $Mg(OH)_2$.

moments appear to reinforce the permanent ones. This is consistent with the way of picturing the hydroxide ion's environment in Figure 6.6: the negative end of the induced dipole would also point towards the ring of Mg^{2+} ions, the positive charge of the Mg^{2+}s forming a 'δ-' on the outer side of the molecule.

Having dissected the dipoles as calculated from the classical MD model, we went on to run *ab initio* CASTEP simulations to enable us to calculate and understand the molecular dipoles we were to fit to. Firstly we looked at the distribution of the Wannier functions with respect to the two species in the OH^- molecular ions. We saw that there were three Wannier centres equidistant from each oxygen atom plus one at a slightly greater distance, accounting for all four valence orbitals. From the hydrogen's RDF we were able to see that this last orbital was drawn along the bond between the two atoms, as drawn back in Figure 6.3, in a way that is consistent with covalent rather than ionic bonding. A selection of the Wannier functions are plotted out as surfaces of volumetric datasets, shown in Figure 6.9 (in blue). We saw that they came in two physical types - those with a large lobe along the bond and another directly behind the oxygen, and those with just one large visible lobe

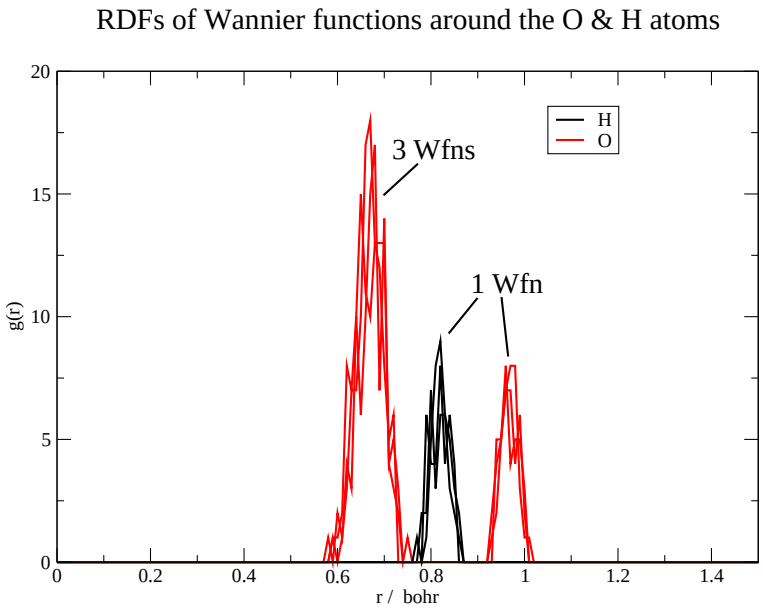

Figure 6.8: Radial distribution of Wannier functions associated with the OH^- molecular ions, with respect to oxygen (red) and hydrogen (black).

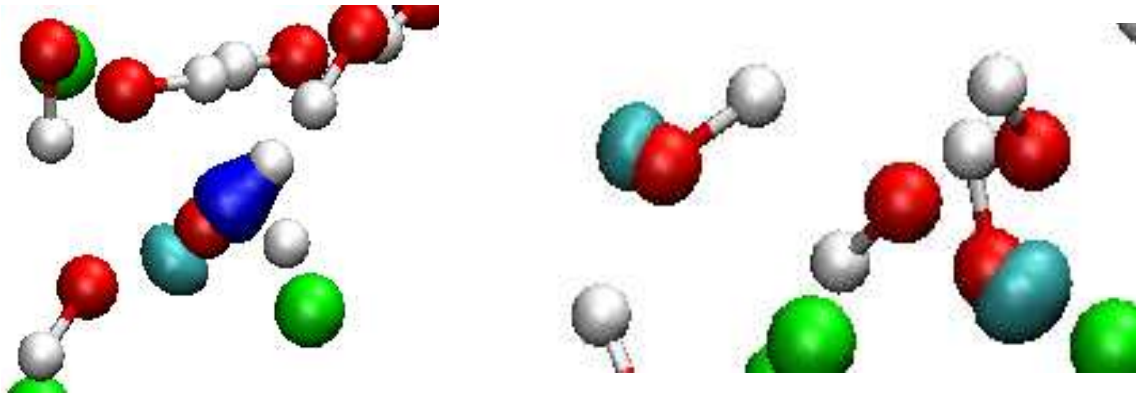

Figure 6.9: Showing the two 'types' of orbital, or Wannier function (in blue), that we observed in CASTEP Wannier localisations of the electron density around the OH^- ions in $Mg(OH)_2$. The oxygen atoms are red, the hydrogen atoms white and the magnesium atoms green.

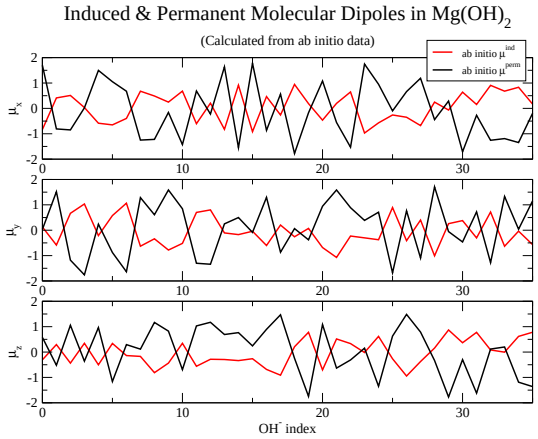

Figure 6.10: Induced versus permanent molecular dipole moments (in atomic units) as calculated for the hydroxide ion in $Mg(OH)_2$ using *ab initio* data.

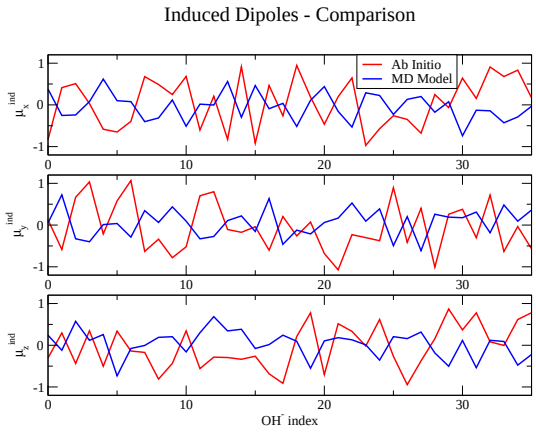

Figure 6.11: Comparison of the induced molecular dipoles (in atomic units) calculated by the *ab initio* and classical simulation methods.

at an angle off the back of the oxygen-end of the molecules. The way these mirrored descriptions of bonding and anti-bonding orbitals was a very good sign that the Wannier localisation was coping well with molecular systems and its results would be equally reliable as the basis for calculating multipoles.

Looking at the induced versus the permanent components calculated from the *ab initio* data in Figure 6.10, we saw there was a very different relationship between the two than in the classical model. Here the two *oppose* each other. This is what would be expected since the direction of the permanent dipole moment has been reversed by the change in charges on the atoms from the typical ionic ones of $O^{1.x-}$ & $H^{0.x+}$ to the pseudised nuclear charges of O^{6+} & H^{1+}. The induced components in the *ab initio* and classical sets are necessarily different too, as shown in Figure 6.11.

With this insight into the polarization, we next went on to attempt to fit a dipole-polarizable potential model for $Mg(OH)_2$.

6.4 Fitting a Dipolar Polarizable Potential for $Mg(OH)_2$ with Full Molecular Polarizabilities

6.4.1 The First Round of Fitting a Dipolar Polarizable Potential

We proceeded to fit the molecular dipoles from our model to the *ab initio* dipole values, in the first step of the process where we optimize the polarization parameters: the oxygen's polarizability and the charge-dipole damping parameters. For this we chose partial charges of $O^{1.2-}$ and $H^{0.2+}$, approximately the best values from rigid ion fitting. At this stage we used the same near-liquid configurations that were used to refine the RIM potential in section 5.6. Even in this first attempt we saw that the fit quality was exceptional, as good as any *atomic* dipole fit carried out in the cryolite work, with a χ^2 of 0.0195. The molecular dipoles derived from CASTEP are plotted alongside the ones predicted by our MD program with the fit potential in Figure 6.12. These excellent first results vouched for both the accuracy of our method of modeling the molecular polarizabilities from the two sources, and for the way we had implemented them in the fitting process.

Next we went on to optimize the partial charges on the O and H atoms according to what produced the best dipole-fits, by re-running the fit at increments over a range of charges. We also looked to see how the change in charge distribution effected the overall polarizability of the molecules, using the values of α output by the fitting program. Figure 6.13 shows the variation in χ^2 and the molecular polarizability α with varying charge distribution.

We saw that as the magnitude of the charges increased in the molecules, the polarizability tended to decrease. This makes sense because as the partial charge of hydrogen (Q_H) increases the permanent contribution to the molecular dipole increases, so the induced dipole decreases to compensate and match the *ab initio* dipole values. However there was a clear minimum to the curve of χ^2 with respect to Q_H, so although there is some artificial shifting of α when the partial charges are off

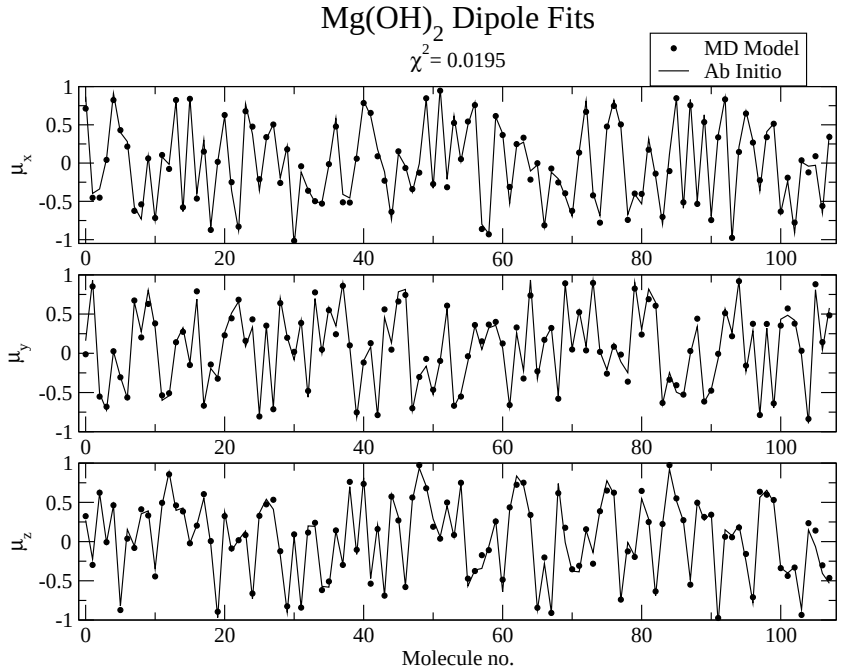

Figure 6.12: First $Mg(OH)_2$ molecular dipole fit, using charges from best RIM fit of $O^{1.2-}$ and $H^{0.2+}$. Dipoles given in atomic units.

the mark, there is still a clearly discernible optimum point on the energy landscape.

The parameter χ^2 reached a minimum at a reasonable intermediate value of Q_H=0.3, giving a polarizability of approximately 12 atomic units, though the best value of χ^2 looks to be just under Q_H=0.3. All of the fits in this appreciable charge range however were of excellent quality. From the work so far it would appear that the quality of the forces is much more sensitive to the partial charges on the atoms, presumably because the short-range parameters cannot be optimized in a way to compensate for the changing values of Q_O and Q_H so as to correct the forces on the ions to reproduce the *ab initio* values.

Finally, we tried including the partial charges in the fit along with the dipole parameters, though some caution was required to avoid the problem of feeding the fitting program too many parameters as happened towards the end of section 5.6. We restricted the range of Q_H to within the narrow range of values we saw the optimum value lay in Figure 6.13: $0.2 \leq Q_H \leq 0.35$. The result was another improvement to χ^2, a very reasonable value for the molecular polarizability and partial charges spot

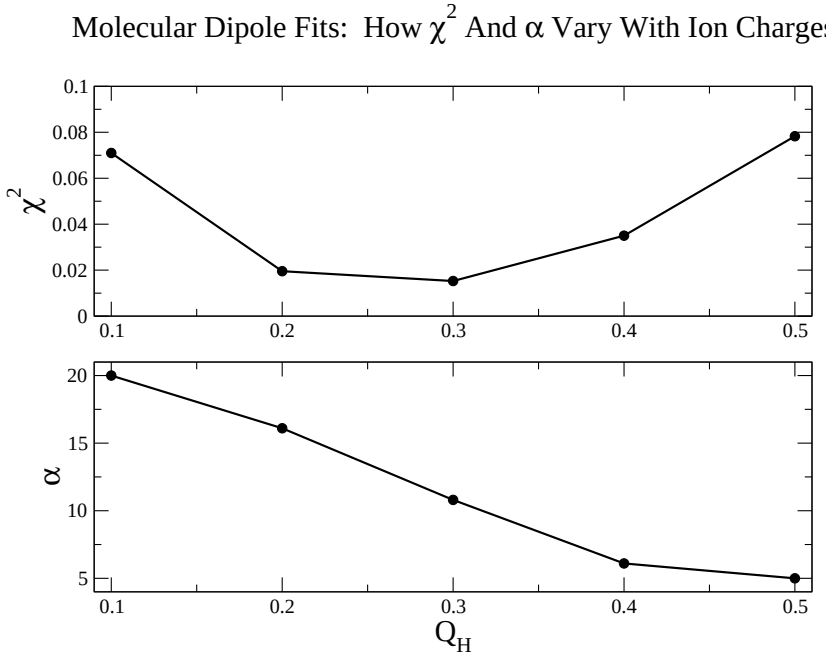

Figure 6.13: Molecular dipole fits for the $(OH)^-$ ion, showing the variation in χ^2 and the molecular polarizability α (in a.u.) on varying the intramolecular partial charges.

on what we would have guessed to be the minimum - the final parameter values are given in Table 6.3, in atomic units.

χ^2	Q_H	Q_O	α_O	b_{OH}	c_{OH}	b_{OMg}	c_{OMg}
0.01360	0.264	-1.264	12.52	3.50	0.80	1.34	0.83

Table 6.3: Optimized polarization parameters obtained by fitting the molecular dipoles derived from our classical model to those from *ab initio* CASTEP simulations. All parameters given in atomic units.

Using the newly fit polarization parameters as fixed values, we went on to fit the corresponding short-range parameters to complete the dipolar potential. The result was a significant improvement on the best RIM fit from section 5.6: χ^2 dropping to 0.9215 versus 2.34. A comparison of the *ab initio* and fitted forces is shown in Figure 6.14. However this did not improve on the very first force fits using an *atomic* dipolar potential in the previous section. So, as far as matching the forces goes, the introduction of dipoles into the potential helps greatly but the precise values of the polarization parameters do not have a great effect on the force fit

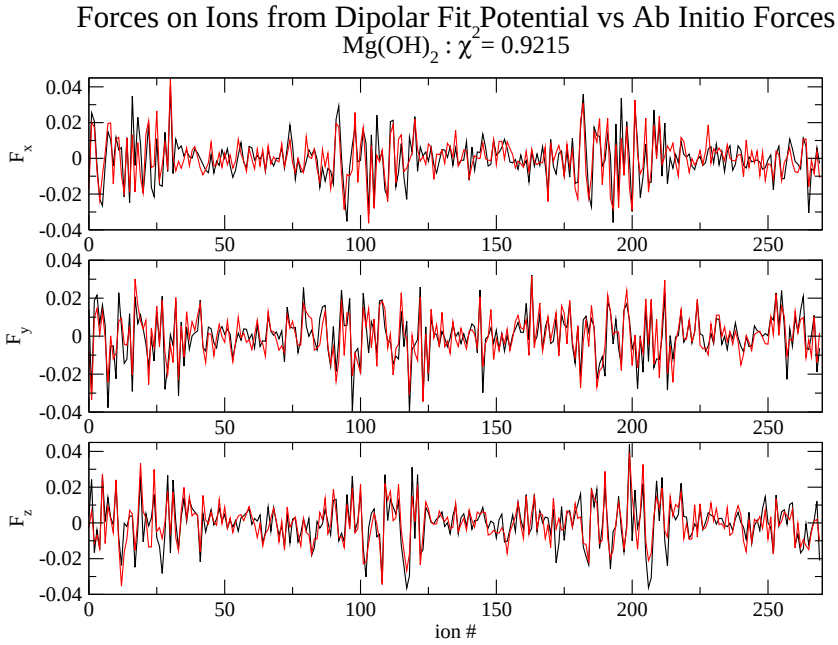

Figure 6.14: $Mg(OH)_2$ force fit using a molecular-dipolar-polarizable potential with near-liquid configurations. Forces in atomic units.

quality. In assessing the quality of a polarizable potential we consider both the quality of the force fits and the multipole fits, and by these criteria this molecular-dipolar-polarizable fit potential is the best so far, since a calculation of χ^2 for the dipoles from the atomic-dipolar-polarizable potential gave 0.06 (versus 0.0136). We would normally judge a fit to be 'good' when χ^2 drops down to a value of 0.1, so although we have developed an excellent model for the polarization, the short-range interactions still require some attention.

6.4.2 Testing the First Fit Potential and the Iterating the Fitting Process for a Dipolar Potential

We ran some test-simulations of $Mg(OH)_2$ with this best-fit dipolar potential as we were interested to see how it fared in terms of stability and reproducing the crystal structure, shown in Figure 5.13. The β-form of $Mg(OH)_2$ has a layered hexagonal CdI_2-type structure, the difference lying in that the anion is now molecular, with the $\delta+$ hydrogen-ends oriented approximately along the c-axis in between the layers. We saw that unlike the empirical potential which melted at approximately 300 K,

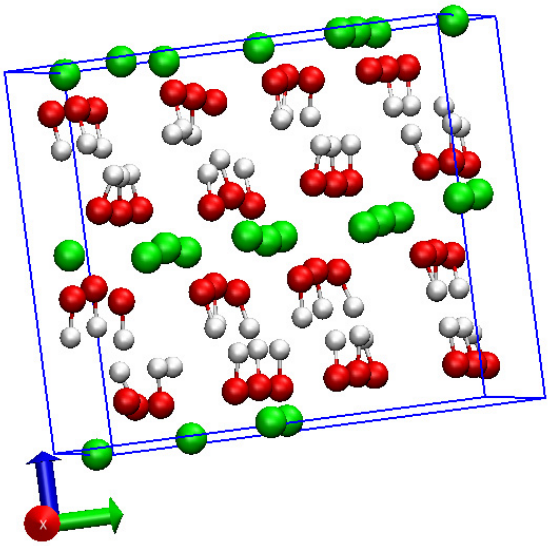

Figure 6.15: Snapshot from simulation of $Mg(OH)_2$ at 300 K using dipolar potential from first round of fitting: view along the a axis (red), showing the layered structure and the dangling O-H bonds between layers.

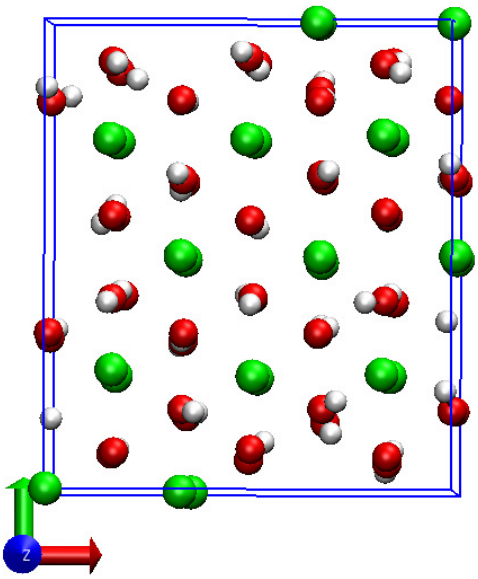

Figure 6.16: View along the c-axis (blue), showing the hexagonal structure. Key: green=Mg^{2+}, red=$O^{1.x-}$ and silver=$H^{0.x+}$.

it reproduced and maintained the β crystal structure excellently at temperatures of up to about 700 K throughout appreciably long simulations, where the melting point of $Mg(OH)_2$ is 623 K [84]. This is similar to the way the cryolite potential from the second round of fitting had a higher point at which ion mobility began to be observable in simulation, at the point we identified with the phase transition which was much closer to that observed experimentally. We used VMD to visualize the simulations as movies, and snapshots from the thermally distorted crystals at a temperature of 300 K are shown in Figures 6.15 and 6.16.

To improve upon this potential further, we decided to try what had worked in potential fitting for cryolite, and generate new configurations using this best-fit potential so far, perform CASTEP calculations on them and go through another cycle of the fitting process. This time around however we chose to utilize the current potential's ability to accurately reproduce the crystal structure, and chose configurations in the β structure from simulations at 300 K and 600 K, covering different degrees of thermal distortion of the ions' environments and hence a wide spectrum

of forces within the crystalline regime. We first transformed the hexagonal cell to orthorhombic, as shown in Figure 6.17, to optimize the cell box for simulation. The hexagonal and orthorhombic cell parameters are given in Tables 6.4 and 6.5.

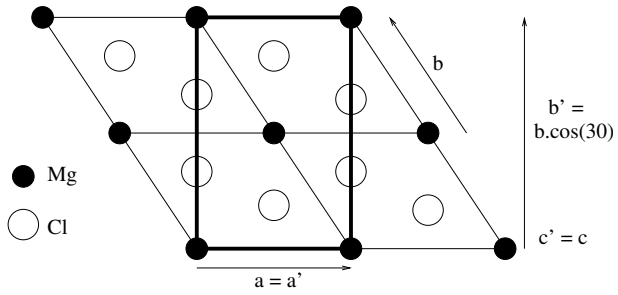

Figure 6.17: Translation to the orthorhombic unit cell of $MgOH_2$.

Cell lengths/Å	$a, b = 3.150$	$c = 4.770$	$\gamma = 120°$
Atomic Coordinates	Mg (0,0,0)	O $\left(\frac{1}{3}, \frac{2}{3}, u\right)$	H $\left(\frac{1}{3}, \frac{2}{3}, u+z\right)$
		O $\left(\frac{2}{3}, \frac{1}{3}, -u\right)$	H $\left(\frac{2}{3}, \frac{1}{3}, -u-z\right)$

Table 6.4: Structural parameters of hexagonal, layered $Mg(OH)_2$, where $u = 0.2203$ and $z = 0.1927$.

Cell lengths/bohr	$a = 5.9522$	$b = 10.3096$	$c = 9.0144$
Atomic Coord's	Mg (0,0,0)	O $\left(0, \frac{1}{3}, u\right)$	H $\left(0, \frac{1}{3}, u+z\right)$
		O $\left(\frac{1}{2}, \frac{1}{6}, -u\right)$	H $\left(\frac{1}{2}, \frac{1}{6}, -u-z\right)$
	Mg $\left(\frac{1}{2}, \frac{1}{2}, 0\right)$	O $\left(0, \frac{2}{3}, -u\right)$	H $\left(0, \frac{2}{3}, -u-z\right)$
		O $\left(\frac{1}{2}, \frac{5}{6}, u\right)$	H $\left(\frac{1}{2}, \frac{5}{6}, u+z\right)$

Table 6.5: Structural parameters of $Mg(OH)_2$ transformed to the orthorhombic unit cell.

Using a simulation box of 3×2×2 orthorhombic unit cells gave us a cell of 120 ions with roughly cubic dimensions, optimum for simulation, being near the size limit in what the supercomputers we had available could run CASTEP calculations on. We ran two simulations, at 300 K and 600 K, from each of which we took three configurations to calculate the forces and dipoles within. All configurations clearly had the solid CdI_2 crystal structure, the 600 K ones being a little more visibly distorted.

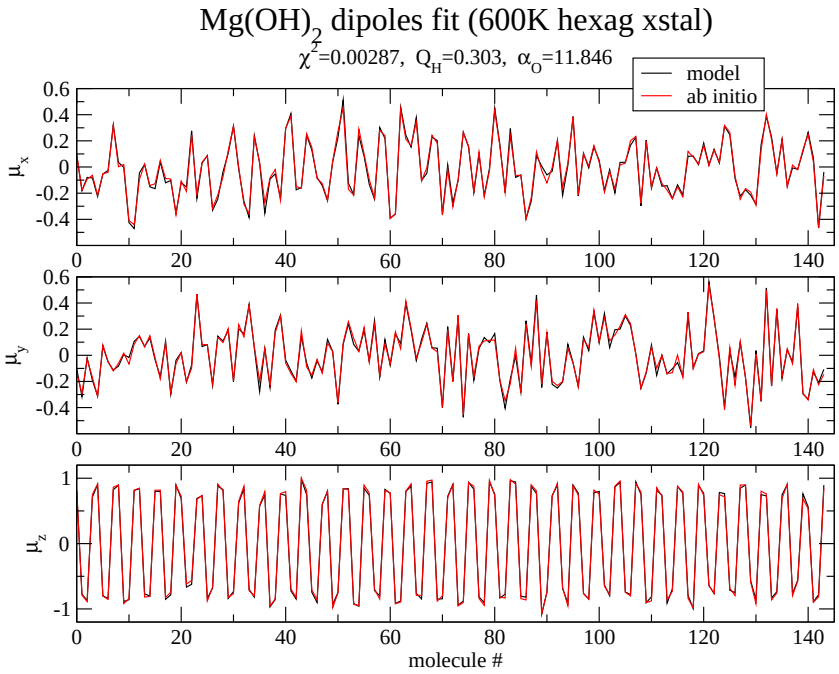

Figure 6.18: *Ab initio* and fitted molecular dipoles in solid crystal configurations of $Mg(OH)_2$ at 600 K. Dipoles in atomic units.

We began the fitting process at the dipolar level, by optimizing the polarization parameters using the molecular dipole fitting method. The molecular dipoles obtained in fitting the 600 K configurations are compared in Figure 6.18. Firstly we saw a further improvement in the fit quality, with χ^2 dropping from 0.01360 in the previous round of fitting to 0.00254 (for all six configurations), which was even better than a typically 'excellent' fit. We saw that the partial charges on the O and H atoms tended to 1.303− and 0.303+ both when fitting the 300 K and 600 K configurations separately and all together, indicating the fit had reached a reliable global minimum with respect to the charges. These partial charges are close to, but marginally higher than the values fitted from the liquid configurations. However, the molecular polarizability α was almost identical to before, reaching a final value of 11.98 atomic units. In the x and y components of the dipoles, which coincide with the a and b axes respectively, we see a typical evenly distributed range of dipoles due to the thermal distortion in the crystal. The z (or c) components have a very distinctive pattern throughout, alternating between similar positive and negative

values of similar magnitude. This is due to the layered structure along the c axis, where the oxygen atoms lie facing each other on either side of symmetrical layers separated only by hydrogens, their environments being approximate mirror images of one another and hence giving approximately equal and opposite dipole moments. The magnitudes of the z components are consequently larger, as it can be imagined that the component of the electric field in this direction would be particularly large. As we would hope though, the magnitude of the dipole *fluctuations* under the thermal motion in the crystal in each component is the same. Once again we see that the charge-dipole damping parameter b is rather higher for the oxygen-hydrogen interaction than the magnesium-hydrogen interaction indicating a 'harder' damping wall (steepness of short-range potential), which seems reasonable considering the diffuseness of the electron densities of the two 'cations' respectively.

These new optimized polarization parameters are given in Table 6.6 and are the values we held fixed on proceeding to fit the short-range parameters using the *ab initio* forces.

χ^2	Q_H	Q_O	α	b_{OH}	c_{OH}	b_{OMg}	c_{OMg}
0.00254	0.303	-1.303	11.98	3.48	3.46	1.69	1.42

Table 6.6: Optimized polarization parameters obtained by fitting the molecular dipoles derived from our classical model to those from *ab initio* CASTEP simulations, using crystalline configurations of $Mg(OH)_2$. Parameters given in atomic units.

On fitting the forces in this second iteration of the fitting process, we saw a vast improvement in the fit quality, with χ^2 for the fit including all six configurations dropping to 0.179. The *ab initio* and fitted forces are compared in Figure 6.19. This had now virtually reached the stage of what we would call a 'good' fit in our work on atomic ions, which was an excellent result for this newly developed fitting process for molecular ions. It seems though that it takes more iterations of the fitting process to achieve similarly good force fits.

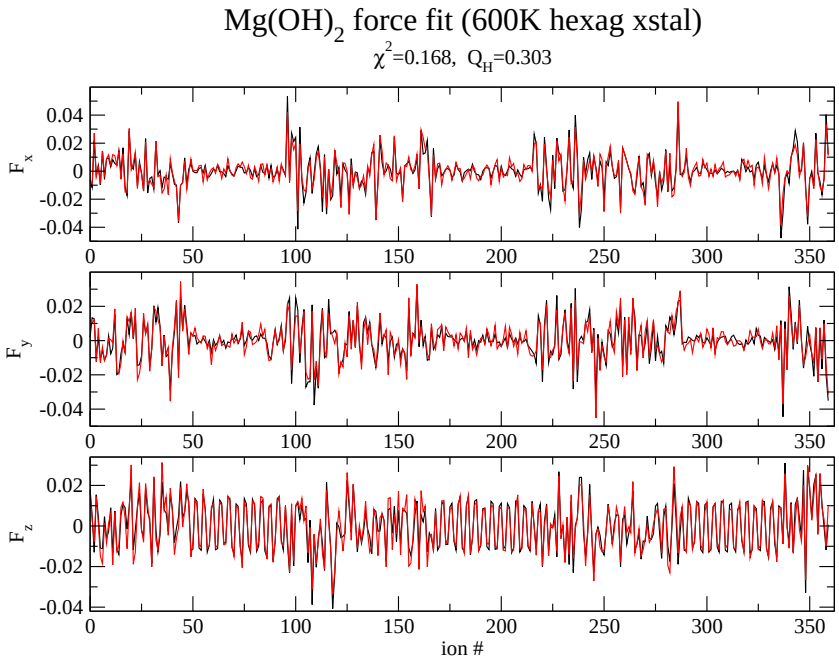

Figure 6.19: *Ab initio* and fitted forces in solid crystal configurations of $Mg(OH)_2$ at 600 K. Forces given in atomic units.

6.5 Comparison with Fitting a Potential for an *Atomic* Layered Structure

In the position now where we had achieved good to excellent force and dipole-fits using this newly developed molecular ion method, we were interested to understand (if possible) how it was that the quality was not quite as good as in fitting a potential for cryolite. Two possibilities presented themselves: one that it was a feature introduced on extending the atomic to the molecular ion model. The second was that the difference lay in the respective structures of the materials. Where cryolite, NaF and AlF_3 have typically ionic structures, $Mg(OH)_2$ has a layered structure which is indicative of something more than the simple ionic bonding upon which our potentials are based and extended from. In layered structures, covalent and dispersion interactions have a more significant role and therefore present more of a challenge for fitting an ionic interaction model.

$MgCl_2$ in its β-form is an example of an *atomic* layered structure similar to the *molecular* layered structure of $Mg(OH)_2$. It has the trigonal space group $P\bar{3}m1$ with

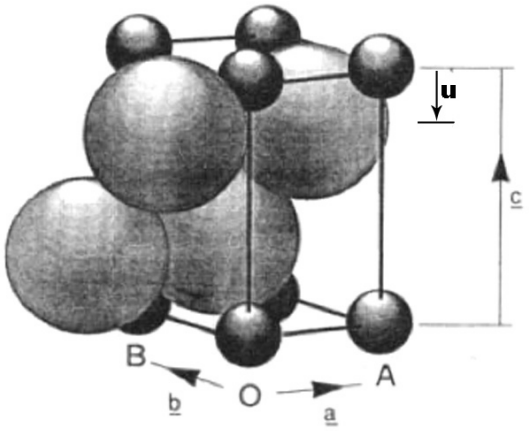

Figure 6.20: The primitive hexagonal unit cell of $MgCl_2$ [85].

a primitive hexagonal unit cell, and the structural parameters given in Table 6.7 [85]. A diagram of the unit cell is shown in Figure 6.20.

Cell lengths/Å	$a, b = 3.641$	$c = 5.927$	$\gamma = 120°$
Atomic Coordinates	Mg (0,0,0)	Cl $\left(\frac{1}{3}, \frac{2}{3}, u\right)$	Cl $\left(\frac{2}{3}, \frac{1}{3}, -u\right)$

Table 6.7: Structural parameters of β-$MgCl_2$.

By running *ab initio* simulations and fitting the dipoles and forces on this structure, we hoped to gain some insight into whether the slightly poorer fits in $Mg(OH)_2$ were due to the molecular model or whether they were due to the interactions in layered structures being intrinsically more difficult to reproduce using our classical potential model. For the purposes of running *ab initio* calculations and fitting potentials for $MgCl_2$, it was best to use the orthorhombic unit cell, principally because the cut-off radius beyond which we do not calculate short-range Fumi-Tosi interactions in our MD code is restricted to half the minimum simulation cell width, and this value is reduced for non-orthorhombic cells. We translated the hexagonal cell to the orthorhombic the way shown in Figure 6.17, giving the new cell parameters in Table 6.8.

We generated configurations of the crystal, using three to perform *ab initio* CASTEP calculations on, each containing 72 atoms. On fitting a RIM potential

Cell lengths/bohr	$a = 6.881$	$b = 11.917$	$c = 11.200$
Atomic Coordinates	Mg (0,0,0)	Cl $\left(0, \frac{1}{3}, u\right)$	Cl $\left(\frac{1}{2}, \frac{1}{6}, -u\right)$
	Mg $\left(\frac{1}{2}, \frac{1}{2}, 0\right)$	Cl $\left(\frac{1}{2}, \frac{5}{6}, -u\right)$	Cl $\left(0, \frac{2}{3}, -u\right)$

Table 6.8: Structural parameters of β-$MgCl_2$, unit cell doubled and translated to orthorhombic symmetry. u=0.23.

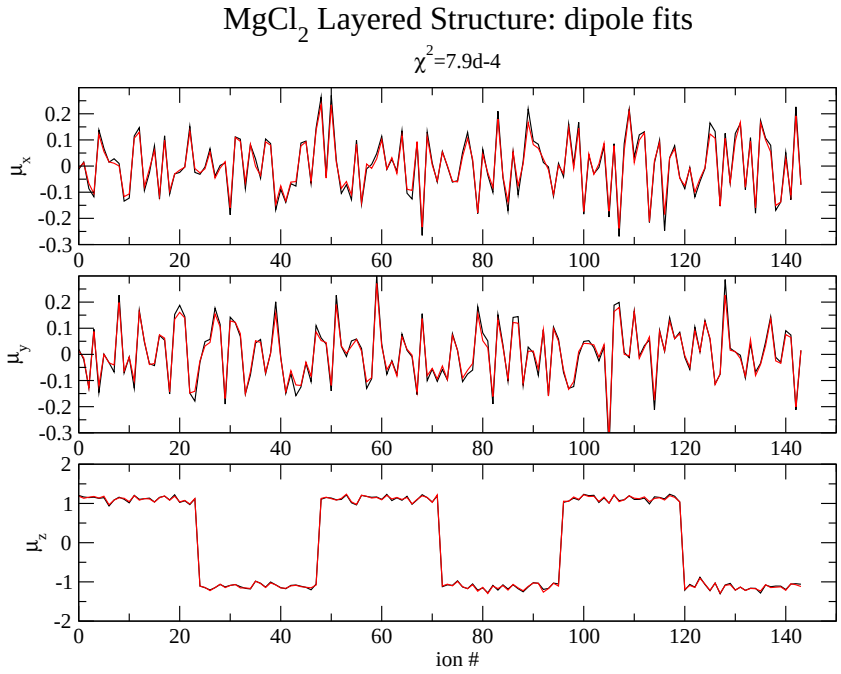

Figure 6.21: The *ab initio* and fitted dipoles (given in a.u.) on the chloride ions in the layered β-form of $MgCl_2$.

model, we obtained a χ^2 of 1.822, the quality of which is in the same regime as the RIM $Mg(OH)_2$ fit χ^2 of 2.34, whereas the $NaF/AlF_3/Na_3AlF_6$ RIM fits were much better with χ^2 values in the range $0.08 \leq \chi^2 \leq 0.275$. This immediately suggested the layered structure was mostly responsible.

Going on to fit the dipole polarization parameters for these $MgCl_2$ configurations, the fit quality we achieved was similarly excellent to the molecular dipole fit quality, as shown in Figure 6.21. Once again we see a marked pattern in the dipoles along the layer axis c, where the anions on either side of a layer have approximately opposing dipole moments as their environments are mirror images or one another, each lying between what can approximately be thought of as a plane of Cl^- and a plane of

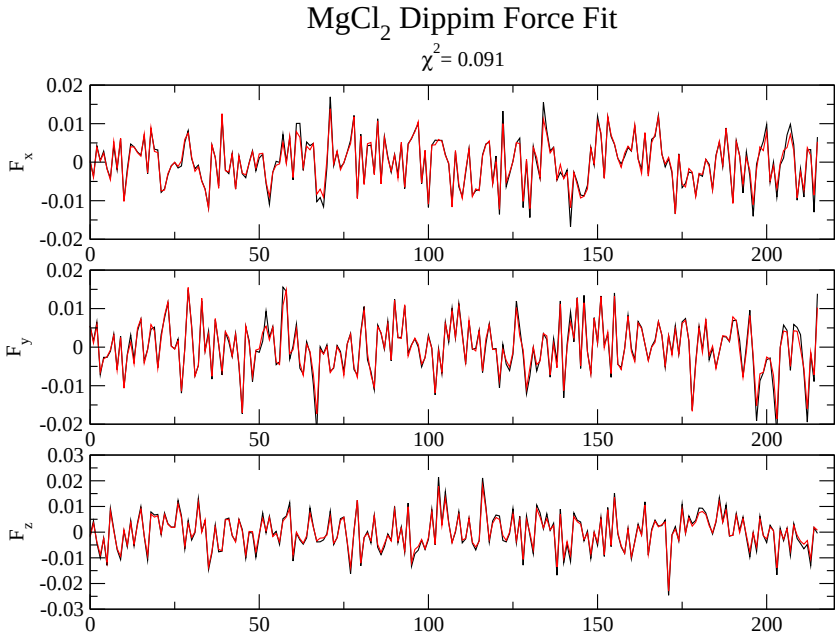

Figure 6.22: Comparison of *ab initio* and fitted forces (given in a.u.) from a dipolar potential for $MgCl_2$.

Mg^{2+} ions, inducing dipoles of reverse sign. Although the magnitude of the z or c-axis component of the dipoles is larger than the other two, we see the size of the fluctuations in all three components are similar, which we can ascribe to the effect of thermal motion.

We then held these optimized polarization parameters fixed while fitting the short-range parameters for a dipolar potential to CASTEP's forces on the ions. For this we achieved a good value of χ^2, of 0.091: the *ab initio* and fitted forces are compared in Figure 6.22. This value, like the value from the RIM fit, was similar to the equivalent $Mg(OH)_2$ fit and though very acceptable, still significantly larger than the corresponding potential fits for the typically ionic structured materials $NaF/AlF_3/Na_3AlF_6$. These results all indicate that it is the layered structure of $Mg(OH)_2$ and similar compounds which prevents us from obtaining the kind of fit-qualities we saw for our work on cryolite (and that it is not the responsibility of the *molecular* aspect of our new model).

On testing this $MgCl_2$ potential to see how well it reproduced the accepted β

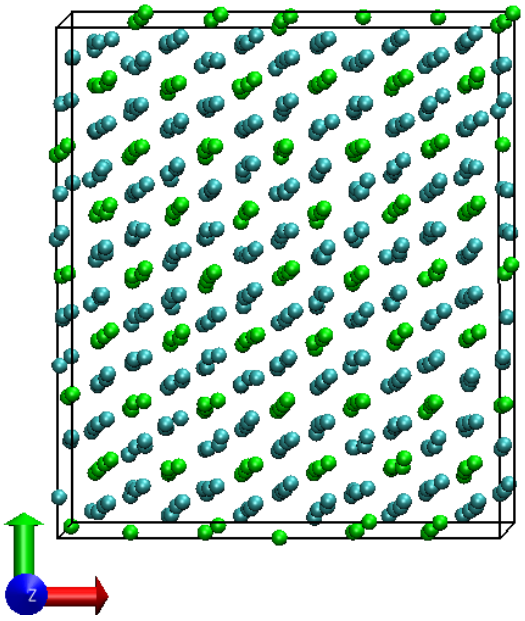

Figure 6.23: View along the c axis of $MgCl_2$, a snapshot from our test simulations using the fitted potential, showing the retention of the hexagonal structure.

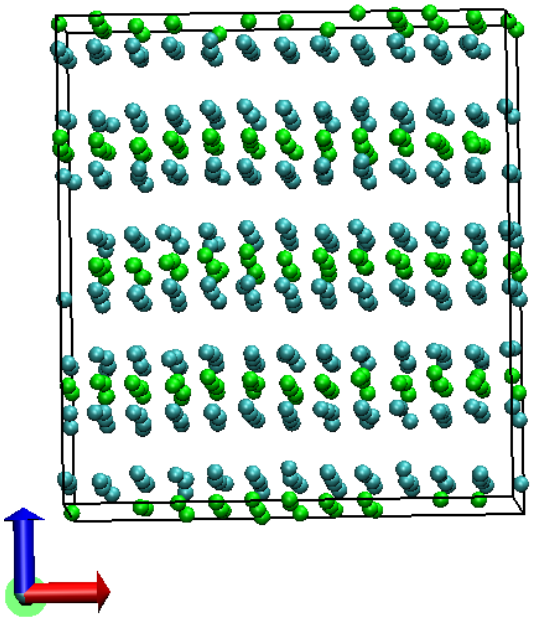

Figure 6.24: 'Side view' (along the a axis) of $MgCl_2$, showing how the layered structure has been retained. Key: Mg=green, Cl=blue.

structure, we found it to be very successful, as was the $Mg(OH)_2$ potential after the first round of fitting. We ran NPT simulations at 300 K, and discovered that the simulation cell had no tendency to change shape or cell angles for long after it had been observed to have equilibrated, the RDFs and structure factors still characteristic of the perfect crystal. We would not expect the potential to accurately replicate the cell dimensions at this early stage, this almost always requires further tuning as described in the next subsection. Snapshots from a movie of the thermally distorted hexagonal layered structure are shown in Figures 6.23-6.24. So despite the fit qualities of layered materials being less good than for atomic, the fitting process still produces potentials which predict the basic structures correctly.

6.6 Testing the Dipolar-Polarizable Potential and Refining the Dispersion Parameters

As the final step in the process of refining a dipolar-polarizable potential for $Mg(OH)_2$, we needed to test that it replicated the crystal structure, and furthermore how well

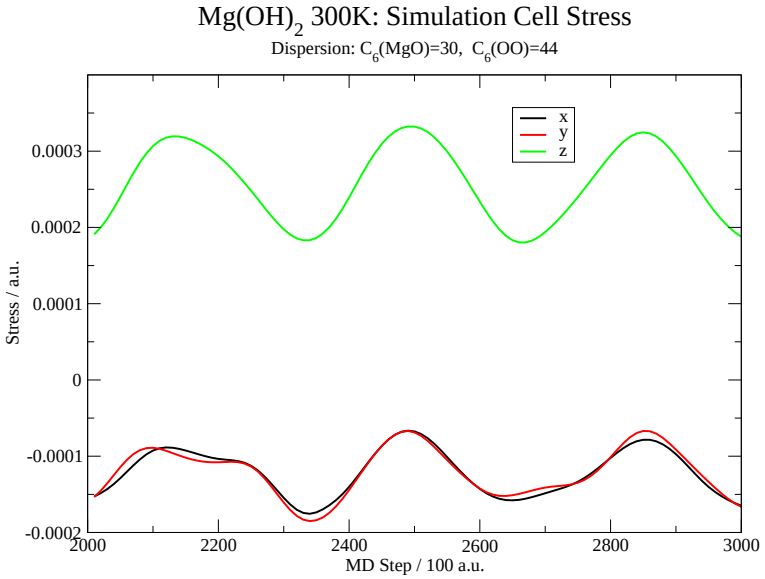

Figure 6.25: The diagonal components of the simulation cell's stress tensor, showing the stress throughout a simulation along the three cell axes, $x = a$, $y = b$, $z = c$.

it reproduced the correct cell volume and dimensions. Like the dipolar potential from the first round of fitting, we found it had no trouble maintaining the basic structure over long simulations. However the cell dimensions it predicted were not in such good accordance with experimental measurements.

Running simulations at constant volume (NVE), at a temperature of 300 K, we plotted out the diagonal components of the stress tensor corresponding to the simulation cell's three axes, using the newly-fit dipolar potential. These are shown in Figure 6.25. The simulation was run using the experimental cell dimensions for 300 K [78], and the signs and magnitudes of the average values of the oscillating stress components indicate to what extent the cell wishes to contract or expand under the fitted interaction potential along each axis. As we see, under the fitted potential the cell wished to elongate along the c-axis and contract in the xy-plane, tending to increase the layer spacing. This layer spacing is dominated by the non-ionic interactions which are the most challenging for us to replicate with our extended ionic model. It has been shown by several previous studies in our research group (including [86], [36]) that dispersion plays a large role in determining the inter-

layer spacing in such materials, and by modifying the dispersion parameters 'post-fitting' the potential can be fine tuned beyond reproducing the basic structure to reproducing the dimensions of a crystal accurately. We do not usually 'fit' the dispersion parameters: we know that density functional theory does not reproduce the r^{-6} dependence of the contribution of dispersion to inter-atomic interactions very well, so we cannot hope to improve the fits significantly by tweaking the dispersion parameters, and any improvements we did see would not be very meaningful since the data we fit to would not necessarily be accurate on the dispersion front.

In our fitting so far we had held the dispersion parameters fixed: the values we used were taken from a tried and tested MgO potential, and only finite values of the dispersion between the pairs O-O, Mg-O and Mg-Mg were included. The values of these C_6 and C_8 parameters are given in Table 6.9. So, we tried varying each of the C_6 parameters in turn to optimize the interlayer spacing in $Mg(OH)_2$, where the C_6 term has a more significant contribution to the energy than the C_8.

	O-O	O-Mg	Mg-Mg
C_6	44.4	30.0	5.8
C_8	853.0	300.0	15.0

Table 6.9: The finite dispersion parameters we held fixed in the fitting of the $Mg(OH)_2$ potential to this point, in atomic units.

We saw two potential ways of dealing with the dispersion. One was to refit the short-range potential potential parameters for each of a series of fixed C_6 values, and looking to see which reproduced the cell dimensions most accurately. The second was to use the potential we had fitted using the reasonable approximations to the dispersion parameter values that we had made, then adjust the dispersion parameters afterwards to optimize the dimensions. It is this latter method which necessarily was used in older work involving the fine tuning of empirical potentials, before *ab initio* information could be obtained for cells of a useful size and before the fitting process had been developed. In one respect, fitting a new potential for each combination of fixed dispersion parameters would seem the best option:

it appears more rigorous in that the short range parameters are optimized so as to match the fitted forces owing to the sum total of interactions in the system as we model them, including dispersion contributions. On the other hand, we know the dispersion contribution to the forces is relatively small compared to those from Coulomb and short range effects, and we know that dispersion interactions are not well-reproduced in our CASTEP simulations, to the extent that they can almost be considered to have been omitted. As it is not clear which method is best to use in practice, we tried both.

Starting by looking at the magnesium-oxygen dispersion, we thought there was a reasonable possibility that by increasing the corresponding C_6 value, we would increase the attractive forces throughout the cell and therefore between layers, correcting the inter-layer spacing which has a tendency to increase above the experimental value with the 'default' combination of C_{disp} values.

Attempting method one first, we tried fitting a different short-range potential for each set of dispersion parameters, with C_6 values of 30, 50, 70 and 90 atomic units. The first feature we noted was that as C_6 was raised, the fit quality worsened a little, χ^2 reaching 0.26 at $C_6 = 90$. On running simulations with these fitted potentials and monitoring the cell stress, we found there were negligible differences in the stress components between any of the potentials. It seemed plausible that the short-range parameters were changing in such a way as to compensate for the shifting dispersion parameters, resulting in no net effect on the cell stress. So it seemed that refitting the potentials for different dispersion parameters was not such an effective method for optimizing the cell dimensions of this and possibly other materials.

Proceeding to try the second method, we ran a series of simulations at the same intervals over a range of Mg-O C_6 values, from the default value of 30 upwards, using the same set of short range parameters for each, which were those we obtained from our best dipolar-polarizable potential fit. The simulations were once again run at the experimental cell volume, and the diagonal cell stresses from these simulations

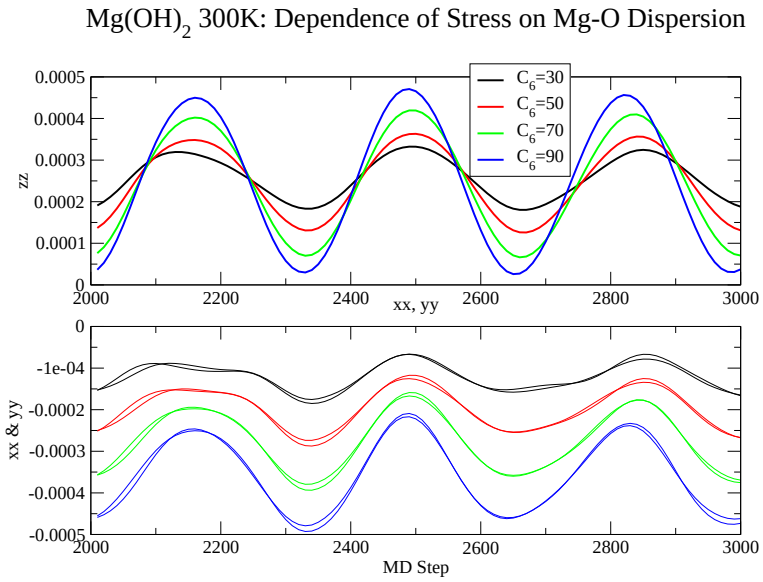

Figure 6.26: Diagonal stress tensor components (given in a.u.) of an $Mg(OH)_2$ simulation cell over a range of Mg-O C_6 dispersion values, where the short range parameters were held constant.

are shown in Figure 6.26.

We saw that now the value of the stress along the c or z axis did decrease as we raised C_6^{MgO}, indicating the natural cell length under these potentials decreased towards the experimental value as the Mg-O dispersion interaction increased. However, the cell dimensions decreased fairly isotropically, so though the c dimension improved, the a and b dimensions became worse and contracted further as we raised the Mg-O dispersion. The stress also oscillated with a greater amplitude as the C_6^{MgO} was raised, to the extent that the simulations became unstable at values of C_6=70 upwards. Therefore it did not seem that adjusting this particular dispersion interaction (between Mg and O) was a particularly effective means of improving the cell dimensions.

Next, we tried repeating the second method, but adjusting the oxygen-hydrogen dispersion interaction instead, which was not included at all in the originally fit dipolar potential. For this, we worked from zero dispersion upwards, until $C_6 = 10$, the magnitude of the dispersion involving hydrogen being smaller than with magnesium because of their respective number of electrons. We kept the $C_{6,8}$ parameters

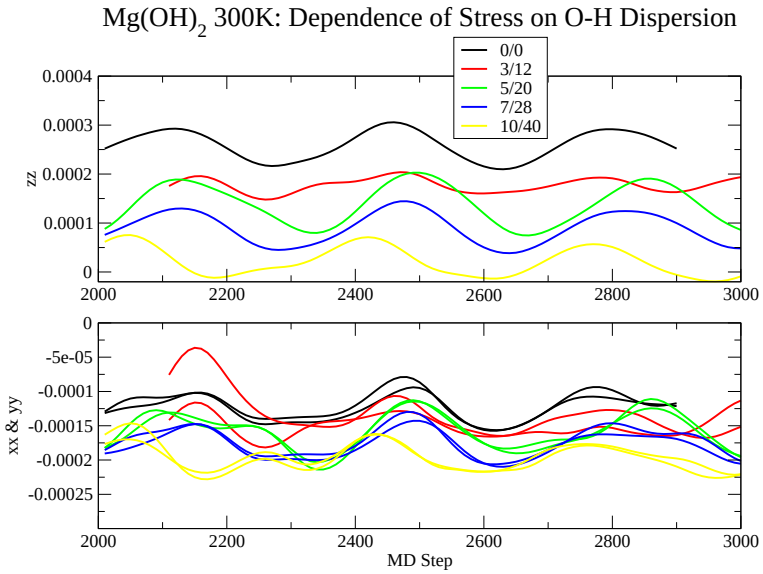

Figure 6.27: Diagonal stress tensor components of an $Mg(OH)_2$ simulation cell (given in a.u.) over a range of O-H C_6 dispersion values, where the short range parameters were held constant.

in the 1:4 ratio they have typically fallen in the region of in much empirical potential development our group has carried out in the past. We modified our MD code to ensure that the O-H dispersion interactions were intermolecular only, so as to be 'physical'. The diagonal components of the stress tensor representing each of the cell axes are shown for each simulation in Figure 6.27. This time we found the method to be of much more use: while the magnitude of the stress and hence the tendency to expand along the z axis decreases, the tendency to contract in the xy plane remains fairly constant: the effect of O-H dispersion on the structure is anisotropic. For the layers - which are formed by sheets of oxygen atoms and are separated only by hydrogen atoms - it can be surmised with the aid of Figure 6.15 that there would be a particular tendency for O-H dispersion to work along the layer axis.

To verify that there were no fundamental changes made to the structure through raising the dispersion, in addition to making movies of the simulations, we also plotted out the radial distribution functions of each atom species with respect to oxygen, which are shown in Figure 6.28, r_{ij} starting just beyond the fixed O-H bond length. It can easily be seen that the basic structure does not change, but

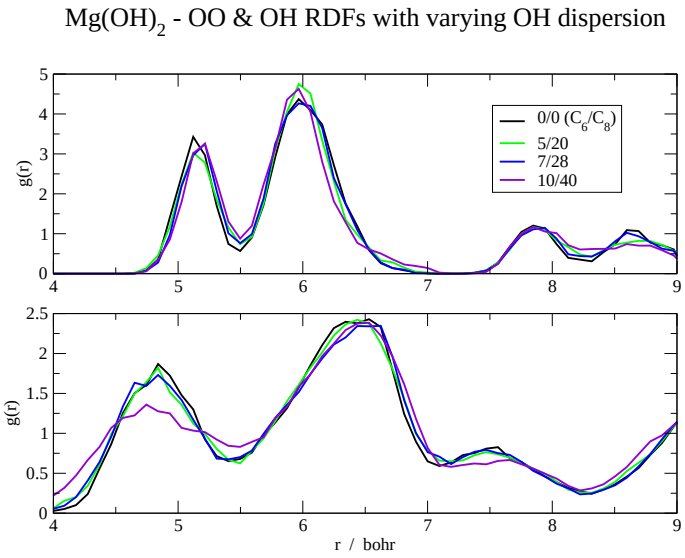

Figure 6.28: Radial distribution functions with respect to the oxygen atoms in $Mg(OH)_2$ using different sets of dispersion parameters. The upper graph is g(r) for O-O, the lower O-H.

also that the inter-atomic spacing does not visibly change despite the introduction of anisotropic dispersion to the system. So the method worked to some extent in gluing the layers together with the choice of modifiable dispersion parameters being Mg-O, though the actual C_n values would have to be increased somewhat further to attain the correct cell dimensions. This should not pose the same problem as it did with increasing the Mg-O dispersion, as the stress oscillation and simulation stability does not appear to change, possibly because of the smaller changes to C_6 required to have a given effect on the stress.

In short summary, we see that simply by introducing dipolar polarization to a potential even at an atomic level we achieve a great improvement in our force-fit quality, as we did in the cryolite work. We found that we can achieve force fits using the molecular ion method of almost as good a quality as the atomic force fits earlier, although it takes more iterations of the fitting process, and that much of the discrepancy is due to the layered structure of $Mg(OH)_2$ rather than the molecular nature of the anions and our method with respect to the molecules. Finally we discovered that by identifying the appropriate set of dispersion parameters, we can further optimize

the structural accuracy of a potential by modifying those parameters *after* fitting the short-range parameters.

6.7 Extending the Potential Model for Diatomics to Aspherical Ions

6.7.1 Adapting the Aspherical Model to Molecular Ions

Given the anisotropic environment within layered structures such as $Mg(OH)_2$, as well as the more diffuse electron distribution of molecular as compared to atomic ions, we thought it well worth investigating whether allowing shape deformation to occur under the influence of the surrounding ions would improve our model's representation of the system. As with the atomic cryolite simulations, we tried using two levels of distortion to describe the effects - dipolar and quadrupolar shape distortions, the development for both of which are described in this chapter.

However, in a similar way that we adapted the polarization model from being atomic to molecular, we attempted to modify our shape distortion model, which would normally be applied to the anions 'O^{2-}', from being atomic to molecular. From the atomic perspective it is clearly the bonded H atom which will have the dominant effect on the shape of the oxygen, and from the molecular perspective, the principle axis of any dipolar or quadrupolar shape distortions must coincide with the bond axis. Therefore in our molecular ion model we fix our axes of deformation to lie along the bond axes. The extent to which a molecule can be distorted is incorporated as a factor λ for the dipolar and quadrupolar distortion terms, so we have λ_d and λ_q respectively. As a starting point for these we would use values which give terms of similar magnitude to atomic distortion terms, but which we would then be able to refine in the fitting process.

The energy terms arising from this model are given in Equation 6.3, where the terms in brackets are the standard Fumi-Tosi short-range repulsion, the dipolar

distortion and the quadrupolar distortion respectively.

$$U = \sum_{pairs\ O,j} B_{ij} e^{-\alpha_{ij}\left(\mathbf{r}_{ij} - \lambda_d \mathbf{S}_{\alpha}^{ij} \boldsymbol{\epsilon}_{\alpha} - \lambda_q \mathbf{S}_{\alpha\beta}^{ij} \boldsymbol{\kappa}_{\alpha\beta}\right)} \tag{6.3}$$

These can be compared to the energy terms associated with the atomic distortion model given in Equation 6.4, where $\boldsymbol{\epsilon}_{\alpha}$ and $\boldsymbol{\kappa}_{\alpha\beta}$ become a unit vector and tensor respectively with fixed axes coinciding with the bond axes, and with magnitudes λ to be determined through fitting the forces. $\mathbf{S}_{\alpha}^{ij}$ and $\mathbf{S}_{\alpha\beta}^{ij}$ are tensors representing the interparticle separations.

$$U = \sum_{pairs\ O,j} B_{ij} e^{-\alpha_{ij}\left(\mathbf{r}_{ij} - \mathbf{S}_{\alpha}^{ij} \boldsymbol{\epsilon}_{\alpha} - \mathbf{S}_{\alpha\beta}^{ij} \boldsymbol{\kappa}_{\alpha\beta}\right)} \tag{6.4}$$

Unlike in the atomic model, we now determine a single value for each of λ_d and λ_k with the reasoning that this represents a tendency towards a shift of the ion-centre (which the diagram in Figure 6.29 helps to explain), and that the molecular shape is predominantly determined by intramolecular effects, where all the bond lengths are at a single fixed value.

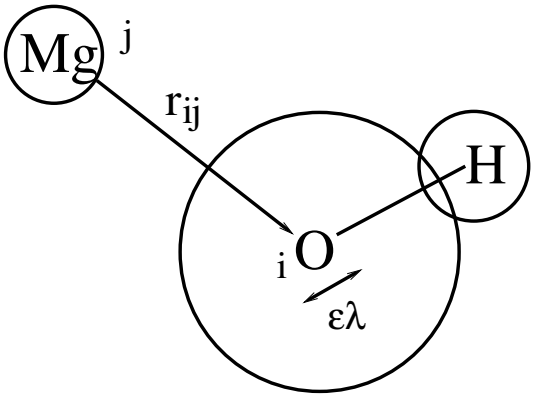

Figure 6.29: The molecular shape-distortion model, applied to diatomic OH^-.

So, to implement this model in our MD program, we needed to determine the expressions for the energies and forces, in terms of the inter-particle separations and the parameters in our interaction potential. For the energies, Equation 6.3 can be rewritten as Equation 6.5, where the index 'H' refers to the hydrogen directly bonded to the oxygen atom in the sum over all pairs with each oxygen.

$$U = \sum_{pairs\ O,j} B_{ij} e^{-\alpha_{ij}\left(|\mathbf{r}_O-\mathbf{r}_j|-\lambda_d\frac{(\mathbf{r}_O-\mathbf{r}_j).(\mathbf{r}_O-\mathbf{r}_H)}{r_{OH}|\mathbf{r}_O-\mathbf{r}_j|}-\lambda_q\left(3\frac{(\mathbf{r}_O-\mathbf{r}_j)^2_{\alpha\beta}}{|\mathbf{r}_O-\mathbf{r}_j|^2}-\delta_{\alpha\beta}\right).\left(3\frac{(\mathbf{r}_O-\mathbf{r}_H)^2_{\alpha\beta}}{|\mathbf{r}_O-\mathbf{r}_H|^2}-\delta_{\alpha\beta}\right)\right)} \tag{6.5}$$

We differentiated this to give the expressions for the forces on each atom due to this three-body (O,H,'j') deformation interaction. Since there are three separate terms in the exponent, one for each physical effect, when differentiated we can write the result as three separate terms contributing to the force on any atom (Equation 6.7).

$$U = B.U(Fumi\ Tosi).U(dipolar).U(quadrupolar) \tag{6.6}$$

$$\mathbf{F}^i = \mathbf{F}^i(Fumi\ Tosi) + \mathbf{F}^i(dipolar) + \mathbf{F}^i(quadrupolar) \tag{6.7}$$

The x-components of the forces on atom 'j' are given in Equations 6.8 to 6.12, the y and z components being symmetrically related. The force is broken down into contributions from the Fumi-Tosi, dipolar and quadrupolar distortions; d stands for the (fixed) O-H bond length.

$$F_x^j(Fumi\ Tosi) = -B\frac{\partial U_{FT}}{\partial x_j} = -B\alpha e^{|\mathbf{r}_O-\mathbf{r}_j|}\left(\frac{x_O-x_j}{r_O-r_j}\right) \tag{6.8}$$

$$F_x^H(Fumi\ Tosi) = 0 \tag{6.9}$$

$$F_x^O = -(F_x^j + F_x^H) \tag{6.10}$$

There is no Fumi-Tosi contribution to the force on the hydrogen atoms from their bonded neighbouring oxygen atoms: these terms were omitted from the potential as described when outlining the form of the molecular ion potential in section 5.2. The force on an oxygen atom arising from any of these three physical effects can always be given by the negative of the sum of the forces on the hydrogen and atom 'j' in any triplet, arising from the same effect (Equation 6.10).

$$F_x^j(dipolar) = -B\frac{\partial U_{dip}}{\partial x_j} = -\lambda_d B\alpha e^{|\mathbf{r}_O-\mathbf{r}_j|}\left(-\frac{\epsilon_x}{|\mathbf{r}_O-\mathbf{r}_j|} + (x_O-x_j)\frac{\boldsymbol{\epsilon}.(\mathbf{r}_O-\mathbf{r}_j)}{|\mathbf{r}_O-\mathbf{r}_j|^3}\right) \tag{6.11}$$

$$F_x^j(quadrupolar) = -B\frac{\partial U_{quad}}{\partial x_j} = -\lambda_q B\alpha e^{|\mathbf{r}_O - \mathbf{r}_j|}(\mathbf{\Omega}) \tag{6.12}$$

$$\mathbf{\Omega} = 6S_{xx}\left(-\frac{x_{Oj}}{|\mathbf{r}_{Oj}|^2} + \frac{x_{Oj}^3}{|\mathbf{r}_{Oj}|^4}\right) + 6S_{xy}\left(-\frac{y_{Oj}}{|\mathbf{r}_{Oj}|^2} + \frac{2x_{Oj}^2 y_{Oj}}{|\mathbf{r}_{Oj}|^4}\right) + 12S_{yz}\left(\frac{x_{Oj}y_{Oj}z_{Oj}}{|\mathbf{r}_{Oj}|^4}\right) + \tag{6.13}$$
$$+6S_{xz}\left(-\frac{z_{Oj}}{|\mathbf{r}_{Oj}|^2} + \frac{2x_{Oj}^2 z_{Oj}}{|\mathbf{r}_{Oj}|^4}\right) + 6S_{yy}\left(\frac{x_{Oj}y_{Oj}^2}{|\mathbf{r}_{Oj}|^4}\right) + 6S_{zz}\left(\frac{x_{Oj}z_{Oj}^2}{|\mathbf{r}_{Oj}|^4}\right).$$

The parameters denoted $\boldsymbol{\epsilon}$ and $\boldsymbol{\kappa}$ are the vector and tensor mentioned earlier in this section, with the principle axes directed along the O-H bonds, and the separation tensor $S_{\alpha\beta}$ associated with the quadrupolar distortions can be written as $\left(3\frac{|\mathbf{r}_{OH}|_{\alpha\beta}^2}{d^2} - \delta_{\alpha\beta}\right)$ but is kept in its succinct form for brevity; $\mathbf{r}_O - \mathbf{r}_j$ etc... are abbreviated to $\mathbf{r}_{Oj}$.

Having incorporated these Equations into the energy routines in our code, we went on to test that we could run stable simulations with it, and verified that it conserved energy. We found this to be the case, provided that $\boldsymbol{\epsilon} \leq 0$: we assumed from this that the situation was unphysical when this condition was not met.

6.7.2 Fitting a Potential for $Mg(OH)_2$ Incorporating Dipolar and Quadrupolar Shape Distortion

Fixing the polarization parameters and partial charges to the best values from the previous section, given in Table 6.3, and first using the same three near-liquid configurations used in the fits in the previous sections, we went on to fit the short-range parameters with the dipolar distortion model, at intervals over a wide range of λ_d (or $|\boldsymbol{\epsilon}|$). The results, in terms of the fit quality χ^2, and the effects on the values of the Fumi Tosi parameters B_{OH}, B_{OMg}, a_{OH} and a_{OMg}, are shown in Figure 6.30. What we saw was an optimum value of λ_d of -0.09, lying at the base of a fairly shallow curve in χ^2 in this range of λ_d where any point in the range $-0.2 \leq \lambda_d \leq 0.0$ produced a value of χ^2 close to 0.9. (The fit with $\boldsymbol{\epsilon} = -0.65$ was anomalously good for that region of the curve, where two parameters can be seen to have found

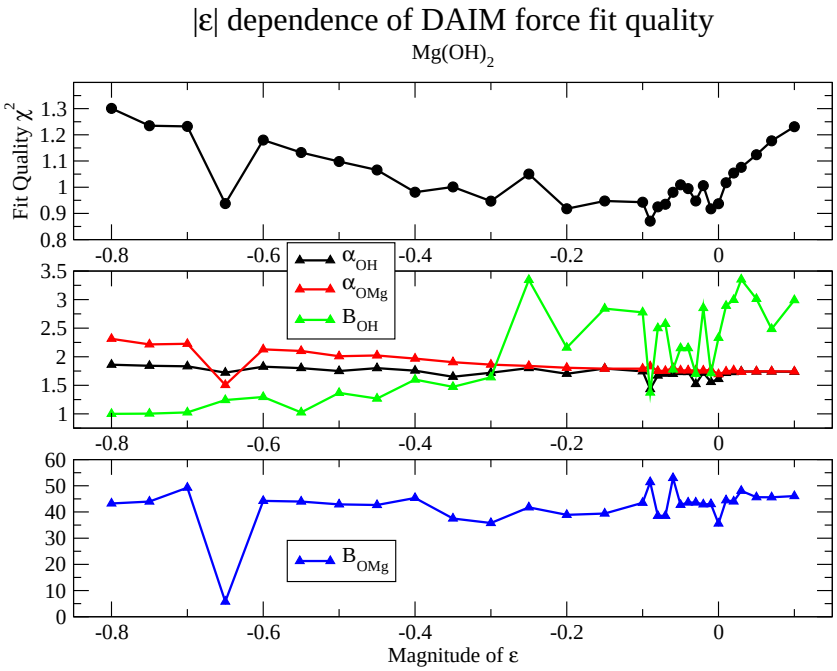

Figure 6.30: The results of fitting potentials at the molecular dipolar distortion level, over a range of values of distortion constant λ_d (using near-liquid configurations). Potential parameters are given in atomic units.

very different places on the energy landscape. This effect was not reproduced when we attempted to restrict the same parameters to their different regions on fitting at other values of $\boldsymbol{\epsilon}$.) The best value of χ^2 was 0.87, an improvement of 6% on the best potential using a polarizable molecular model without ion deformation. Though fairly small, this is a similar degree of improvement to that made on adding dipolar distortion to the atomic ion model in fitting a potential for cryolite. Such a small improvement means it would probably not be worth employing this model for this material at the extra computational cost for lengthly simulations, but the similarity in improvement on going from fixed-shape to deformable ions in both this molecular model and the tried and tested atomic model tells us firstly that our implementation is working, and secondly that improvement in fit quality is possible. Although not significant for this material, it could well be for another where ionic shape-deformation is a more significant characteristic, and a larger improvement in force-fit quality is highly feasible.

In addition to looking at the effect of the dipolar deformation constant λ_d on the force-fit quality, we also looked at the effect it had on the Fumi Tosi parameters. This was as much to gain insight into the fitting program and how to best use it to understand the interactions in the material itself, a necessity if we wish to optimize our likelihood of discovering the true minimum on the potential energy surface with respect to the values of our parameters. We see that as the value of λ_d increases towards its optimum value, most notably the value of B_{OH} (a parameter approximately reflecting changes in the intermolecular O-H cross sectional radius) increases before forming a noisy plateau. This behaviour of B_{OH} can be interpreted as occurring to compensate for us forcing the deformation constant towards what we see as its best value: so although we are not observing an actual deformation effect, such a trend is very useful in order to pinpoint the optimum value of a new parameter we introduce. Similar, though less marked effects, can be seen in the behaviour of the three other Fumi Tosi parameters shown as the value of λ_d is changed.

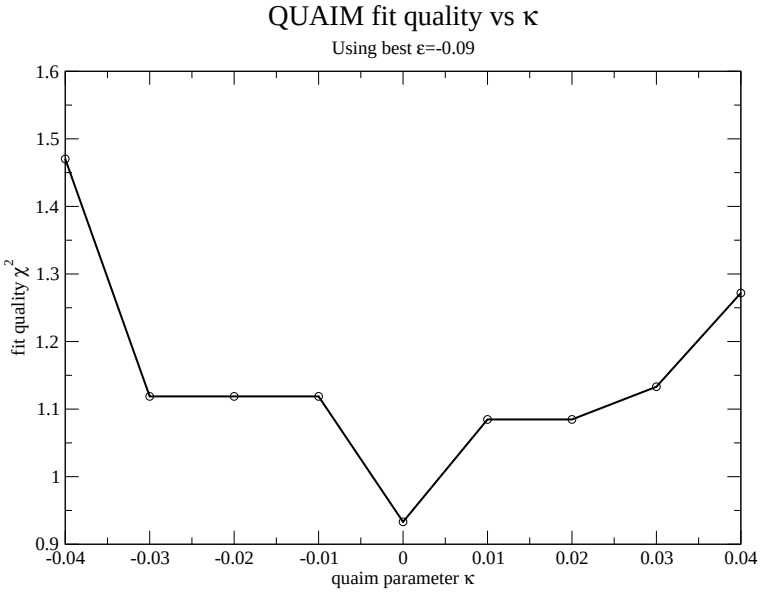

Figure 6.31: Fit quality as a function of λ_q, for a quadrupolar shape-distortion potential (using near-liquid configurations).

In the next step we went on to perform a similar process with the quadrupolar distortion constant λ_q, holding the polarization and short range parameters at their

optimum values as well as λ_d, where the dipolar and quadrupolar distortion constants should be independent of one another, with the two having different symmetry. However this did not meet with the same success as dipolar distortions, as seen in Figure 6.31. χ^2 reached a minimum at $\lambda_q = 0$, the same value as reached by the best non-deformable polarizable potential upon which the fixed parameters here were based, but there was no improvement on moving to finite λ_q, rather the fit quality got slightly worse without there being any clear reason for this. We could postulate that there was something unphysical about extending this model to molecular shape distortions the way we did, or our particular function was not a good choice, but we were not in fact sure why this proved unsuccessful.

At this stage we had completed the second round of fitting of the dipolar potential in the previous section, and thought it could prove insightful to attempt to fit a dipolar-shape-deformation potential using the same crystalline configurations generated by the dipolar potential from the first round of fitting. The motivation was to both compare the pattern in the optimum value of λ_d with that from the near-liquid configurations, and also to compare the degrees of improvement in χ^2 on iterating the fitting process with the two forms of potential.

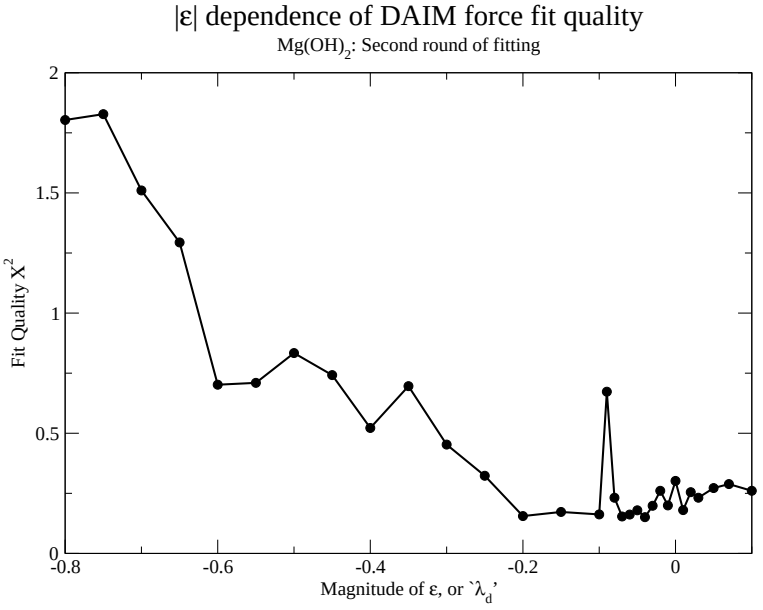

Figure 6.32: Fit quality of DAIM potentials for $Mg(OH)_2$ as a function of λ_d

Once again we saw that the minimum in χ^2 lay in the region $-0.2 \geq \lambda_d \geq 0$, as shown in Figure 6.32, so it would seem that the optimum value of the dipolar distortion constant and hence the tendency of the ions to be distorted is not particularly effected by whether the state is solid or liquid. As we supposed in our reasoning for assigning all the molecules a single distortion constant, it is the in*tra*molecular bonding which predominantly defines the ability to be distorted, where all the bond lengths are fixed, and so it is not surprising that we see this consistency in λ_d from our fitting results.

As we saw in comparing the first round of DAIM-potential fitting results with those from the first round of non-deformable dipolar potential fitting, there was a small improvement in the fit quality χ^2 for a certain range of λ_d. For the -0.2 to 0.0 interval in λ_d, χ^2 lies between 0.15 and 0.2 for the most part, which are verging on 'good' fits. The best value 0.153 lay at $\lambda_d = -0.04$, and was an improvement of 16% on the corresponding non-deformable dipolar potential fit, somewhat better than the 6% improvement between the equivalent two first-round fits. It is conceivable that on choosing to fit the forces within more structurally accurate configurations such as in our second iteration, the more subtle effects of atomic/molecular distortion come into play as they should, having an influence on the *ab initio* forces which can be picked up through the fitting process and translated into the final potential. So, as with the cryolite simulations, the extension to the potential model which gave the greatest improvement in the description of our systems containing molecular ions was allowing the formation of dipoles on the molecules, and allowing ionic shape deformation had a relatively small (though not insignificant) effect on the fit quality.

6.8 Conclusions to $Mg(OH)_2$ Potential Fitting

In the process of refining our potential model for molecular ions, we found the rigid molecular geometry model to produce fits of far superior quality. By omitting an

intramolecular potential and fitting to purely intermolecular forces, by considering the charge distribution within the molecular ions, and by incorporating a molecular polarization model into the fitting process, we were able to obtain very reasonable fit qualities. While the standard of fit at this stage was not as good as that obtained for cryolite, the study of an atomic system ($MgCl_2$) with a very similar structure where we when through the same fitting process, suggested that it was in fact the layered nature of the system rather than its molecular nature that proved the challenging factor. On iterating the fitting process, whereby we generated new $Mg(OH)_2$ configurations for fitting using the first-fit potential as input in place of an empirical potential, the fit quality improved very much to the point where it could be described as excellent, in the same regime as the NaF/AlF_3 fits. We were able to obtain dispersion parameters for the potential through varying their values by hand to optimize the cell lengths. Allowing the molecular ions to form dipolar shape distortions, there was a small improvement in fit quality, but the most significant extension to the model was, once again, the introduction of polarization, as was the case in the cryolite fitting process.

In conclusion, although it required an extra iteration of the fitting process, and despite the lack of precedent for expecting the molecular ion fitting procedure to work well, we found this work on the hydroxide ion to be very successful, providing an excellent foundation for further work in this field.

Chapter 7

Extension to the Triatomic UO_2^{2+}

7.1 *Ab initio* Modeling of the Uranyl Compound

The next obvious step in developing potentials for molecular ions was to extend the method we had refined so far to another compound, with another molecular geometry. We chose the compound $Cs_4U_2O_4Cl_8$ containing the linear triatomic molecular ion UO_2^{2+} as an interesting and challenging candidate. The structure is illustrated in Figure 7.1. Further to introducing the interaction model for the UO_2^{2+} molecular ion and describing how its molecular geometry was implemented in our simulation code in section 5.2, here we go on to study the material using *ab initio* CASTEP calculations and attempt to fit RIM and dipolar-polarizable potentials for it by adapting the method we developed for diatomics.

Such uranium compounds are of interest in nuclear fuel reprocessing: understanding and being able to model them is particularly important in the light of the need to deal with nuclear waste as the industry grows, and simulation is a particularly useful tool for studying hazardous and expensive compounds like this. The uranyl ion is exceptionally thermodynamically stable, the U=O double bonds undergoing few chemical reactions. One recent exception to the unreactivity has been found by using a potassium complex [87]. The stability of the uranyl ion is thought to be due to a 'unique confluence of electronic effects that lead to the formation of strong, unreactive U=O bonds' [88]. Uranium is a very unusual case where relativistic effects lead to the non-valence $6p$ orbitals lying at a relatively high energy for a

core state, and to thereby potentially interact with the valence $5f$ orbital generating a set of hybrid orbitals of a certain symmetry and at an intermediate energy which is appropriate for a strong linear bond with two small first row elements such as oxygen.

Uranium compounds are challenging from the point of view of simulation for a number of reasons arising from their electronic structure and bonding. The high formal charge of the uranium (usually +5 or +6) is the cause of stability problems when used in classical simulations which use a strictly ionic model. However an ionic model is not necessarily an accurate one for highly charged polarizing Actinides, which are known to have a greater tendency for covalency from a molecular orbital point of view, yet they are far from fully covalent. There was also an issue for us with modeling this compound in *ab initio* simulations, there being no available, reliable and well-tested uranium pseudopoential to work with, so we had to take the process back one step and develop our own.

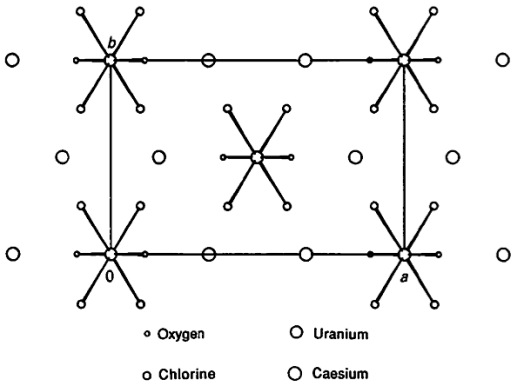

Fig. 1. The *c*-axis projection of the structure of $Cs_2UO_2Cl_4$.

Figure 7.1: The structure of $Cs_2UO_2Cl_4$ [75]. The octahedral units are UO_2Cl_4 species, with the shorter axial bonds connecting uranium and oxygen. The remaining spheres represent the atomic caesium ions.

Using the code developed in section 5.2 we were able to generate $Cs_4U_2O_4Cl_8$ configurations, using the empirical RIM potential with springs to represent the intramolecular U-O bonding. The largest computationally tractable simulation cell based on the number of pseudized electrons was $1\times2\times2$ unit cells in dimension,

containing 72 ions including eight UO_2^{2+} molecular units, and had a minimum cross section of 21 bohr. A diagram of the unit cell is shown in Figure 7.1.

The program 'opium' [89] is considered a reliable way of generating good pseudopotentials for CASTEP, and has been used successfully in work by members of our research group in recent years [36]. So as to have a consistent set of norm-conserving pseudopotentials, we used opium to generate pseudopotentials for each of the four species in $Cs_4U_2O_4Cl_8$. For each one we input a plane wave cut-off equivalent to 1000 eV, quite a stringently high value as has been used in all this work so far, and the recommended 10 bessel functions to model the pseudized wavefunction on. The pseudized electrons and the cut-off distances after which we required the real and pseudized wavefunctions to match, for each species, are given in Table 7.1.

O (n,l,k) [He]	2,0,0	2,1,0			
occupancy	2.00	2.00			
cut-off (bohr)	1.40	1.45			
Cl (n,l,k) [Ne]	3,0,0	3,1,0			
occupancy	2.00	5.00			
cut-off (bohr)	1.60	1.60			
Cs (n,l,k) [Kr]	5,0,0	5,1,0	5,2,0	6,0,0	
occupancy	2.00	6.00	0.00	0.00	
cut-off (bohr)	1.85	1.78	1.83	1.81	
U (n,l,k) [Xe]	6,0,0	6,1,0	7,0,0	5,3,0	6,2,0
occupancy	2.00	5.50	0.00	0.00	0.00
cut-off (bohr)	1.75	1.75	1.75	1.75	1.75

Table 7.1: The occupancies of the pseudized wavefunctions (n,l,k) for each species to be present in the $Cs_4U_2O_4Cl_8$ simulations, and the distance cut-offs after which the pseudized wavefunctions are required to match the real wavefunctions.

For oxygen we pseudized the same electrons as in the stock-potential used in the $Mg(OH)_2$ work: the $2s^2$ and $2p^4$. Similarly for the other three species we chose to pseudize the electrons which could be considered to have any involvement in the bonding. The cut-off distances were taken from model-examples published on the opium website, and we had no need to adjust them in order to achieve the recommended acceptable convergence errors of $\leq$ 2meV, except with uranium which

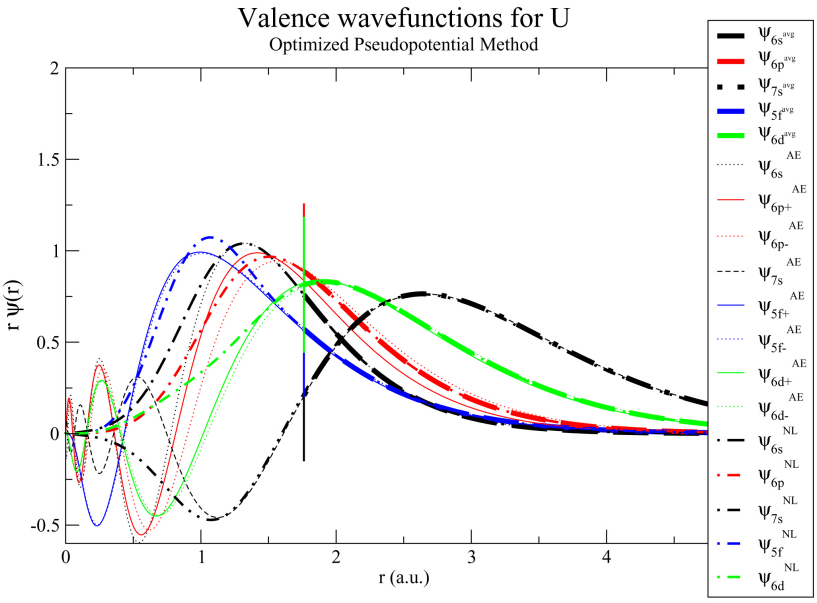

Figure 7.2: Pseudized wavefunctions of uranium, calculated using opium.

required a little work. Increasing the cut-off after which the wavefunctions must match can reduce the convergence error but it makes the resulting pseudopotentials less transferrable. We used the Cs^+ configuration rather than the neutral atom, which is a tried and tested practice for generating pseudopotentials for ionic group 1 and 2 metal-compounds. Also, we used extra test configurations for uranium and caesium in which we fractionally occupied the empty 5d, and 5f & 6d shells respectively, as it is required to at least partially occupy each type (s,p,d,f...) of each orbital to be pseudized. The resulting wavefunctions that made up the uranium pseudopotential are shown in Figure 7.2. This was the most troublesome to achieve convergence for, yet it can be seen that the wavefunctions match very well after the specified cut-off, represented by the vertical line.

Having generated our pseudopotentials, we went ahead and used them to perform CASTEP single-point and Wannier calculations on configurations generated with our empirical potential by our classical MD code. From these we could analyze the distribution of the Wannier functions around the molecular ions as we did for $Mg(OH)_2$, to gain some insight into the bonding. We plotted their distribution in histograms as a function of distance (rather than R.D.F.s) from each of the four

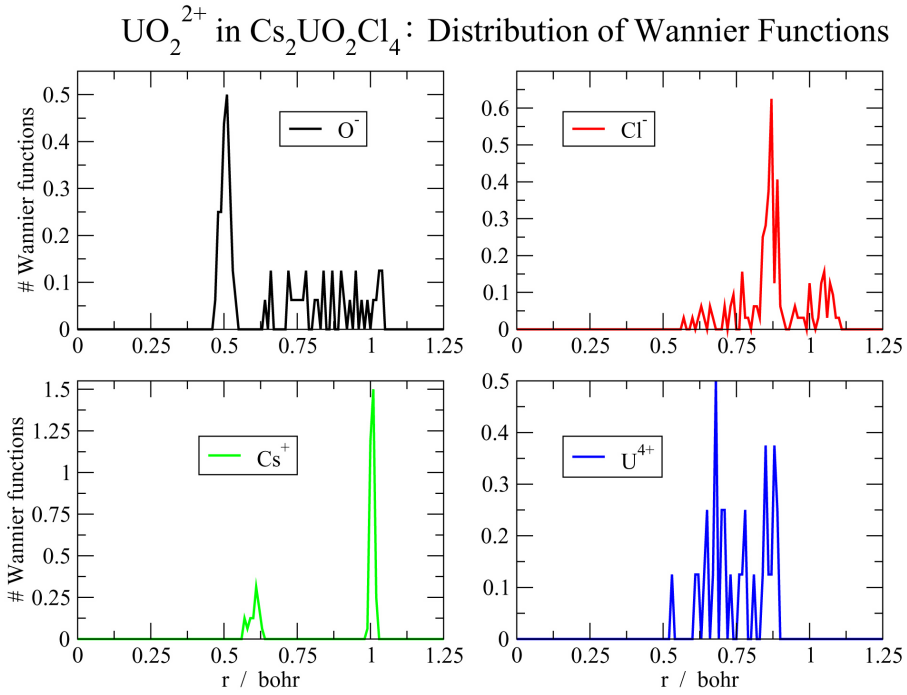

Figure 7.3: Histograms showing the distribution of Wannier functions around each of the four species in $Cs_4U_2O_4Cl_8$

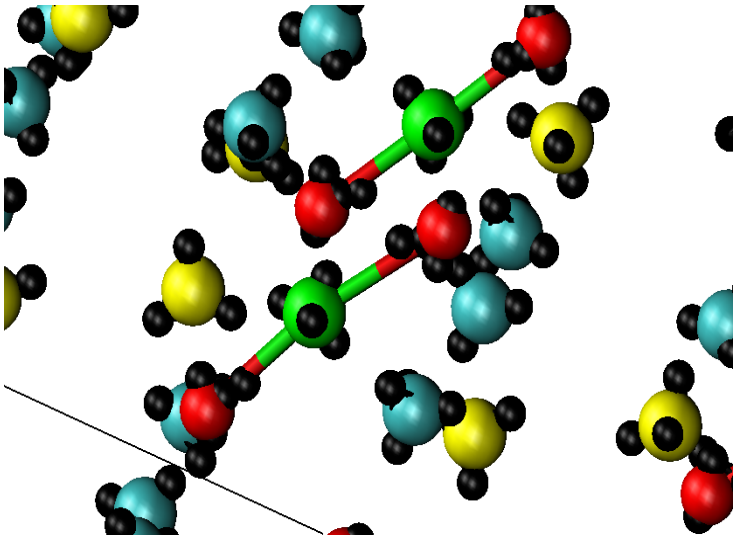

Figure 7.4: Distribution of Wannier functions around the UO_2^{2+} ions, drawn using VMD. (Green=U, Red=O, Yellow=Cs, Blue=Cl)

species of atom, giving the plots in Figure 7.3. Knowing that the U-O equilibrium bond-length was 3.36 bohr, and with the aid of the configuration plotted by VMD in Figure 7.4, where the black spheres represent the centre positions of the Wannier functions, we saw that every atom in the configuration could, to a first approximation, unequivocally be assigned four Wannier functions, surrounding each in a rough tetrahedron with none being doubly assigned. (Four is the number that would be expected given each species' formal charge and the number of pseudized electrons.) The easy assignment of each Wannier function to a particular atom differs from $Mg(OH)_2$ in that one Wannier centre was drawn along each O-H bond to the extent that it could not be assigned to just one atom, reflecting the highly covalent nature of the bonding in the OH^- molecular ions. By this measure the bonding is less covalent in UO_2^{2+}. However, looking at pictures of the configurations such as in Figure 7.4, two of the Wannier functions on each oxygen atom can be seen to lie together, drawn directly towards the central uranium atom, with the remaining two on the outer-side of the molecule at angles indicating sp^2-type hybridization. So although the degree of covalency is less, there is clear evidence of a 'double bond' between the oxygen and uranium atoms.

7.2 First Fitting Attempts, Using a RIM Potential

With the *ab initio* method now in place, and the constraints for triatomics implemented into our MD code, we generated new configurations of the same size, this time with fixed U-O bond lengths. After performing CASTEP force-calculations on them we used our adapted SHAKE algorithm to extract the none-shape-changing forces on each atom. Once again, in the triatomic constraints method we remove all short-range intramolecular interactions. Further to finding that a lower bond length convergence tolerance was required for SHAKE to reliably work for triatomics (mentioned earlier in section 5.5), we found that there was also a convergence issue in

the non-shape-changing forces with respect to the timestep we used, which was perceptibly not the case for the OH^- ion.

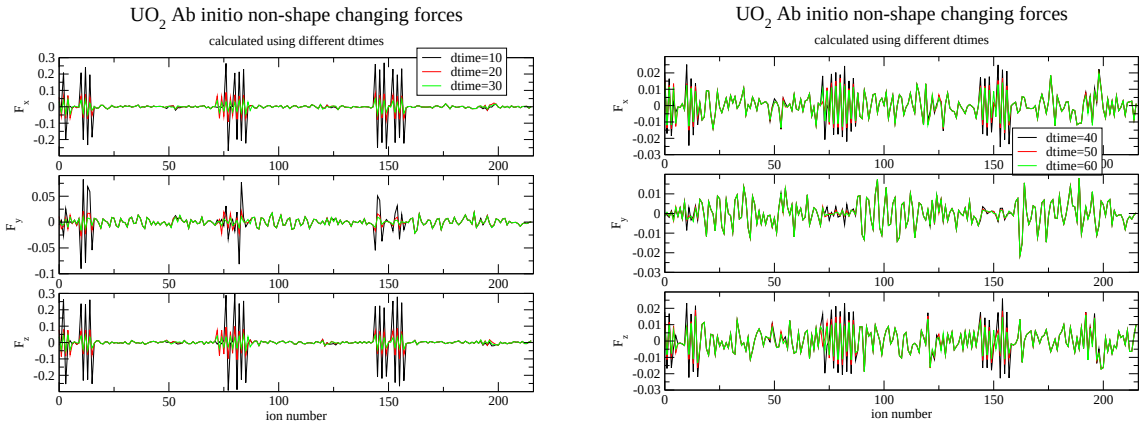

Figure 7.5: Showing how the accuracy of the non-shape changing forces depends on the timestep used in the SHAKE algorithm to extract them from the total forces. Forces given in atomic units.

Figure 7.5 shows the non-shape-changing forces calculated from the *ab initio* sets using different timesteps. It can be seen that the forces on the O and H atoms converge as the timestep is raised: the forces between timesteps of 10 and 20 a.u. are approximately a factor of four out, but by the time the timestep reaches 50 to 60 a.u. there is less than a 10% difference between the forces. This can be rationalized by the much greater molecular weight of the UO_2^{2+} molecular ion compared to the OH^-, where a longer timestep is required for enough movement to take place for SHAKE to base accurate geometry corrections on and hence for accurate non-shape-changing forces to be derived. With this in mind we would ideally use an even longer timestep than 60 a.u., but we also know that the Verlet algorithm becomes less accurate at higher timesteps, as well as there being a reduction in simulation-stability for this particular molecular shape as mentioned earlier. Therefore we chose a compromise timestep of 50 a.u.. Accordingly, we saw on fitting potentials with respective timesteps of 10 and 50 a.u. as a test that the values of χ^2 at 10 a.u. were approximately double those at 50 a.u., as the fit potential model could not replicate the inaccurate forces with the lower timestep.

With the greater number of species in $Cs_4U_2O_4Cl_8$ than $Mg(OH)_2$ there was an

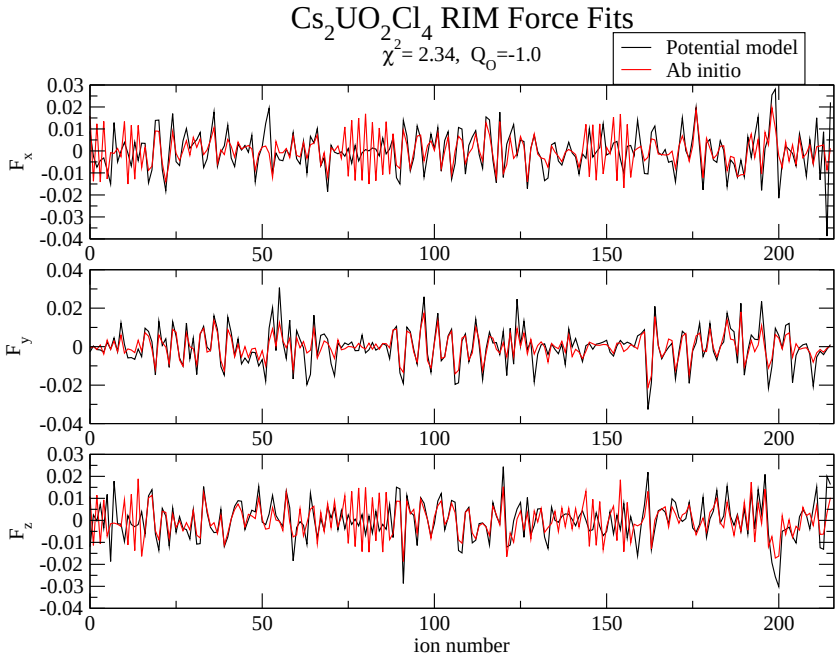

Figure 7.6: Force matching comparison from first attempts at fitting a $Cs_4U_2O_4Cl_8$ RIM potential with an MX_2 molecular geometry. Forces are in atomic units.

even more pressing need to try to cut down on the number of parameters to be fit so as not to overload the fitting program, rendering it less likely to find the global minimum on the energy surface. So once again after some preliminary fits containing all the Fumi-Tosi parameters as variables, we chose fixed values for the U-U, U-Cs and Cs-Cs parameters, thereby holding all the cation-cation interactions fixed, as it has been shown earlier in this and in the previous chapter that these provide a relatively tiny contribution to the forces on one another in the crystal state where the cations are widely spaced and shielded from one another by the anions.

Figure 7.6 shows the match of the *ab initio* to the potential model forces from a fit with a timestep of 50 a.u. (the default value hereon), and partial charges of $U^{4.0+}$ and $O^{1.0-}$. As it can be seen, a good value of χ^2 does not come easily for this molecular geometry either, although it is also clear that the three clusters of oxygen atom forces are mainly responsible, as these stand out in the diagram as not being well reproduced at all (at the beginning of each of the three configurations of 72 atoms). We saw at this stage that for some reason our potential could not

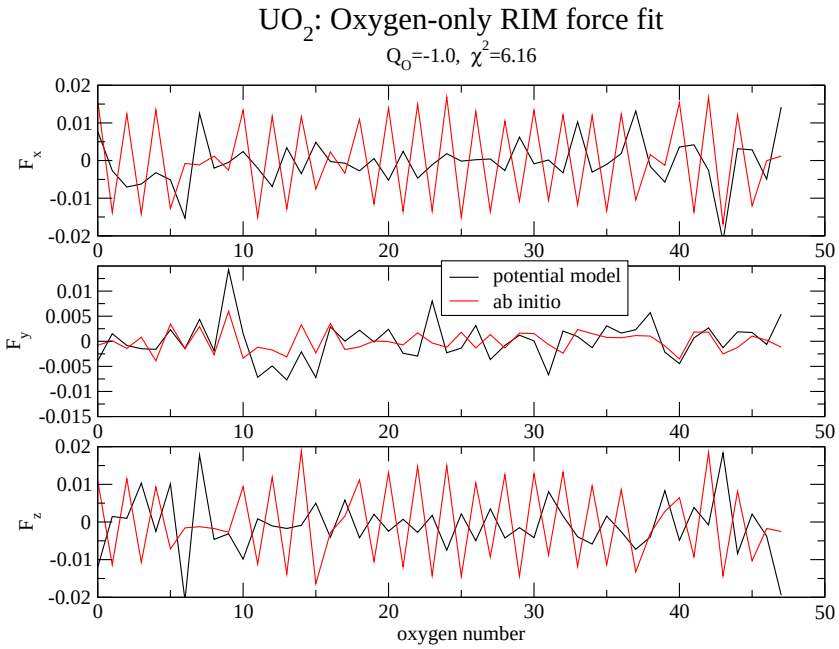

Figure 7.7: Force matching comparison from a fit to the oxygen forces alone, showing the difficulty in replicating the forces on the atoms within UO_2^{2+} molecular ions with an RIM potential. Forces are in atomic units.

match the non-shape-changing forces derived from the *ab initio* forces, within the molecules. Looking more closely at the oxygen forces alone (figure 7.7), from a fit of just the oxygen forces with the same partial charges, we see that it is predominantly the forces perpendicular to the bond axes which are not being modeled well, as the molecular axes approximately correspond with the cell b axis (component 'F_y'). Uncertain as to what was the cause of these non-fits, we went on to try fitting potentials using springs instead of constraints for the same system, and we fit the total forces on the ions. As can be seen in Figure 7.8 however, the equivalent spring fits were of even worse quality than the constraint-model fits, which indicated it was less likely an error in our implementation of the method and more likely an insufficiency in our non-polarizable potential model for describing this particular system.

Something that did not immediately occur to us was to allow the partial charge on the oxygen atoms to become positive. However it is not impossible that this could be physically realistic, despite the fact that the atomic oxygen ion is strictly

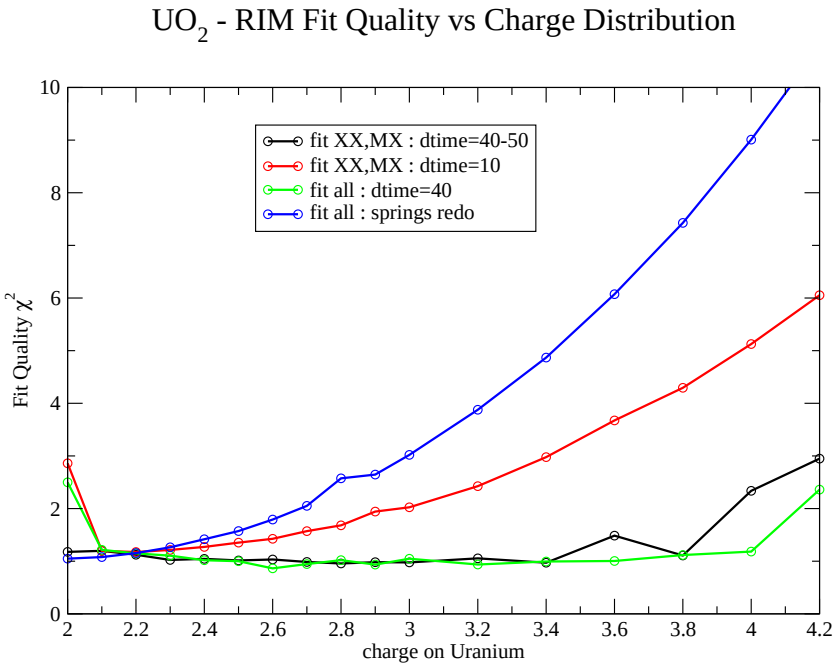

Figure 7.8: RIM fit quality versus intramolecular partial charges for the $Cs_4U_2O_4Cl_8$ system, modeled using springs to compare with fixed bond lengths, and with large and small timesteps in the SHAKE algorithm.

negative, since the total charge of the molecule is positive and the bonding covalent so much of the electron density of the oxygen atoms could be drawn towards the highly charged 'U^{6+}' atom. On fitting over a range of positive oxygen partial charges, at first to the forces on oxygen alone, we saw a great improvement in the fit quality, χ^2 dropping as low as 0.217, and it can be seen in the force comparison in Figure 7.9 how dramatically this improved the potential model's ability to reproduce the *ab initio* forces. On fitting all the species' forces together with these charges, the fit quality deteriorated somewhat giving a best value of χ^2 of approximately 1.0, but most significantly our model could now be observed to match the pattern of all the forces in the system, which meant our basic model was functioning correctly.

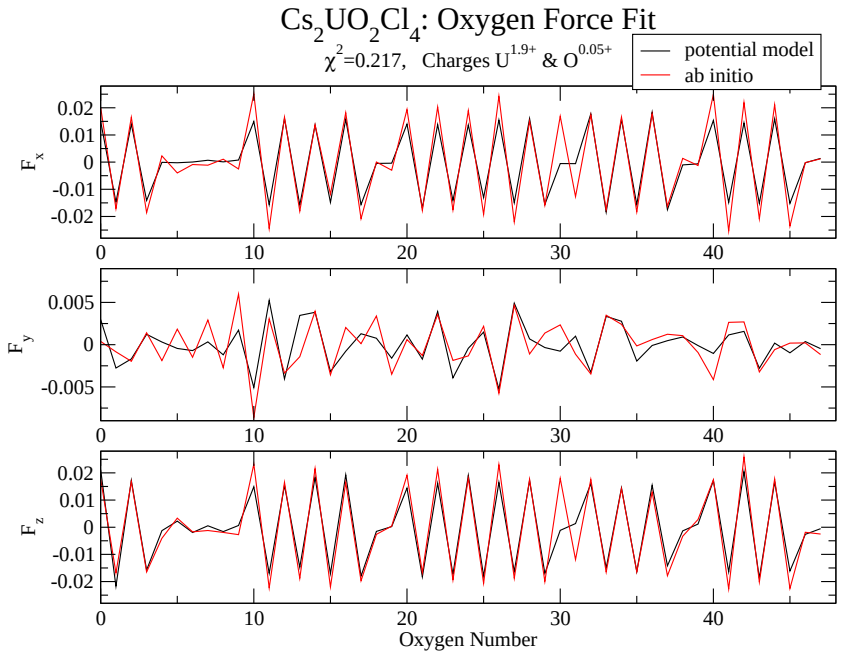

Figure 7.9: Comparison of *ab initio* and potential model forces, with a small positive partial charge on the oxygen atoms. Forces in atomic units.

7.3 Extending the Potential Model to Incorporate Polarization

The next step was to add polarization to the model, in the hope that it could improve the accuracy of our potentials as it has every time it has been introduced to the systems mentioned previously here. We saw in the case of $Mg(OH)_2$ that the molecular polarizability and the partial charges were inextricably linked: as one was altered the value of the other changed in accordance to maintain the best replication of forces and dipoles. Considering this it is possible that the apparently optimum positive oxygen charges are an artifact of a lack of polarization in the model, and that by introducing it there may be a correction to bring them back to something we would regard as more physically intuitive.

In modeling the polarization for the triatomic UO_2^{2+}, we used exactly the same principle as for the diatomic OH^-. We took the uranium atom as the origin for both the *ab initio* and MD model dipole calculations, and in the latter we allowed all of the anions to form dipoles, giving two polarizable centres on each molecule.

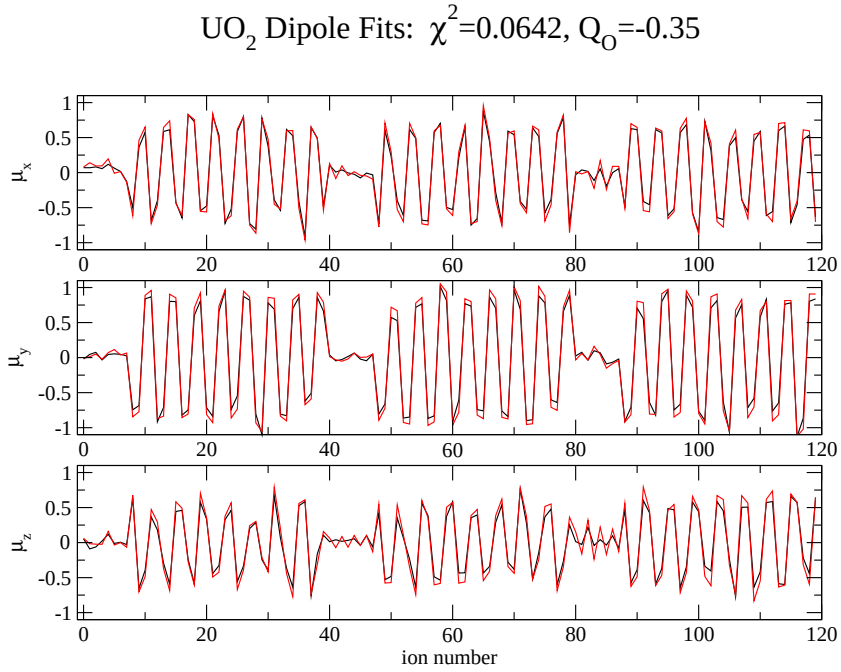

Figure 7.10: Comparison of *ab initio* and our MD model dipoles on fitting the polarization parameters for the UO_2^{2+} molecular ion, at the optimum partial charges of $O^{0.35-}$ & $U^{2.7+}$. Red = *ab initio* and black = potential model dipoles, where the values are in atomic units.

To calculate the *ab initio* molecular dipoles we summed over the charges of the oxygen nuclei and the Wannier functions distributed around the molecules. In the MD model we summed over the oxygen partial charges and added them to the conjugate-gradient-derived induced dipoles. Although we remove the intramolecular charge-dipole interactions in calculating the molecular dipoles from our MD program, it has been suggested in the past that the intramolecular dipole-induced-dipole contributions should remain intact [90] - of course they were not an issue in the OH^- ion with only one polarizable atom per molecule, but we retained them in our modeling of the molecular dipoles for UO_2^{2+}.

As in the case of $Mg(OH)_2$, we found on fitting the molecular dipoles that excellent results were achievable immediately. We fit the dipole parameters over a range of partial U/O charges corresponding to a total molecular charge of +2, and a comparison of the *ab initio*/MD model dipoles from the fit with the lowest value of χ^2 (0.0642) at charges of $O^{0.35-}$ & $U^{2.7+}$ are shown in Figure 7.10. The fit quality

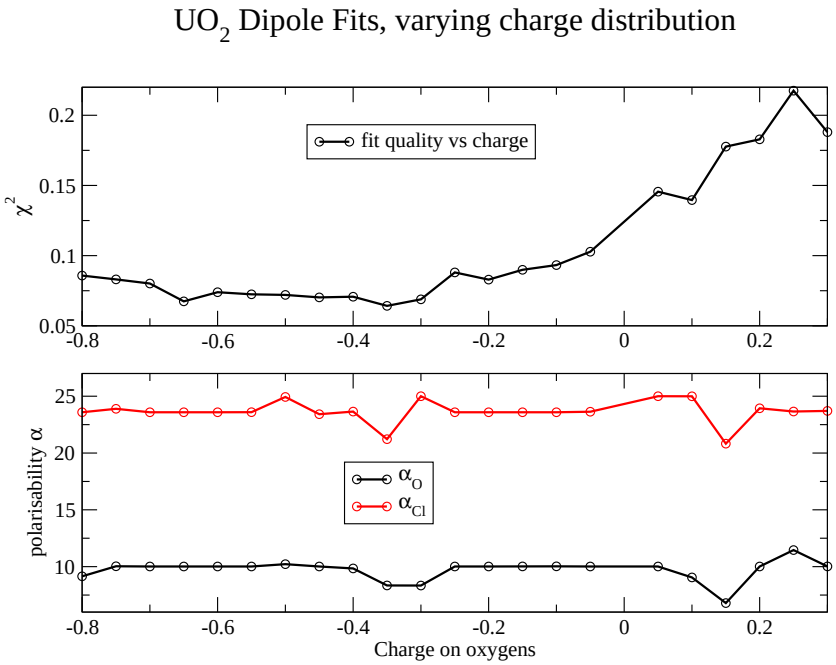

Figure 7.11: The variation in fit quality and preferred anion polarizability (in a.u.) as the partial charges are varied within the UO_2^{2+} molecular ion.

across the full range of partial charges we experimented with is shown in Figure 7.11. Unlike in the $Mg(OH)_2$ dipole fits, here we see that the optimum value of the polarizability of the oxygen atom does not seem to be dependent on the charge distribution within the molecule. However, this can be rationalized by the symmetry of the molecule: with virtually no 'permanent' contribution to the molecular dipole owing to the symmetry of linear MX_2 species, it is only the induced contribution corresponding to distortion of the valence electron distribution under the influence of the surrounding environment, into which the oxygen partial charge does not enter, which contributes. In addition to this observation we see that the trend in fit quality does not suggest that a positive charge on the oxygen atoms, however small, is ideally what we should use in the representation of the molecular charge distribution. However, as with the $Mg(OH)_2$ dipole fits we saw that there is an appreciable range of acceptable partial charge distributions we could reasonably use to model the system, which again gives us more flexibility in optimizing the force fits.

Moving on to fit the Fumi-Tosi short-range parameters to the *ab initio* forces,

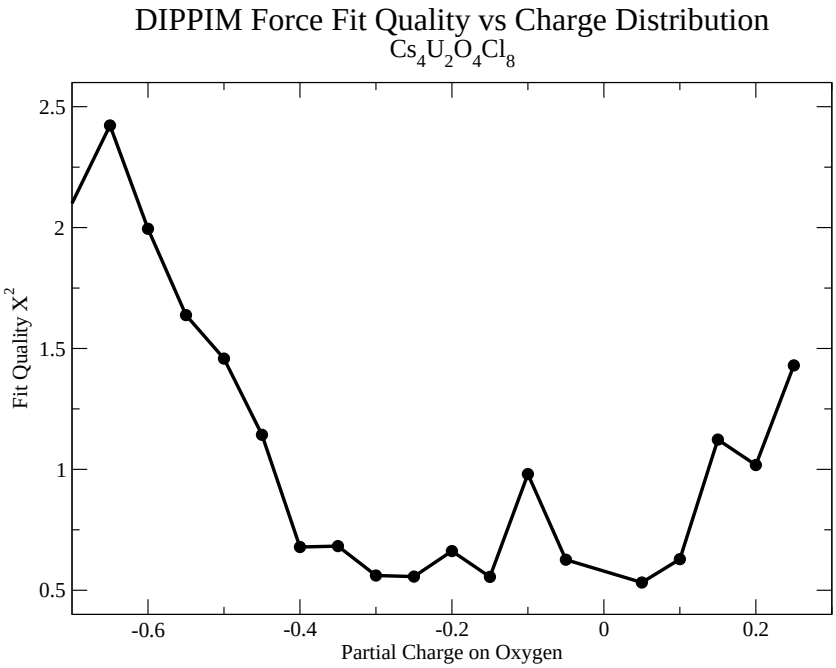

Figure 7.12: Quality of the dipolar-polarizable force fits for $Cs_4U_2O_4Cl_8$ versus partial charges within the UO_2^{2+} molecular ions.

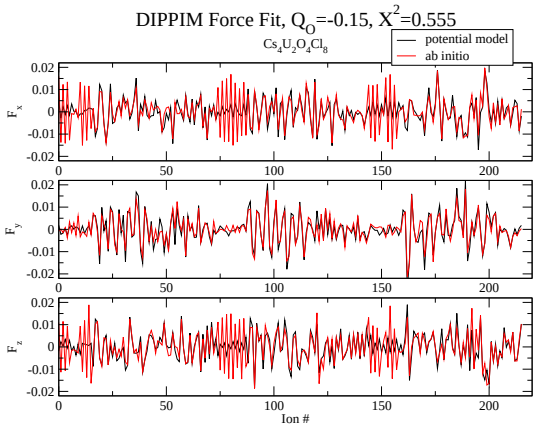

Figure 7.13: Comparison of *ab initio* and fitted forces for a dipolar polarizable potential: best result with negative partial oxygen charge. Forces are in atomic units.

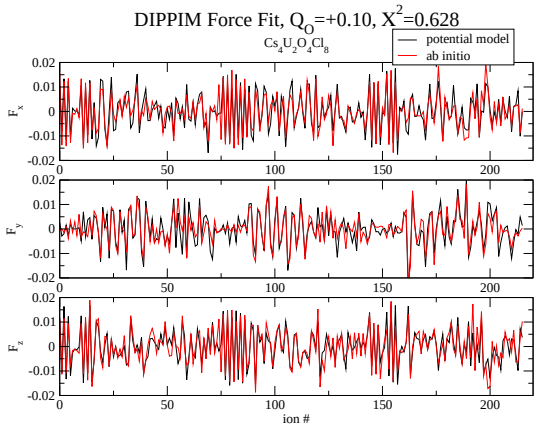

Figure 7.14: Comparison of *ab initio* and fitted forces for a dipolar polarizable potential: best result with negative partial oxygen charge. Forces are in atomic units.

we tried this over a range of partial charges, using the polarization parameters that had been fit for each respective set. What we saw, as shown in Figure 7.12, was that the best fits lay in the interval of partial charges O^n: $-0.40 \leq n \leq +0.10$, and that the two best fits had oxygen partial charges that lay either side of zero. Figures 7.13 and 7.14 compare the *ab initio* and fitted forces from two of the best fits, one with positive and one with negatively charged oxygens. Within this range of partial charges we found that while χ^2 did not vary much, the more positive the oxygen became the better the fit quality of the forces on the oxygen, but that the fit quality of the forces on the other species deteriorated. We could not determine a physical significance to this trend, but it would seem sensible to choose a potential with a more positive charge on the oxygen atoms as in these fits the quality of the forces on all species tended to be equal. At this stage however, we found we had achieved as good a fit quality for the linear triatomic as we did for the equivalent dipolar polarizable potentials for the $Mg(OH)_2$ system from the first round of fitting, the best values of χ^2 being 0.55 and 0.92 respectively. The fits from this first round for $Cs_4U_2O_4Cl_8$ were actually even more successful, though not as good as from the second round for $Mg(OH)_2$: however all of our configurations in this triatomic system lay in the thermally distorted crystal regime rather than the liquid, and the greater environmental distortion could well lead to it being more difficult to reach quite the same quality of fit using liquid configurations. Therefore the work described in this section revealed that the fitting method developed for our molecular-ion interaction model could be readily extended from diatomics to another molecular geometry, and potentially to other types of molecule as well.

7.4 Conclusions to the Molecular Ion Potential Fitting

In conclusion to the work described in this chapter, we found that through technical modifications to our MD code based upon our molecular ion potential model, and

through extension of the fitting process, we were able to create interaction potentials which reproduced the forces and dipoles on the atoms and molecules as calculated using *ab initio* methods almost or as accurately as the previous work on atomic systems. The main source of error we saw to be the layered nature of the crystals rather than the molecular nature of the ions; the dispersion, polarization and covalent effects putting more strain on our ionic-based potential model. However, through further iterations of the fitting process thereby refining the crystal structures upon which our force fits were based, we found we could greatly improve the fit quality of the potentials we produced.

We found that on extending our atomic ionic model by introducing spring interactions between atoms within a molecule, we improved the quality of our simulations containing molecular ions: even with an empirical potential we saw a massive improvement in the nature of the vibrations in the crystal, and on fitting spring-potentials we saw a significant improvement in fit quality. Even more improvement was seen on extending the model to molecules of fixed geometry. As the electron density slices and Wannier function distributions which we calculated for the $Mg(OH)_2$ and $Cs_4U_2O_4Cl_8$ systems suggested, modeling the hydroxide and uranyl ions as discrete rigid units (though still on an atomic rather than molecular level) by incorporating the SHAKE algorithm into our MD code proved a reliable method of simulation, bar some stability issues for the linear MX_2 geometry. Furthermore using SHAKE to extract the non-shape-changing forces for fitting purposes also proved a very successful method of generating potentials for these molecular systems, where we measured that success by the fit quality χ^2, comparable to atomic system potential fits, and by the ability of the fitted potentials to reproduce and maintain the experimentally reported crystal structures. A degree of the inaccuracy in the cell dimensions could be at least partially corrected by empirically fine tuning the dispersion parameters between appropriate species, where it is largely the dispersion interaction (not reproduced well in the *ab initio* DFT calculations) that is thought

to be responsible for the interlayer spacing.

As with fitting for atomic ion systems in the previous chapter (with the exception of the highly ionic NaF), we found that the rigid ion model was not sufficient to produce force fits of acceptable quality. The layered structure of the molecular ionic compounds meant this was even more the case. However we saw that by allowing the atoms to form electric dipoles the force-fit quality improved a lot, and by adjusting the polarization to a molecular-dipole based model we achieved excellent dipole fits of the polarization parameters. The introduction of dipoles also improved the quality of the force fits for the purpose of calculating the short-range parameters, and after a second round of the fitting process (carried out for $Mg(OH)_2$) where we used configurations generated by the best choice of the first fitted potential, that were more representative of the real material, we achieved good force-fits of almost the quality of the non-layered atomic systems. So, though with a little more work and a more convoluted fitting process, we found this newly developed model and method highly effective.

Chapter 8

Summary and Conclusions

The motivation for this work was to continue the development of our potential fitting technique within the regime of an extended ionic model by extending its application to the perovskite cryolite, then to assess the accuracy of the fitted potentials and use them to gain a greater understanding of the dynamical information derived from NMR spectroscopy and diffusion measurements. Secondly, was to make more substantial changes to the technique in order to model materials containing molecular ions, in which not all of the bonding can be described with an extended ionic model.

Interaction potentials for cryolite were developed via the binary compounds NaF and AlF_3, using several degrees of extension to the basic ionic model, by fitting the forces and multipoles on the ions to *ab initio* data. Adding polarization to the model at the dipolar level was the key extension that brought the greatest improvement in our description of all the systems: NaF, AlF_3 and cryolite. We demonstrated that by fitting polarization parameters in a system where polarization plays a greater role (AlF_3 >NaF), we obtained a better set of values, and for the fluoride ion which was common to both systems it was the values from the AlF_3 fits we chose to use in putting together the final potential. We also found that an improvement in the AlF_3 fits was achieved by raising the order of the multipoles to quadrupolar level, owing to greater significance of polarization in AlF_3. Adding ionic shape deformation to the model did not produce a definitive enough improvement in fit quality to justify the extra expense of using such a model in simulations of these compounds. It is

possible that some small shape deformation effects are present, but we could justify the difficulty in the fitting process picking these up using NaF and AlF_3 for structural reasons.

By fitting the potentials at differing densities, we saw that the ionic polarizability as predicted by the fitting process was dependent upon the lattice size, an observation that has been made both previously and subsequently through different methods of calculation. A corollary of this is the realization that potentials should be fit close to the density at which they intend to be used to model a system in simulation. It is also evidence that the fitting method is reproducing real physical phenomena well.

Overall, we achieved excellent force and multipole fits in this work and simulations carried out to test the best dipolar potential showed an excellent qualitative reproduction of both the low and high temperature structures, the phase transition occurring at a rather lower temperature than observed experimentally. The reproduction of the subtle tilt domain sequence in the low temperature structure, which we believe to be present owing to polarization effects, was particularly impressive and further justifies our polarization model. We went on to use the 'best' fitted potential to study the ion dynamics in cryolite, and put together a picture of the sequence of events that occurs with changing temperature. By studying the diffusion rates and calculating site-hopping activation energies, we showed that the quantitative discrepancies between the the motion in different samples could be ascribed to the intrinsically defective nature of cryolite, and that the diffusive motion of the sodium ions relies greatly upon the presence of these defects. Close study of the molecular reorientation of the AlF_6^{3-} octahedra helped demonstrate that there is no necessary qualitative inconsistency between the small thermal ellipsoids seen in diffraction data and the wide libration angles derived from NMR studies. We investigated a previously made proposition that Na^+ diffusion and AlF_6^{3-} rotation occur cooperatively via a turnstile mechanism, and found that there is some correlation

between the events, locally, at low temperatures, but that this lessens to become indistinguishable by a point high above the phase transition.

Both the empirical and fitted potentials produced the same sequence of dynamical events, suggesting this pattern is robust with respect to changes in the parameters within the dipolar potential model. When we compare the results for the dynamical behaviour on a reduced temperature scale of T/T_{trans} there is a fairly close quantitative consistency between potentials. While the first fitted potential gave a quantitative improvement on the empirical potential as measured by the point of the phase transition, by iterating the fitting procedure using actual cryolite configurations, still further improvement was made, the transition in the latter falling very close to that observed experimentally at 850 K.

Moving on to systems containing molecular ions where the intramolecular interactions are covalent in nature, we made modifications to our potential model in order to incorporate such species, and adapted the fitting process accordingly. We found that with a harmonic springs model to describe the intramolecular bonding, we could improve the description of the molecules as single entities - we saw great improvements in the vibrational spectra in comparison with the atomic ion model - however we were limited in the quality of potential we could fit using this model, and hence the accuracy we could hope to attain in describing such systems as a whole. Though even the optimized springs-model proved to be a better description of $Mg(OH)_2$ (in terms of force-fit quality) than an empirical Morse potential used in previous work, on applying a constraints-model, whereby we fixed the molecular geometries and fit to purely intermolecular forces, we achieved a significantly better series of force fits. Although it took an extra iteration of the fitting process, we found that we could achieve very good quality of force fits, almost on a par with those from atomic ionic systems. $Mg(OH)_2$ is a layered material, and by studying the atomic material $MgCl_2$ which has a similar structure, we showed that the difficulty in obtaining quite the same standard of fit as we had in the cryolite work was

due to the layered nature of the structure as opposed to the molecular nature.

Once again we found that adding polarization to the potential model improved it considerably. In order to model the polarization more rigorously we developed the fitting process to match the full-molecular rather than the induced-atomic polarizabilities from the *ab initio* and model calculations. We showed this to be necessary, given the different ways the induced polarization is modeled by either method. In addition to polarization, we found the fit quality to be highly dependent on the distribution of partial charges throughout the molecular ions, and in the case of the hydroxide ion it proved very beneficial to include short range repulsion interactions with the H atom, despite the fact that in a simple ionic system we would consider them bare nuclei - again, owing to the molecular nature of the system. Despite the greater anisotropy in $Mg(OH)_2$ than cryolite, we still found that modeling the ions as aspherical did not significantly improve the fit quality. Simulations to test the fitted $Mg(OH)_2$ potential revealed that it reproduced the crystal structure, though not the cell dimensions very accurately. By fine tuning the dispersion parameters post-fitting, using the argument that dispersion is not well reproduced in our *ab initio* DFT calculations and hence not an interaction we can usefully fit the parameters for, we found however that we could improve the potential's prediction of the cell dimensions. The development of our model and fitting process to systems containing molecular ions described here, though still in its early stages, provided a solid foundation for future work, some of which is already in progress on $Ca(OH)_2$ and carbonate-systems, and the degree of success described here is promising for other such systems.

Appendix A

Atomic Units

Due to the very small nature of the lengths, masses and timesteps involved in computer simulations, the use of SI units often leads to loss of accuracy in computer calculations. Atomic units, au, are reduced variables based upon microscopic properties, such as the distance at which the electron orbits the nucleus in the hydrogen atom, and are a set of units much more suited to the length and time-scales involved on an atomic level. The table below gives the conversion factors for the common atomic units used in the simulations.

Unit	Name	Conversion Factor
Mass	m_e	9.1095×10^{-31} kg
Time		2.4188×10^{-17} s
Charge	e	1.6022×10^{-19} C
Energy	Hartree	4.3597×10^{-18} J
Length	bohr	0.5292×10^{-10} m
Pressure		2.9420×10^{13} Pa
Electric Dipole		8.4784×10^{-30} Cm

Table A.1: Conversion factors to convert atomic units to S.I. units.

Appendix B

Abbreviations

- ***ab initio*** - Literally from first principles. A method of calculating quantities without any parameterisation of the model.
- **RIM** - Rigid Ion Model. This is the simple ionic model, in which the ions are treated as electronically rigid closed shell species with formal valence charges.
- **DIPPIM** - Dipole-Polarizable Ion Model. An extended ionic model, in which the ions are no longer treated as electronically rigid species, but have induced dipoles centred on them. **QUADPIM** raises the order of the multipole to quadrupolar level.
- **CIM** - Compressible Ion Model. The ions are allowed to 'breathe', or change their size according to their environment.
- **DAIM** - Dipolar Aspherical Ion Model. The ions are allowed to change shape according to their environment, forming distortions of dipolar symmetry. **QUAIM** raises the level of the shape distortion to quadrupolar level.
- **RDF** - Radial Distribution Function. This function is a measure of how dense the particles around a given particle are relative to an ideal gas.
- **au** - Atomic Units. A convenient set of units for measurements on the atomic scale, mostly based on the Hydrogen atom.

Appendix C

Published Paper

Ionic motion in crystalline cryolite

Authors: *Lindsay Foy and Paul A. Madden*

Publication Details: *J Phys Chem B Condens Matter Mater Surf Interfaces Biophys; Aug 2006; 110 (31); 15302-15311*

This largely covers the work described in chapter four where we study the ion dynamics in cryolite, and also makes reference to the fitting carried out in chapter three.

Appendix D

Courses, Conferences and Workshops

- Attended weekly departmental postgraduate research seminars: at Oxford this comprised one 'general physical chemistry' seminar and one 'theoretical chemistry' seminar per week, at Edinburgh this comprised one 'inorganic and structural chemistry' seminar and one CSEC seminar per week and one 'general chemistry' seminar per fortnight.

- Gave annual presentations in the departmental 'inorganic and structural' chemistry seminar series: a powerpoint talk in the second year and a whiteboard talk in the third year.

- Attended departmental 2007 Firbush meeting, gave a powerpoint presentation.

- Attended week-long CASTEP workshop at Imperial College, London, 2006.

- Undertook mathematics tutoring and marking for undergraduate chemists at Oxford, for the duration of the first year of PhD.

- Attended Brighton Careers Gradschool, October 2006.

- Attended EastChem conference and poster session at St. Andrews University.

- Attended several university computing courses relevant to field of research: MATLAB, LaTeX, FORTRAN, MPI parallel programming and OpenMP parallel programming.

- Attended several postgraduate lecture courses relevant to field of research: 'Complex Analysis and Integral Transform' (M. Child), 'Advanced Calculus' (P. Grout), 'Electronic Structure Theory' (N. Gidopoulos), 'Quantum Mechanics' (P. Atkins), and 'Statistical Mechanics' (P.A. Madden). Also a series of video-conference lectures on 'Electronic Structure Theory', speakers including C.J. Pickard and P.A. Madden.

Bibliography

[1] C. G. S. Chaudhuri, M. Wilson and P. Madden. *J. Phys. Chem. B*, **108**, 3437 (2004).

[2] M. Castiglione, M. Wilson and P. Madden. *Physical Chemistry Chemical Physics*, **1**, 165 (1999).

[3] P. Madden and M. Wilson. *Chem. Soc. Rev.*, **25**, 339 (1996).

[4] L. Foy. *A Simulation Study of Cryolite: Structure and Dynamics in the Solid Phase*. Part II thesis, Chemistry, Oxford, (2004).

[5] R. Heaton, P. Madden, R. Brookes, M. Salanne, C. Simon and P. Turq. *J. Phys. Chem. B*, **110**, 11454 (2006).

[6] Q. Williams, E. Knittle and R. Jeanloz. *Perovskite: A Structure of Great Interest to Geophysics and Materials Science*. Am. Geophys. Union, Tokyo, (1989).

[7] A. Amin. *J. Am. Ceram. Soc.*, **72**, 369 (1989).

[8] R. Newnham. *Perovskite: A Structure of Great Interest to Geophysics and Materials Science*. Am. Geophys. Union, Tokyo, (1989).

[9] J. Wiley and K. Poeppelmeier. *Perovskite: A Structure of Great Interest to Geophysics and Materials Science*. Am. Geophys. Union, Tokyo, (1989).

[10] E. Dewing. *Trans. TMS-AIME*, **245**, 1829 (1969).

[11] M. Kotecha, S. Chaudhuri, C. Grey and L. Frydman. *JACS*, **127**, 16701 (2005).

[12] D. Spearing, J. Stebbins and I. Farnan. *Phys. Chem. Minerals*, **21**, 373 (1994).

[13] K. Grjotheim, C. Krohn, M. Malinovsky, K. Matiasovsky and J. Thonstad. *Aluminium Electrolysis: Fundamentals of the Hall-Heroult Process*. Aluminium-Verlag, Dusseldorf, (1982).

[14] A. Aguado, L. Bernasconi, S. Jahn and P. Madden. *Faraday Discussions*, **124**, 171 (2003).

[15] U. Müller. *Inorganic Structural Chemistry*. Wiley, Chichester, (1992).

[16] D. Evans and R. Slade. *Struct. Bond.*, **119**, 1 (2006).

[17] S. Newman and W. Jones. *New J. Chem.*, **22**, 105 (1998).

[18] F. Cavani. *Catal. Today*, **11**, 173 (1991).

[19] M. Hermosin. *Fres. Environ. Bull.*, **4**, 41 (1995).

[20] F. Figueras. *Top. Catal.*, **29**, 189 (2004).

[21] S. Rhee. *Environ. Technol.*, **18**, 231 (1997).

[22] G. Onkal-Engin. *Environ. Technol.*, **21**, 167 (2000).

[23] S. Cotton. *Lanthanide and Actinide Chemistry*. WileyBlackwell, (2006).

[24] M. Allen and D. Tildesley. *Computer Simulation of Liquids*. Clarendon, (1987).

[25] N. Metropolis, A. Rosenbluth, M. Rosenbluth, A. Teller and E. Teller. *J. Chem. Phys.*, **21**, 1087 (1953).

[26] M. Born and J. Mayer. *Zeits. f. Physsik*, **75**, 1 (1932).

[27] F. Fumi and M. Tosi. *J. Phys. Chem. Solids*, **25**, 31 (1964).

[28] F. Fumi and M. Tosi. *J. Phys. Chem. Solids*, **25**, 45 (1964).

[29] K. Tang and J. Toennies. *J. Chem. Phys.*, **80**, 3726 (1984).

[30] F. Hutchinson, M. Wilson and P. Madden. *Molec. Phys.*, **99**, 811 (2001).

[31] R. Heaton, P. Madden, A. Aguado and S. Jahn. *J. Mol. Struct. Theochem.*, **771**, 9–18 (2006).

[32] M. Segall, P. Lindan, M. Probert, C. Pickard, P. Hasnip, S. Clark and M. Payne. *J. Phys.: Cond. Matt.*, **14 (11)**, 567 (2002).

[33] D. Vanderbilt. *Phys. Rev. B*, **41 (11)**, 7892 (1990).

[34] L. Bernasconi, P. Madden and M. Wilson. *PhysChemComm*, **5**, 1–11 (2002).

[35] L. Bernasconi, P. Madden and M. Wilson. *Computational Materials Science*, **22 (1-2)**, 94–98 (2001).

[36] R. Heaton. *From First Principles to Material Properties.* DPhil thesis, Chemistry, Oxford, (2007).

[37] J. Perdew, K. Burke and M. Ernzerhof. *Phys. Rev. Lett*, **77**, 3865 (1996).

[38] A. Aguado, L. Bernasconi and P. Madden. *Chem. Phys. Lett.*, **356**, 437 (2002).

[39] F. James. CERN Program Library Long Writeup D506.

[40] A. Wells. *Structural Inorganic Chemistry.* Oxford University Press, (1950).

[41] M. Segall, P. Lindan, M. Probert, C. Pickard, P. Hasnip, S. Clark and M. Payne. *J. Phys. Condens. Matt.*, **14**, 2717 (2002).

[42] D. Vanderbilt. *Phys. Rev. B*, **41**, 7892 (1990).

[43] G. Janz. *Thermodynamic and Transport Properties of Molten Salts: Correlation Equations for Critically Evaluated Density, Surface Tension, Electrical Conductance, and Viscosity Data.* J. Phys. Chem. Ref. Data, 17, Suppl. 2, (1988).

[44] P. Fowler and P. Madden. *J. Phys. Chem*, **89**, 2581 (1985).

[45] P. Daniel, A. Bulou, M. Rousseau, J. Nouet, J. Fourquet, M. Leblanc and R. Burriel. *J. Phys. Condens. Matt.*, **2**, 5663 (1990).

[46] http://www.cerac.com/pubs/proddata/alf3.htm.

[47] S. Chaudhuri, P. Chupas, M. Wilson, P. Madden and C. Grey. *J. Phys. Chem. B*, **108 (11)**, 3439 (2004).

[48] H. Yang, S. Ghose and D. Hatch. *Phys. Chem. Minerals*, **19**, 528 (1993).

[49] A. Glazer. *Acta Crystallogr.*, **B28**, 3384 (1972).

[50] A. Glazer. *Acta Crystallogr.*, **A31**, 756 (1975).

[51] K. Suzuki. *J. Phys. Soc. Japan*, **64**, 674 (1995).

[52] Q. Zhou and B. Kennedy. *J. Solid State Chemistry*, **177**, 654 (2004).

[53] R. Nacken. *Centre. Min.*, **38**, 38 (1908).

[54] W. Roth and W. Bertram. *Z. Elektrochem*, **35**, 297 (1929).

[55] G. Menzer. *Naturwissenschaften*, **26**, 236 (1938).

[56] S. V. Naray-Szabo and K. Sasvari. *Z. Kristallogr.*, **9**, 27 (1939).

[57] V. Lacassagne, C. Bessada, D. Massiot, P. Florian and J. Coutures. *J.Chimie Physique*, **95**, 322 (1998).

[58] G. Landon and A. Ubbelohde. *Proceedings of the Royal Society of London. Series A, Mathematical and Physical Sciences*, **240**, 160 (1957).

[59] S. Hull. *Reports on Progress in Physics*, **67 (7)**, 1233 (2004).

[60] S. Falak, A. Venimadhav, M. Blamire, B. Dabrowski, S. Kolesnik and J. Attfield. *Solid State Sciences*, **7 (8)**, 912 (2005).

[61] J. Donnay. *Amer. Min.*, **37**, 230 (1952).

[62] D. Wrinch. *Amer. Min.*, **37**, 234 (1952).

[63] S. Jahn, J. Ollivier and F. Demmel. *Solid State Ionics*, **179**, 1957–1961 (2008).

[64] G. Martyna, D. Tobias and M. Klein. *J. Chem. Phys.*, **101 (5)**, 4177 (1994).

[65] S. Cikit, S. Ukar, Z. Akadeniz and P. Madden. *awaiting publication*, (2009).

[66] M. Castiglione, M. Wilson, P. Madden and C. Grey. *J. Phys. Condens. Matter*, **13 (1)**, 51 (2001).

[67] M. Castiglione and P. Madden. *J. Phys. Condens. Matter*, **13 (44)**, 9963 (2001).

[68] A. Solheim and A. Sterten. *Proceedings of the Ninth International Symposium on Light Metals Production*. pages 225–234 (1997).

[69] E. Dewing. *Metallurgical and Materials Transactions B*, **28B**, 1095 (1997).

[70] E. Stewart and H. Rooksby. *Acta Cryst.*, **6**, 49 (1953).

[71] Y. Gebremichael, M. Vogel and S. Glotzer. *J. Chem. Phys.*, **120 (9)**, 4415 (2004).

[72] J. Ryckaert, G. Ciccotti and H. Berendsen. *J. Comput. Phys.*, **23**, 327 (1977).

[73] D. Parfitt, D. Keen, S. Hull, W. Crichton, M. Mezouar, M. Wilson and P. Madden. *Phys. Rev. B*, **72**, 054121 (2005).

[74] W. Glover. *Part II Thesis*. Part II thesis, Chemistry, Oxford, (2003).

[75] D. Watkin, R. Denning and K. Prout. *Acta Crystollagraphica C: Crystal Struct. Comm.*, **47**, 2517 (1991).

[76] T. Kundu, K. H. Rao and S. Parker. *J. Colloid and Interface Science*, **295**, 364 (2006).

[77] G. Conn and C. Wu. *Trans. Faraday. Soc.*, **34**, 1483 (1938).

[78] M. Catti, G. Ferraris, S. Hull and A. Pavese. *Phys Chem Minerals*, **22**, 200 (1995).

[79] R. Heaton. Unpublished.

[80] A. Aguado and P. Madden. *J. Chem. Phys.*, **119(14)**, 7471 (2003).

[81] G. Ciccotti, M. Ferrario and J. Ryckaert. *Molec. Phys.*, **47**, 1253 (1982).

[82] G. Ciccotti and J. Ryckaert. *Comp. Physics Reports*, **4 (6)**, 345 (1986).

[83] J. Tissen and G. Janssen. *Molec. Phys.*, **71 (2)**, 413 (1990).

[84] http://chemicalland21.com/.

[85] N. Harrison and V. Saunders. *J. Phys Cond. Matter*, **4**, 3873 (1992).

[86] G. Tribello. *Superionic Heterostructured Materials*. Part II thesis, Chemistry, Oxford, (2004).

[87] P. Arnold, D. Patel, C. Wilson and J. Lowe. *Nature*, **451**, 315 (2008).

[88] J. Boncella. *Nature*, **451 (17)**, 250 (2008).

[89] opium.sourceforge.net.

[90] J. Applequist. *JACS*, **94**, 2952 (1972).